NAVAL POSTGRADUATE SCHOOL
MONTEREY, CALIFORNIA

DTIC
S ELECTE D
JUL 2 0 1995
G

THESIS

NON-DESTRUCTIVE INSPECTION OF COMPOSITE STRUCTURES USING MODAL ANALYSIS

by

Timothy Stirling Matthews

March, 1995

Thesis Advisor: Edward M.Wu

Approved for public release; distribution is unlimited.

19950719 028

REPORT DOCUMENTATION PAGE		Form Approved OMB No. 0704-0188

Public reporting burden for this collection of information is estimated to average 1 hour per response, including the time for reviewing instruction, searching existing data sources, gathering and maintaining the data needed, and completing and reviewing the collection of information. Send comments regarding this burden estimate or any other aspect of this collection of information, including suggestions for reducing this burden, to Washington Headquarters Services, Directorate for Information Operations and Reports, 1215 Jefferson Davis Highway, Suite 1204, Arlington, VA 22202-4302, and to the Office of Management and Budget, Paperwork Reduction Project (0704-0188) Washington DC 20503.

1. AGENCY USE ONLY *(Leave blank)*	2. REPORT DATE March 1995	3. REPORT TYPE AND DATES COVERED Master's Thesis

4. TITLE AND SUBTITLE NON-DESTRUCTIVE INSPECTION OF COMPOSITE STRUCTURES USING MODAL ANALYSIS	5. FUNDING NUMBERS
6. AUTHOR(S) Matthews, Timothy S.	

7. PERFORMING ORGANIZATION NAME(S) AND ADDRESS(ES) Naval Postgraduate School Monterey CA 93943-5000	8. PERFORMING ORGANIZATION REPORT NUMBER

9. SPONSORING/MONITORING AGENCY NAME(S) AND ADDRESS(ES)	10. SPONSORING/MONITORING AGENCY REPORT NUMBER

11. SUPPLEMENTARY NOTES The views expressed in this thesis are those of the author and do not reflect the official policy or position of the Department of Defense or the U.S. Government.

12a. DISTRIBUTION/AVAILABILITY STATEMENT Approved for public release; distribution is unlimited.	12b. DISTRIBUTION CODE

13. ABSTRACT *(maximum 200 words)*
Anomalies from manufacturing variability or in-service damage are manifested as subtle differences in the inertial and stiffness matrices of otherwise identical components. Modal analysis seeks to model these constitutive relations by examining a structure's dynamic response to applied vibrations. In this investigation, characterization of anomalies in composite structures is attempted through multi-input, multi-output modal analysis. Two graphite-epoxy specimens manufactured by different processes are subjected to random excitation and frequency response functions are obtained. The dynamic behavior of the structures is compared through modal parameter extraction techniques. Dynamic solutions from a finite element model are used to validate the results. Finally, observations are made concerning the feasibility of extending the procedure to quality assurance and damage detection applications.

14. SUBJECT TERMS Modal Analysis, Composite Structures, Non-Destructive Inspection			15. NUMBER OF PAGES 118
			16. PRICE CODE

17. SECURITY CLASSIFI- CATION OF REPORT Unclassified	18. SECURITY CLASSIFI- CATION OF THIS PAGE Unclassified	19. SECURITY CLASSIFI- CATION OF ABSTRACT Unclassified	20. LIMITATION OF ABSTRACT UL

NSN 7540-01-280-5500

Standard Form 298 (Rev. 2-89)
Prescribed by ANSI Std. 239-18 298-102

NON-DESTRUCTIVE INSPECTION OF COMPOSITE STRUCTURES USING MODAL ANALYSIS

Timothy S. Matthews
Lieutenant Commander, United States Navy
B.S., University of Colorado, 1980

Submitted in partial fulfillment
of the requirements for the degree of
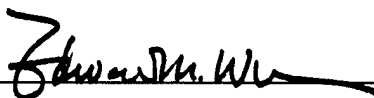
MASTER OF SCIENCE IN AERONAUTICAL ENGINEERING

from the

NAVAL POSTGRADUATE SCHOOL
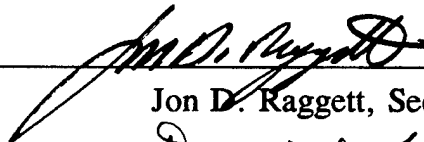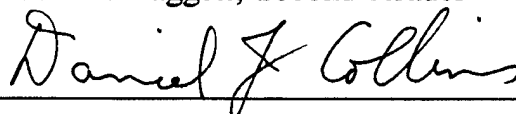**March 1995**

Author: _____

Timothy S. Matthews

Approved by: _____

Edward M. Wu, Thesis Advisor

_____

Jon D. Raggett, Second Reader

_____

Daniel J. Collins, Chairman,
Department of Aeronautical Engineering

iii

ABSTRACT

Anomalies from manufacturing variability or in-service damage are manifested as subtle differences in the inertial and stiffness matrices of otherwise identical components. Modal analysis seeks to model these constitutive relations by examining a structure's dynamic response to applied vibrations. In this investigation, characterization of anomalies in composite structures is attempted through multi-input, multi-output modal analysis. Two graphite-epoxy specimens manufactured by different processes are subjected to random excitation and frequency response functions are obtained. The dynamic behavior of the structures is compared through modal parameter extraction techniques. Dynamic solutions from a finite element model are used to validate the results. Finally, observations are made concerning the feasibility of extending the procedure to quality assurance and damage detection applications.

Accesion For		
NTIS CRA&I	☒	
DTIC TAB	☐	
Unannounced	☐	
Justification		
By		
Distribution /		
Availability Codes		
Dist	Avail and / or Special	
A-1		

TABLE OF CONTENTS

ACKNOWLEDGEMENT

I. INTRODUCTION

Traditional methods of Non-Destructive Inspection (NDI) for Naval Aviation applications are inadequate for identifying damage/defects in composite materials for several reasons [Refs. 1, 2]. The widely used techniques of eddy current, dye penetrant, and magnetic particle inspection are applicable only to metallic structures and will only show structural damage close to the surface of the component. Ultrasonic testing (UT) results are often ambiguous or difficult to interpret and quantify and require a reference standard for calibration. Standard radiographic testing is difficult to perform in the field, presents a significant safety hazard, is insensitive to defects and delaminations, and the results (in the form of film images) are often highly subjective [Ref. 3]. A technique currently under development, acoustic emissions (AE) testing, shows promise but suffers from sensitivity to background noise. Clearly, as the use of composite materials expands in programs such as the F-18E/F and V-22, a new approach to NDI is needed.

The characterization of a structure's dynamic behavior may be achieved through an examination of its response to an induced vibration, a process generally known as "modal analysis". Modal analysis using multiple input, multiple output (MIMO) excitation in the lower frequency range (below 1000 Hz) is relatively straightforward to perform with the signal processing tools now available, and, given sufficient resolution, can be used to detect differences in the dynamic response characteristics of two seemingly identical structures. The premise of this investigation is that these differences in resonant frequencies, damping ratios, and deformation amplitudes can then be linked to manufacturing anomalies, internal damage, or other structural deficiencies in components. If the procedure proves viable, the long term goal is to adapt this technique for use at depot and intermediate level maintenance activities for both quality assurance acceptance testing and damage detection.

The application presented here sought to utilize MIMO modal analysis to detect differences in the structural composition of composite components by a comparison of

1

modal parameters obtained through vibration tests. Test results from two 1 foot square composite plates which were manufactured by different processes were compared to each other through the extraction of modal parameters. The results were validated against a finite element model which can be updated with the test results for use as a baseline in future measurements. The results suggest that, though further refinement is required, the procedure is a viable method of detecting manufacturing anomalies and internal damage in composite materials. Localization of such deficiencies was not attempted and is the next logical extension of the technique.

The damage localization problem was recently investigated by Campbell [Ref. 4], where frequency domain localization using the Error Matrix Method was applied to a composite beam with purposely fabricated damage located along the neutral axis. A single reference and response data acquisition system was used to collect the frequency domain data. In his investigation, the damage was consistently identified but the localization results were inconclusive. Among his recommendations for future work were the utilization of multiple channel data acquisition systems and frequency response function curve fitting techniques.

II. BACKGROUND

A. MODAL ANALYSIS OVERVIEW

Modal analysis refers to the identification of the modal parameters of a structure in order to characterize its dynamic behavior. These modal parameters are the resonant frequencies, damping ratios and mode shapes. The mode shapes represent the physical displacement of the structure at a particular resonant frequency (mode). Together, these quantities make up a unique "modal model" of the structure which describes its dynamic behavior and as such represent the inertial and stiffness properties of the structure. The modal parameters can be obtained through dynamic analysis of a theoretical (finite element) model or through vibration testing of the physical structure. Traditional applications of the modal analysis approach have been to [Ref. 5]:

1. Use the results of a modal test to verify and adjust a finite element model.
2. Produce a mathematical model of the structure to predict the effects of structural modifications.
3. Estimate the forces a structure experiences in operation through measurement of the response to the unknown forces and a mathematical description of the transfer function.

The procedure by which the modal parameters are obtained depends upon whether a theoretical model or a vibration test is used to derive them. The theoretical and experimental approaches to modal analysis start from opposite directions to arrive at the same point: identification of the modal parameters.

B. THEORETICAL MODEL APPROACH

Modal properties can be obtained for a N Degree of Freedom (DOF) viscously damped system by solving the N equations of motion, as follows:

$$[m] \{q''(t)\} + [c] \{q'(t)\} + [k] \{q(t)\} = \{F(t)\} \qquad 1$$

3

where

[m] = mass matrix

[c] = damping matrix

[k] = stiffness matrix

{q(t)} = displacement in generalized coordinates

{F(t)} = generalized applied forces

The system of equations is reduced to a straightforward N by N eigenvalue problem when the excitation and damping are zero (free vibration). The result yields the system's undamped natural frequencies (the eigenvalues) and mode shapes (eigenvectors) for free vibration. If proportional damping is assumed, where

$$[c] = \beta[k] + \gamma[m], \qquad\qquad 2$$

then the mode shapes are identical to those derived from the undamped case [Ref. 5], and the damped natural frequencies are given by

$$\omega_{dr}^2 = \omega_r^2 (1 - \zeta_r^2), \quad \text{where } \zeta_r = \beta \omega_r / 2 + \gamma / 2 \omega_r . \qquad 3$$

Even in the general damped case, with small damping ratios the mode shapes and frequencies are very close to those in the undamped case.

In a finite element model the total number of DOF's corresponds to the summation of the DOF's at each node. The system of N equations can then be solved for the mode shapes and frequencies using a number of algorithms suited for this purpose [Ref. 5, 6].

The response of the structure to an applied excitation is usually characterized in the frequency domain by the transfer function, known as the frequency response function (FRF), from the applied excitation to the displacement, velocity, or acceleration response. The complete "response model" of a structure would consist of many different FRF's, one for each excitation and response pair. For a proportionally damped multiple DOF system, the FRF can be written as [Ref. 5]:

$$H_{ij}(\omega) = \sum_{r=1}^{N} \frac{A^r_{ij}}{\omega_r^2 - \omega^2 + i2\zeta_r\omega_r\omega} \qquad 4$$

where

A^r_{ij} = modal constant or residue

ω_r = natural frequency

ζ_r = damping ratio of rth mode

N = total number of modes of interest

j = reference (excitation) coordinate

i = response coordinate

The coefficients or "residues" are complex in general and are usually expressed in terms of amplitude and phase. These residues represent the spacial orientation of the structure in a particular mode and can be used to derive the mode shapes. The FRF contains information on all of the modal parameters, since the resonant frequencies occur at the peaks in the FRF (w = w$_r$), and the relative amplitudes of the peaks provide the mode shapes and damping ratios. Appendix A provides additional background on theoretical vibrational analysis.

C. MODAL TESTING

In the modal testing approach, modal parameters are derived from examining the response of the system to a known excitation. The responses are typically in the form of accelerations, obtained through accelerometers placed on the structure at various locations. The reference force measurement is provided by a force transducer connected to the source of excitations (shakers). The time history of these signals is converted into the frequency domain by the use of Fast Fourier Transform (FFT) techniques and the result is a frequency domain transfer function, the FRF, as H=a/f. As noted above, the FRF contains all of the desired modal parameters; the challenge is in extracting a consistent set of parameters from the test data which normally consists

5

of many FRF's (for each force input there will be a set of FRF's, one for each accelerometer). In practice, extraction of the modal parameters from the set of FRF's consists of the following basic steps:

1. Obtain FRF's from FFT analyzer.

2. Assemble the set of FRF's into a matrix where each entry in the matrix represents the response at point i to an excitation at point j.

3. Use a curve-fitting algorithm to obtain the natural frequencies, damping ratios and mode shapes for the functions contained within the FRF

matrix. An analytic expression is generated for the FRF's and can be checked against the test FRF to assess the accuracy of the fit. A number of routines are currently available for this purpose, such as the complex exponential, direct parameter, and polyreference techniques [Ref. 7, 8].

4. Compare the derived mode shapes through a correlation method such as Modal Assurance Criteria (MAC) (Appendix C) to determine accuracy of mode shapes and curve fit.

Until the mid-1970's, modal testing was conducted almost exclusively using a single input force and often with only one response measurement taken at a time [Ref. 8]. MIMO testing became possible with the advent of modern digital signal analyzers but the hardware was relatively expensive and the parameter estimation algorithms were not yet developed.

MIMO modal testing has recently become more feasible and inexpensive due to advances in piezoelectric transducers, digital signal analyzers and associated software. MIMO offers several advantages over single input excitation methods, including:

1. Better distribution of excitation energy, especially in large structures.

2. Consistent, more complete FRF database. Measurements are taken simultaneously vice during multiple passes for each spacial location.

3. Ensures all vibrational modes are adequately excited in a given frequency range.

4. Reduced probability of introducing systematic errors to FRF's.

These advantages have made MIMO modal testing a useful tool in the aerospace industry, where large structures such as the Space Shuttle Solid Rocket Motors must be analyzed [Ref. 9].

D. TEST ARTICLE DESCRIPTIONS

The test articles were two 13.750 x 14.125 x .088 inch plates made by Hercules Corp of Magna, Utah, from IM-7 graphite epoxy material. Detailed material property specifications and photographs of these plates are provided in Appendix D. The ply stacking sequence and orientation angles are shown in Figure 1 and were identical for each plate; however, one was constructed using a fiber placement machine (hereafter referred to as the MLU plate), while the other was made using the standard hand lay-up technique (hereafter referred to as the HLU plate). The fiber placement process is a relatively new procedure whereby fiber tows are positioned for layup by a special fiber placement machine. Hand lay up is the more conventional procedure performed by manually cutting each ply from B-staged (partially cured) prepreg fabric and building up the laminate one ply at a time. Like components made from the two processes are known to have different acoustical properties. The HLU plate weighed 0.9520 lbf. and the MLU plate weighed 0.9513 lbf.

The plates are classified as symmetric angle-ply laminates with generally orthotropic layers [Ref. 10, p. 165]. The symmetric layup means that the coupling stiffness matrices will be zero and there will not be any coupling between bending and extension in the laminates (see Appendix E). The extensional and bending stiffness matrices, however, will be fully populated and some twist coupling stiffness can be anticipated. This means that any curvature from bending will also result in an out of plane twist. The effect of this twist-curvature coupling is generally to increase the strain energy density and reduce the vibration frequencies. The effect of twist coupling is proportional to 1/N, where N is the number of laminate layers [Ref. 10].

7

CURRENT LAMINATE

HERCULES IM-7/8552

PLY PROPERTIES

PLY THICKNESS = .0055 INCHES

TENSILE STRENGTH = 400 KSI

SHEAR STRENGTH = 14.5 KSI

TENSILE MODULUS = 25 MSI

SHEAR MODULUS = 0.71 MSI

FIBER VOLUME = 62 %

45
0
-45
90
90
-45
0
45
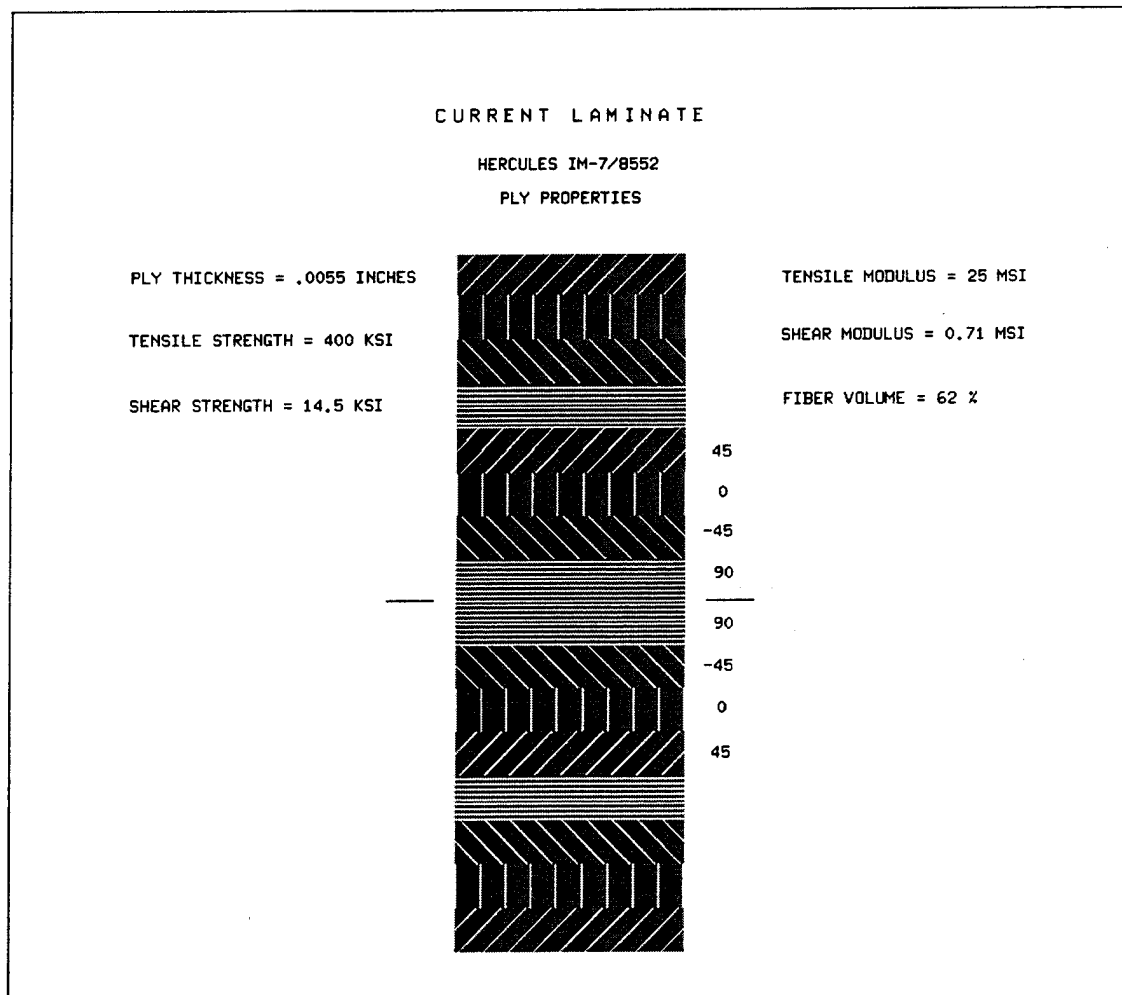
Figure 1. Test Specimen Ply Layup Sequence

III. THEORETICAL ANALYSIS

A. FINITE ELEMENT MODELING

Finite element models were constructed and analyzed using Structural Dynamics Research Corporation (SDRC) IDEAS software. IDEAS is a multipurpose structural analysis software package for workstations incorporating design, modeling, simulation, analysis and testing features. To verify the analysis method, finite element models were developed for isotropic aluminum and steel plates for which known natural frequency data was available. This enabled the selection of the element types that would best predict the dynamic behavior of the test specimens.

The model was built by first specifying the geometry and then using a automeshing feature to create the nodes and elements at specified intervals. The quadrilateral parabolic thin shell elements were selected as those providing the most reasonable results while being compatible with the laminate material feature of the software. This element's bending stiffness is based on the Mindlin shell equations where the transverse shear strain displacements are included [Ref. 11]. Specific properties of the parabolic thin shell elements are available in Reference 11. The model was meshed with elements measuring two inches per side with 49 total elements and 176 total nodes. Lumped mass elements were later added to simulate the transducers after their location was determined. Figure 2 shows the overall configuration.

The material for the model was generated using the IDEAS Laminate feature, which allows each individual ply's material, orientation and thickness to be specified. The plies are then built up into a complete laminate which was applied to the finite element model. The material for our laminate was the same for each ply but the ply orientation varied as noted in Chapter II above. The laminate applied to the finite element model was the same as that depicted previously in Figure 1.
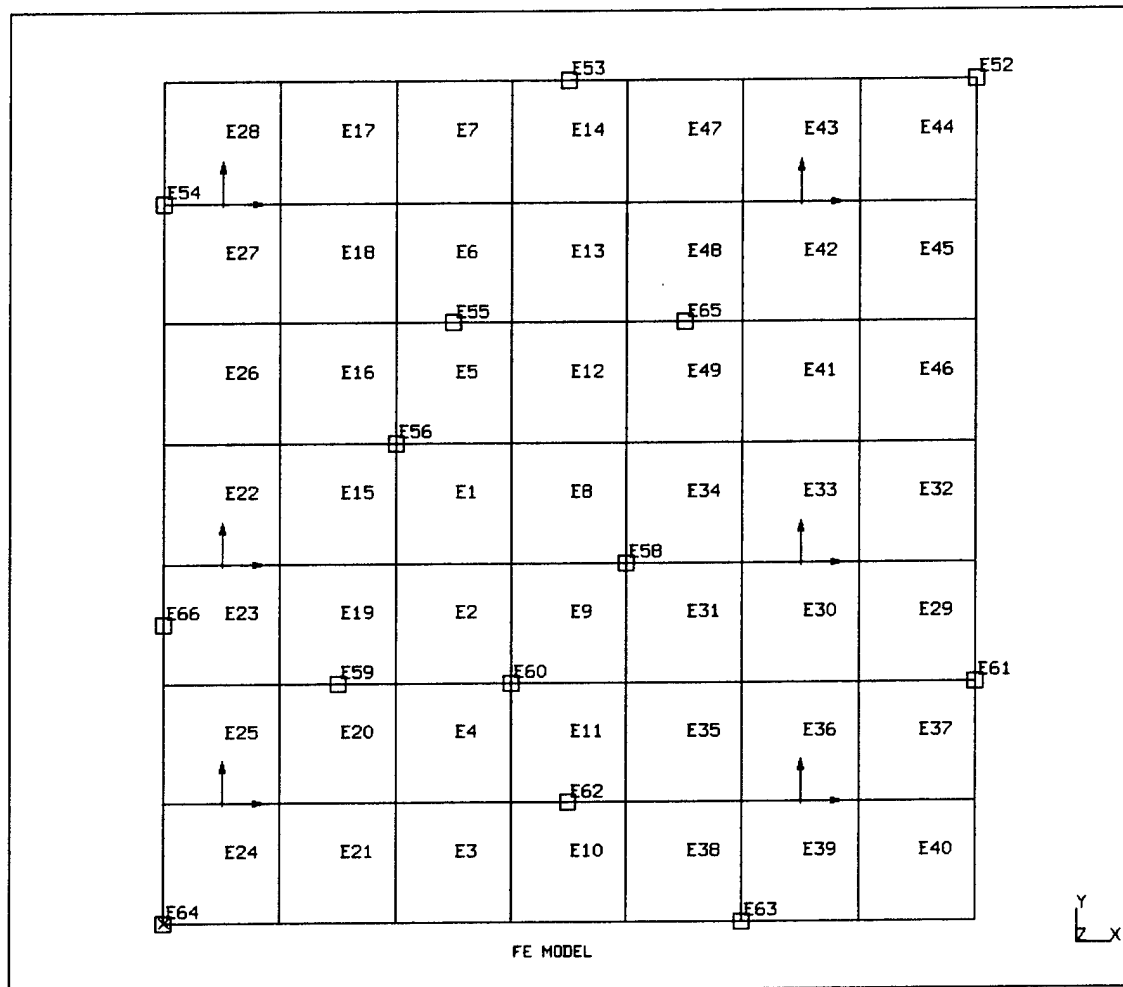
9

Figure 2. Finite Element Model Configuration

10

B. DYNAMIC ANALYSIS OF MODEL

IDEAS Normal Mode Dynamics features three basic algorithms for determining the undamped natural frequencies and normalized mode shapes: Lanzos, Guyan Reduction, and Simultaneous Vector Iteration (SVI). Although all three methods were used on an aluminum beam test case with similar results, the SVI method was chosen for the composite model because it offers several advantages noted below and it is compatible with the IDEAS Optimization routine for model update. SVI is two step inverse power iteration method that solves the eigenvalue problem

$$[k]\{\phi\} = \lambda[m]\{\phi\} \qquad\qquad 5$$

where λ is the square of the natural frequencies and $\{\phi\}$ is the mode shape vector. Appendix F provides details on the mechanics of the SVI method.

The advantages of the SVI method are that it does not contain the errors associated with static condensation, the iteration can be restarted for improved accuracy, and accuracy estimates are available from an iteration history file.

Since the boundary conditions of our test approximated that of a free structure, a free (unrestrained) analysis was performed using "kinematic degrees of freedom", or KDOF. The use of KDOF's are required to account for the singularities introduced by the rigid body modes of an unrestrained structure. The rigid body modes are eliminated from the iteration by partitioning the stiffness matrix into independent and kinematic DOF, where the singularities are all contained in the KDOF partition. Once the rigid body displacements have been calculated using the KDOF subspace, the displacements of the other DOF's can be calculated as linear dependents of the KDOF. Reference 6 contains the details of this procedure.

In order for the rigid body mode elimination procedure to function, the number of KDOF's designated must be greater than or equal to the number of rigid body modes. Six KDOF's were selected at different nodes on the structure such that if these KDOF's represented restraints, the rigid body modes would be eliminated. The KDOF's can be seen as arrows pointing outward from the nodes in Figure 2. The solution was set up to estimate the first 20 bending modes and it converged within

11

ten iterations.

C. THEORETICAL ANALYSIS RESULTS

The analysis identified 20 modes in the 0-1000 Hz frequency range; the first 16 frequencies are shown in Table 1.

Mode	Freq., Hz Initial FE	Freq., Hz FE w/ Trans.
1	73	63
2	108	89
3	133	112
4	184	149
5	188	157
6	317	248
7	334	251
8	336	300
9	358	321
10	411	348
11	541	403
12	548	493
13	598	526
14	645	551
15	664	563
16	690	579

Table 1. Finite Element Model Solution Frequencies

The mode shapes for each frequency were graphically depicted with the IDEAS Post

12

Processing feature. Figures 3 through 5 provide a representative sample. Examination of these mode shapes guided the placement of the suspension lines and transducers as described in the next chapter. After the transducer locations were determined, the effect of these masses was modeled using lumped mass elements and the dynamics solution was run again. The result was a significant downshift in the frequencies, as shown in Table 1. FRF's were generated for a unit excitation using IDEAS Model Response for the selected reference and response locations; a sample FRF for the point inertance (coincident reference and response) at node 176 is shown in Figure 6.

/disk2/hercplate1.mf1
DEFORMATION: 7- B.C. 1,MODE 7,DISPLACEMENT_7
MODE: 7   FREQ: 73.069
DISPLACEMENT - MAG MIN: 3.65E-13 MAX: 6.02E+00
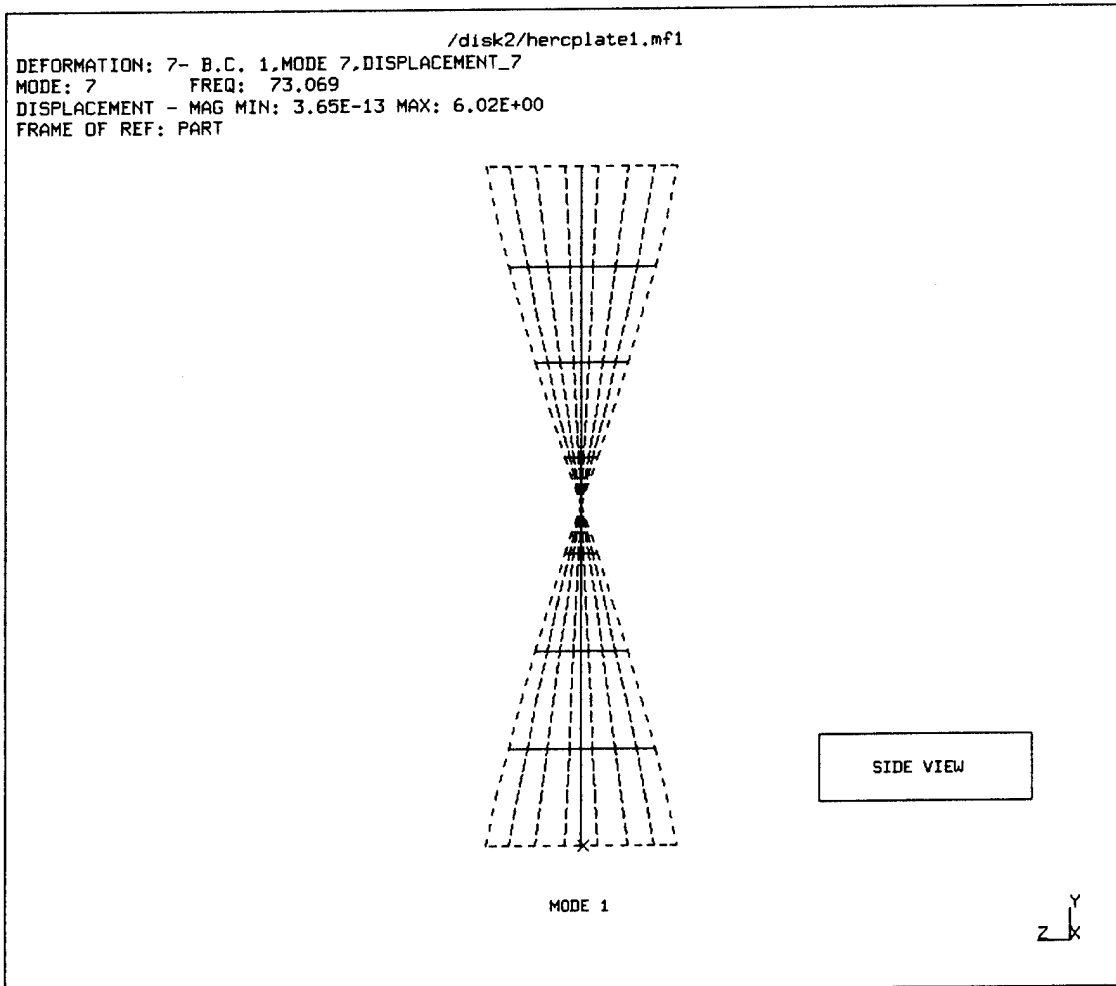FRAME OF REF: PART

SIDE VIEW

MODE 1

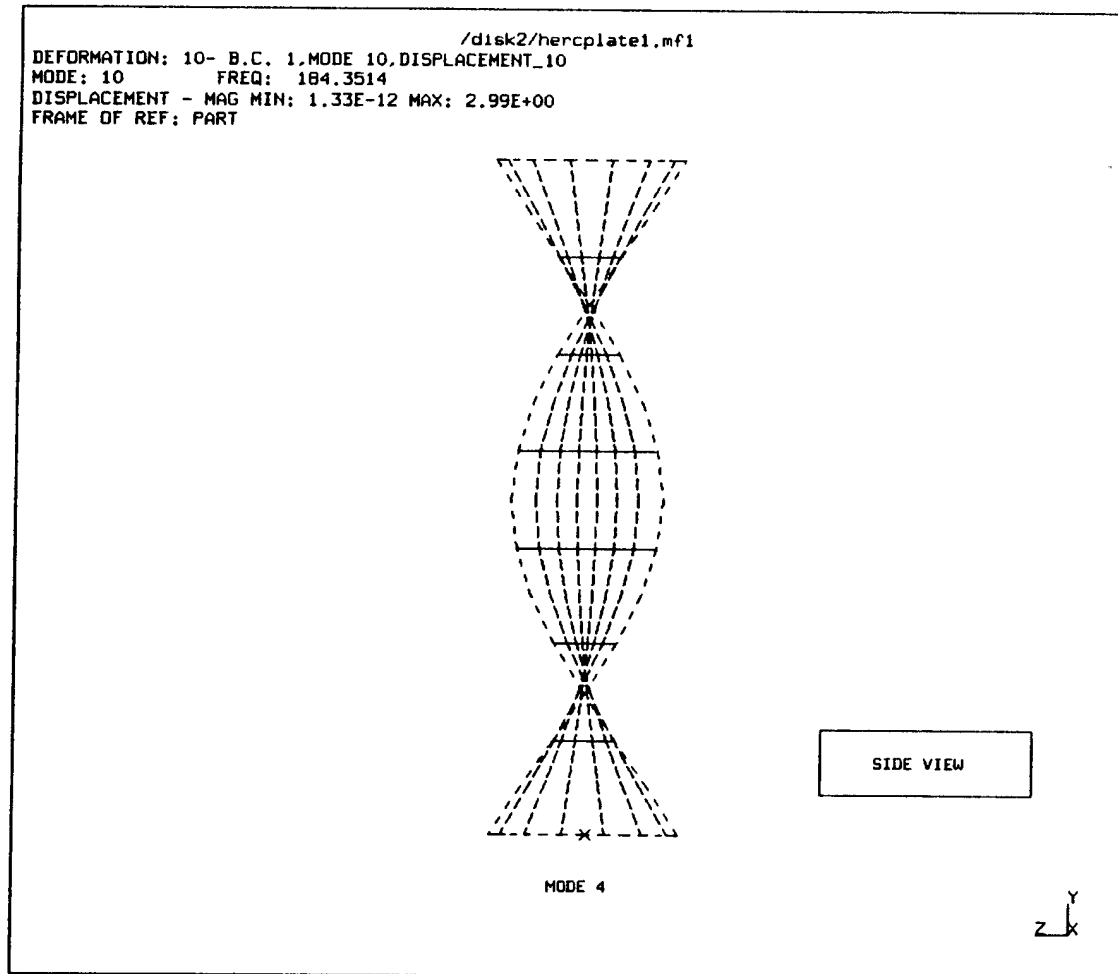Figure 3. Finite Element Model Mode Shape (Mode 1)
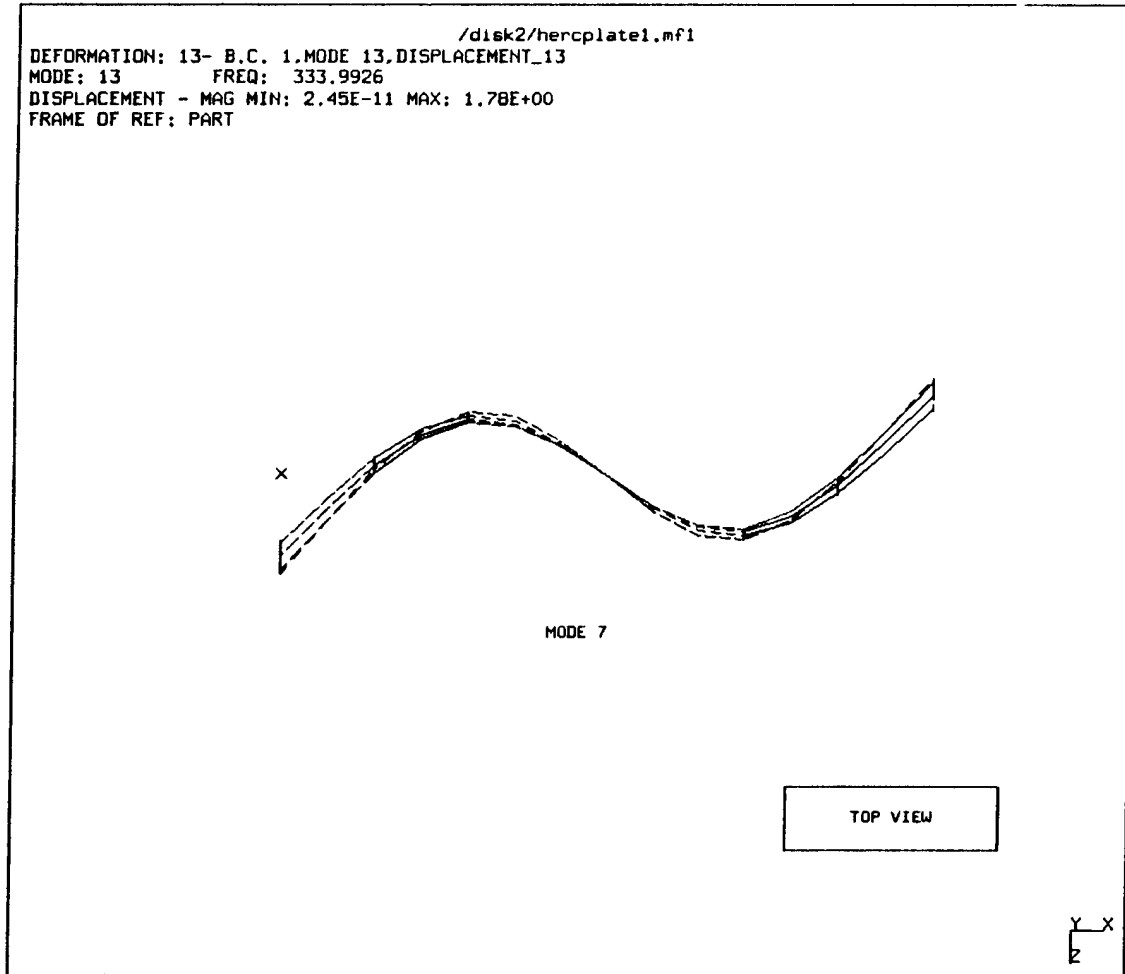
14

Figure 4. Finite Element Model Mode Shape (Mode 4)

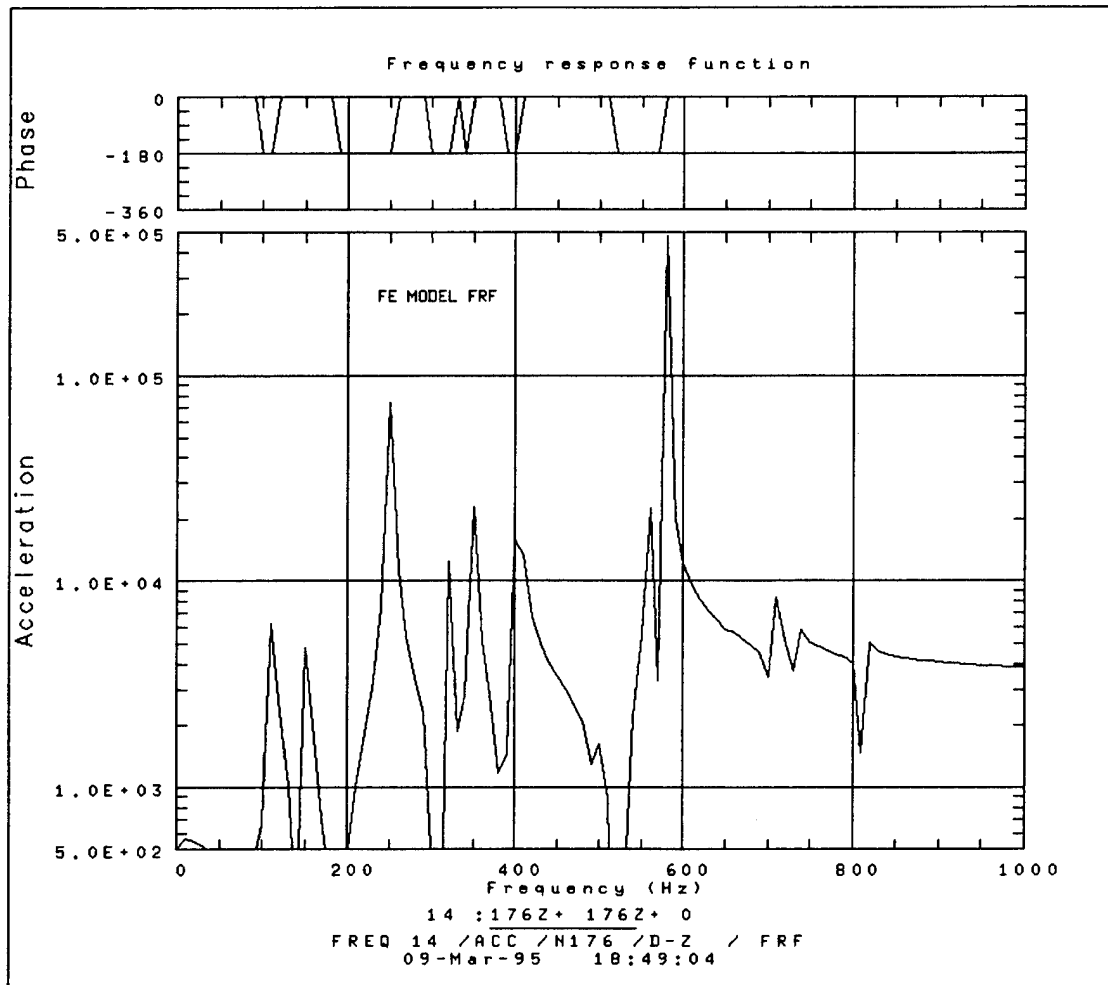Figure 5. Finite Element Model Mode Shape (Mode 7)

Figure 6. Finite Element Frequency Response Function, Node 176

IV. EXPERIMENTAL SET-UP AND PROCEDURES

A. HARDWARE DESCRIPTION

The experimental set-up is depicted in Figures 7 through 9. The major components are the test frame, the shakers and the data acquisition system, each of which is described below.

1. Test Frame and Suspension System

The test frame was constructed using 1.25 inch diameter threaded steel pipe in a rectangular shape with a cross beam to support the test specimen. Teflon paste was used on all threaded joints to provide a solid connection and vibration dampening. Floor flanges attached to each leg supported the frame on a wooden workbench. Rubber matting was placed under each leg to provide some vibration isolation from the shakers. Provisions were made to attach guy wires to the upper corners of the structure in the event that further rigidity was necessary. Two insulated clamps and a series of steel turnbuckles were connected to elastic bands and monofilament line to suspend the test specimen from the cross beam. This system provided a nearly "free" test condition in that the rigid body modes of the test article were at frequencies below 20 % of the first bending mode [Ref. 5]. To ensure minimum interference from the rigid body modes on the first bending mode, the suspension lines were positioned as close to the nodes of the first bending mode as possible, as determined by the FE analysis. This position corresponded to approximately 3 inches from the edges of the plate. As a further measure in achieving the free condition, the test article was suspended in a vertical orientation so that the suspension lines were perpendicular to the primary direction of vibration.

19
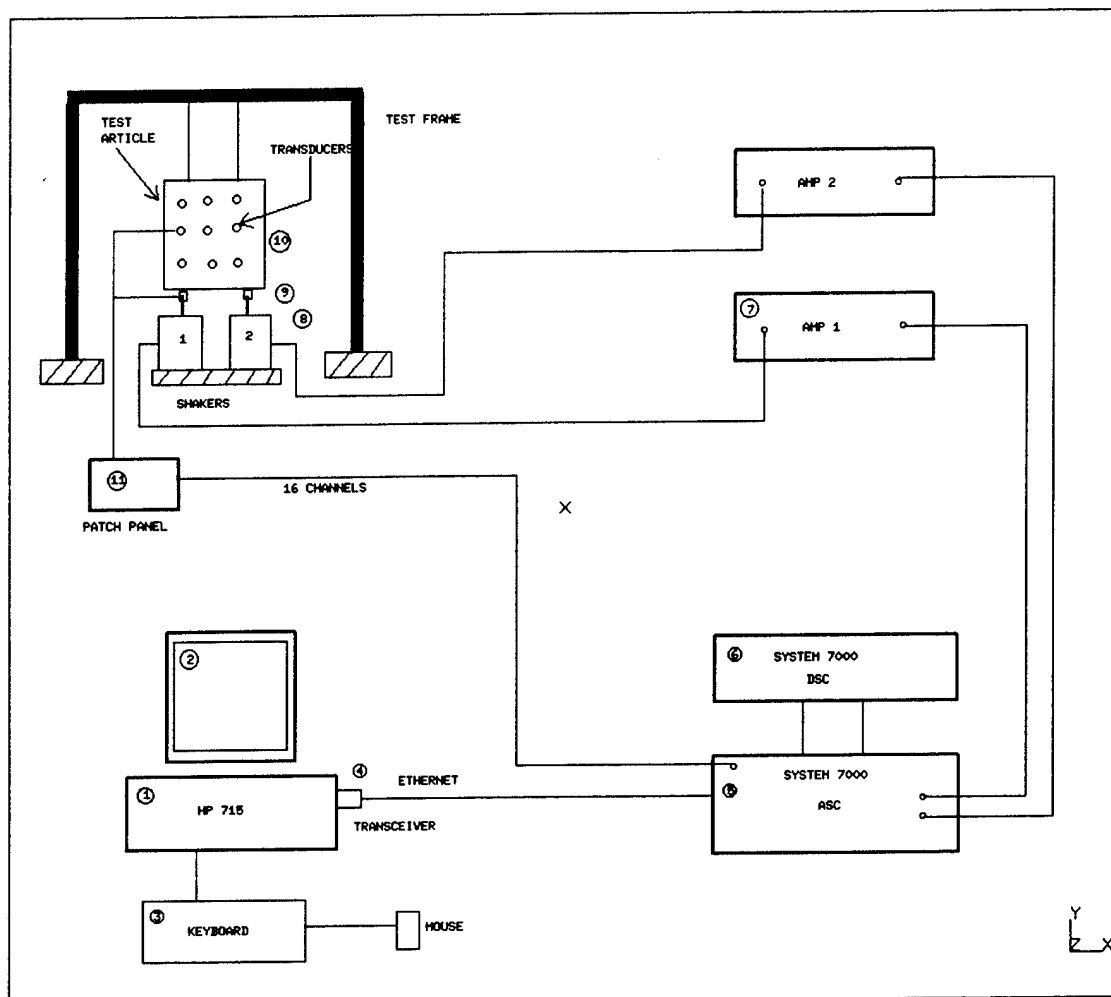
Component Description

1. Hewlett-Packard 715/75 Model A2896A Workstation
2. HP A2094A 19" Color Monitor
3. HP C1429B Keyboard
4. 10-Base 2 Ethernet Transceiver
5. Zonic System 7000 Analog Signal Chassis Model 7014
6. Zonic System 7000 Digital Signal Chassis Model 7015
7. Techron Model 7521 Power Amplifier (2)
8. Ling Electronics Model 207 Shaker (2)
9. PCB ICP Model 208B Force Transducer (2)
10. PCB ICP Model 336C34 Acceleration Transducer (14)
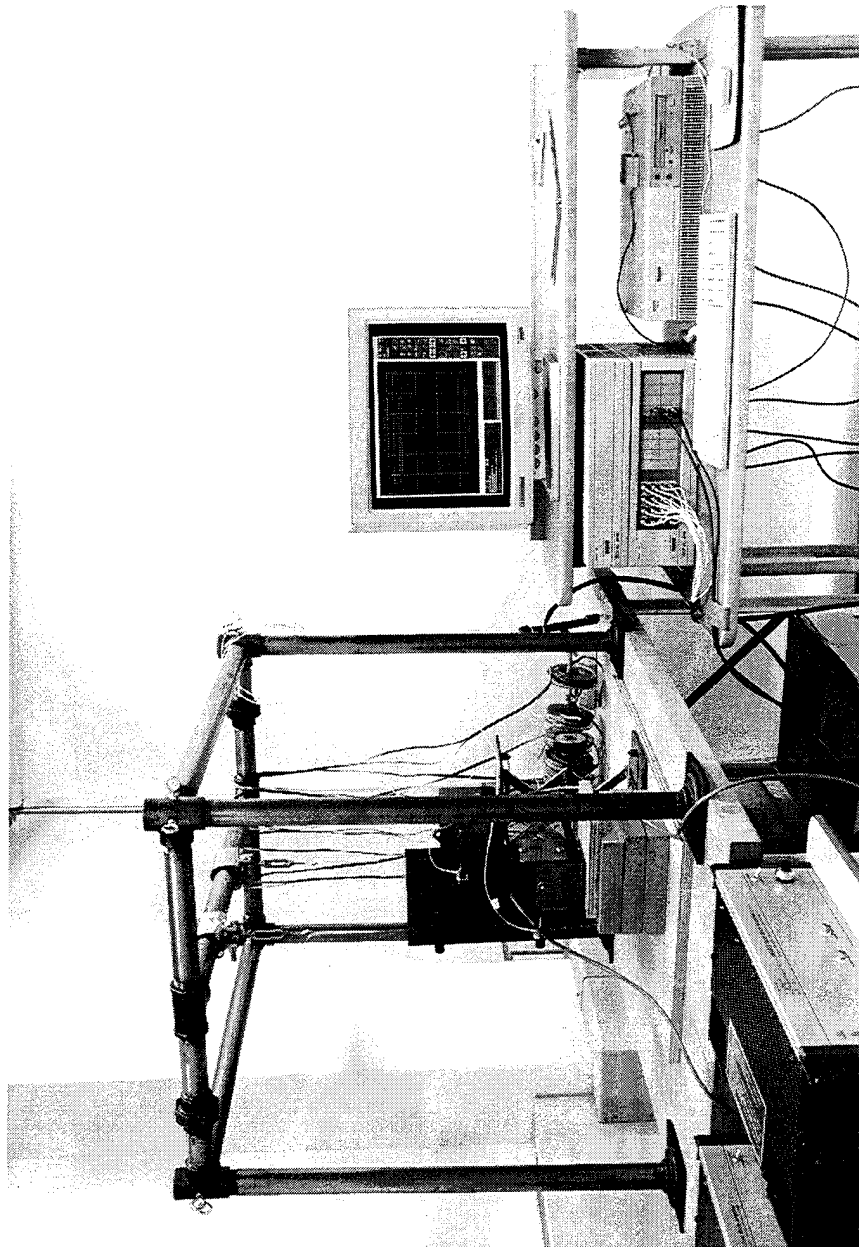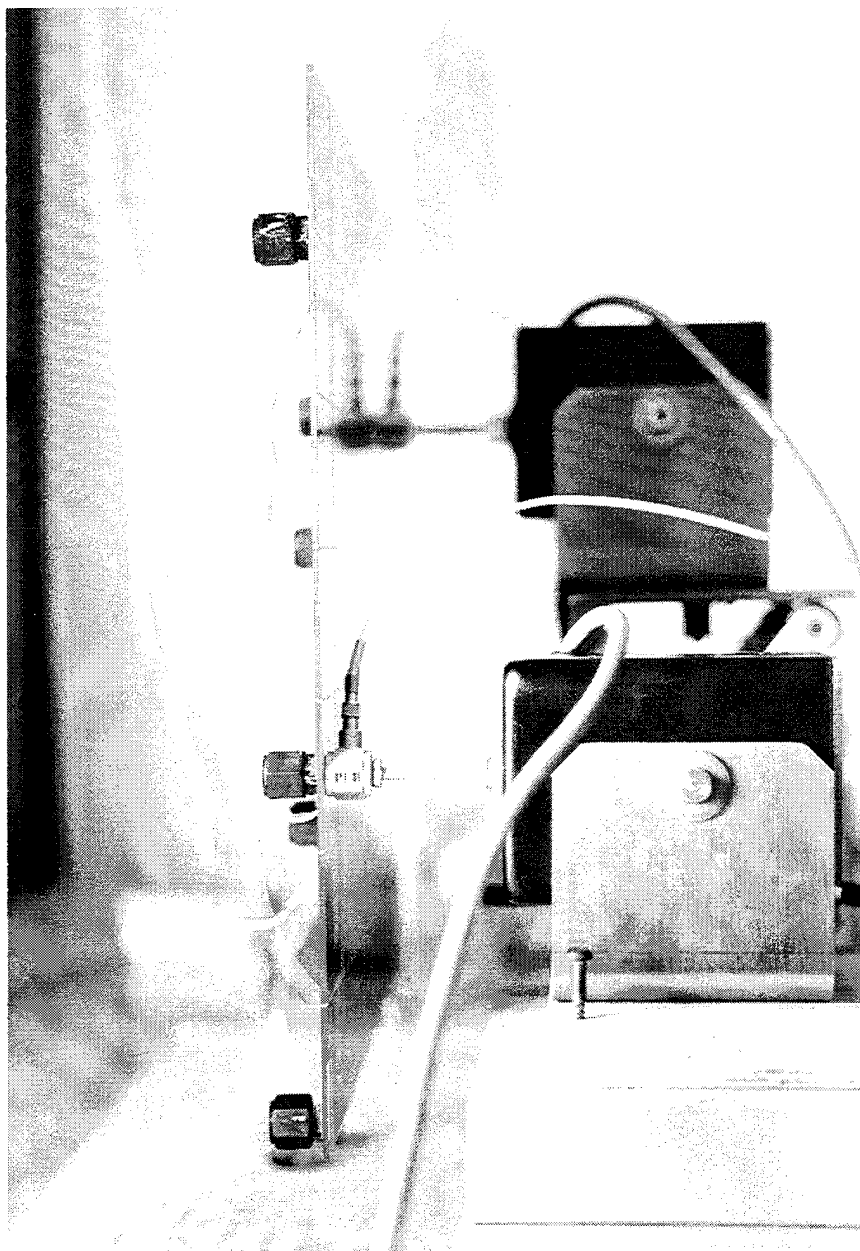11. PCB Model 070C29 Patch Panel

Figure 7. Experimental Set-Up

20

Figure 8. Experimental Layout

Figure 9. Test Specimen and Shakers

2. Shakers and Power Amplifiers

Excitation force was provided using two identical Ling Electronics Model 207 electrodynamic shakers with an rms force output of 5 lbf in the random mode, a 90 g peak acceleration, and a frequency range of DC-10,000 Hz. The shakers' resonant frequency was approximately 7.5-8 kHz, far outside the range of our application. The shakers were mounted in a trunnion frame that allowed the shaker armature mounting surface to be swiveled 90 degrees to the horizontal position. Force was applied using "stingers" made from 3 inch threaded steel rods which were inserted into the internal threads of the armature mounting surface. The free end of the stingers were screwed directly into the threaded receptacles of the force transducers.

The shakers were each powered by separate Techron Model 7521 amplifiers capable of delivering a maximum voltage gain of 26.3 +/- 0.3 dB at 150 watts (2 ohm load) and with a frequency response of DC to 35 kHz. The amplifiers received the excitation signals from the output module of Zonic System 7000 and applied the amplified signals directly to the shakers.

3. Transducers

Force and acceleration measurements were acquired through the use of two PCB ICP Model 208B quartz force transducers and 14 PCB ICP Model 336C34 quartz acceleration transducers. The force transducers had a working range of 0-10 lbf and .01-14,000 Hz and a sensitivity of 500 mV/lbf. The accelerometers had working ranges of 0-500 g's and 2-5000 Hz and a sensitivity of 10 mV/g. Calibration of these sensors had been accomplished by PCB within six months of the experiment and calibration data was provided for each transducer. The ICP (Integrated Circuit Piezoelectric) sensors use the piezoelectric effect of a quartz crystal to generate a charge signal proportional to the applied force or acceleration. The PCB sensors have built-in signal conditioning electronics to convert the high impedance piezoelectric signal to a low impedance voltage signal that can be effectively transmitted to the signal analyser. The transducers require a constant 20 VDC from the signal analyser to operate.

The accelerometers were attached to the test article using Petrowax, which provides adequate adhesion with a minimum of output distortion in the frequency range of interest (less than 2 % below 1000 Hz). The use of Petrowax allowed easy removal and relocation of the accelerometers. The accelerometers were connected to a patch panel via lightweight cable with modular connections at both ends. The patch panel was connected to the Zonic System 7000 via a 16 channel coaxial cable with separate BNC connectors. The force transducers were mounted directly to the test specimens using double sided adhesive tape. The force transducers were connected to the patch panel via general purpose coaxial cable.

4. Signal Analyser

A Zonic System 7000 signal processor provided multi-channel data acquisition, real time Fast Fourier Transform signal analysis, and source signal generation. The System 7000 consisted of an analog chassis and a digital chassis, with the following functions.

a. Analog Chassis

The analog chassis contained the Analog Signal Conditioning Input (ASC-I) module and the Analog Signal Output (ASC-O) module. The ASC-I performed the data acquisition including anti-alias filtering, overload detection, amplitude range selection and digitizing of the analog input signals. It processed 16 input channels up to 5 KHz, with separate A to D conversion for each channel in a parallel arrangement. Filtering was accomplished automatically as a function of the sampling rate, and was identical for all 16 channels. The digitized, differentially balanced signal was passed to the digital chassis via a 25 pin RS-422 connector.

The ASC-O received digital source signals from the digital chassis and converted them to analog signals which were output through BNC connectors. The model used in the experiment had a maximum of two output channels available. The analog output signals were sent through the amplifiers and on to the shakers to produce the excitation. The system was capable of generating sine, random, pseudo random, and burst random output signals.

b. Digital Chassis

The digital chassis contained the Digital Signal Conditioning Input (DSC-I) module, the Digital Signal Conditioning Output (DSC-O) module and the Digital Signal Processing (DSP) module. The DSC-I provided digital filtering, buffering, gain/offset management, zoom processing, trigger control and ASC-I control functions via integer array processors. It provided data in a parallel digital format to the DSP for processing.

The DSC-O generated specified waveforms in a digital format and fed them to the ASC-O where they were converted to analog signals. It also provided digital filtering, bursting and ramping of the output signals and interfaced with the DSP for control of the ASC-O.

The DSP provided windowing, signal averaging, trigger control and performed variable block size FFT for each input channel. It interfaced with the host computer via an Ethernet Nodem and controlled the functions of the DSC's.

5. Host Computer

The data acquisition system was controlled by a Hewlett-Packard 715/75 Model A2896A Workstation configured with two 1 GB hard drives and a 19 inch color monitor. The computer communicated with the System 7000 signal analyser via a 10-base-2 ethernet cable and transceiver. HP-UX, the Hewlett-Packard version of Unix, and HPVUE (XWindows) were used as the operating system on which Structural Dynamics Research Corporation (SDRC) IDEAS was loaded. IDEAS is a structural analysis software application capable of performing design, drafting, finite element modeling, dynamic analysis, and testing. It was used to control the experiment, acquire the data, and conduct post test analysis. Test data and finite element analysis results were stored on one of the two internal hard drives. A DDS SCSI-2 tape drive was used to back up the data collection.

B. PRE-TEST ANALYSIS

A number of trial tests were conducted using isotropic aluminum and plexiglass plates to determine the optimum choice of data acquisition parameters, excitation signals, and test article suspension configuration.

1. Excitation Signal

Various forms of excitation signals were available with the hardware and software configuration, including sine, pure random, burst random and periodic random (swept sine is not available for multiple input configurations in IDEAS). Based on Reference 12, which provides a survey of these types of signals, and some experimentation with the different signals, burst random excitation was chosen. It provides excitation in all frequency ranges of interest and is much less time consuming than a manual sine sweep of the frequencies. There was very little difference in the FRF's generated from a single input swept sine and the random excitation, provided measurement frame averaging was utilized. Figure 10 is a comparison between FRF's produced by swept sine and random excitation for a plexiglass beam, where the swept sine resolution was 10 Hz. Burst random excitation was utilized to combat leakage problems since the signal is brought to zero well before the end of the measurement frame.

As discussed in references 5 and 12, it is important to have uncorrelated excitation signals when using multiple inputs. This is due to the procedure by which the FRF's are derived from random excitation. Appendix H gives the mathematical development, but suffice it to say here that the FRF's are generated from the transfer functions between the input and response spectral densities, cross spectrums, or both. If the off diagonal terms of the input cross spectrum are not zero (indicating correlated inputs), inaccuracies in the FRF calculations can result. The Zonic signal analyser provided two uncorrelated random source signals that met this criteria.

2. Data Acquisition Parameters

The IDEAS Testing and Zonic System 7000 configuration offers a wide variety
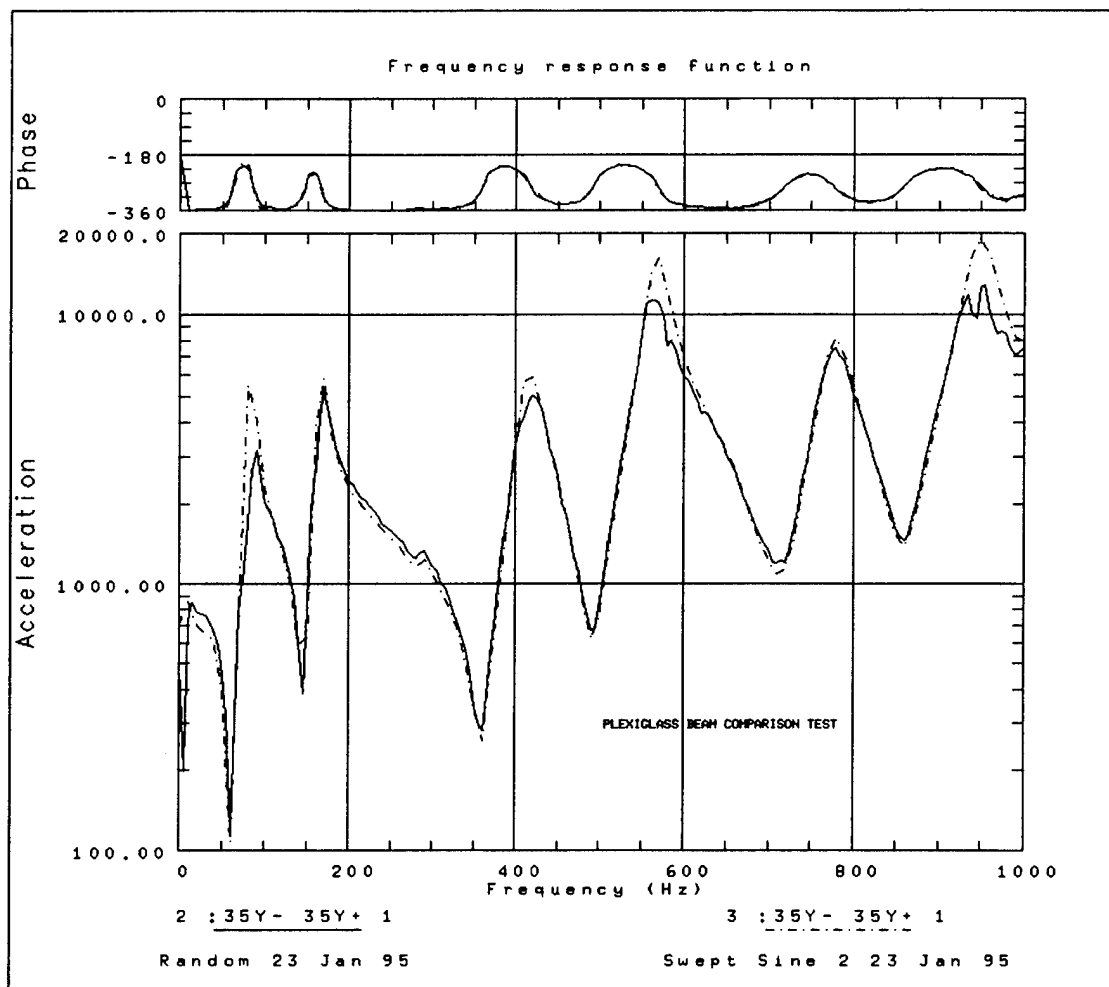
Figure 10. Sine vs. Random Excitation Comparison, Plexiglass Beam

of signal acquisition and processing options, including anti-aliassing, windowing, frame averaging and FFT analysis methods. After some experimentation with various combinations of the available acquisition parameters, the following settings were found to produce the best combination of high signal to noise ratio and reproducibility. Appendix I provides the specific acquisition settings for the test runs used in the analysis.

a. Windowing

A Hanning Broad window provided low leakage and good frequency definition.

b. Averaging

Frame averaging with automatic rejection of frames with out of range signals was utilized; 20 frames were averaged for each acquisition.

c. Spectral Lines / Sampling Rate

801 spectral lines were used over the 1000 Hz frequency range of interest, corresponding to a frequency resolution of 1.25 Hz. The sampling rate was fixed by the number of spectral lines and the Niquist criteria to 2560 samples per second with a frame length of 0.8 seconds. Total test time with 20 frames was then 16 seconds.

3. Sensor Location

The finite element model analysis provided the means to determine the best positions for the sensors. Essentially, the exciter locations were chosen such that they were not coincident with any of the nodes predicted by the FE mode shapes. Accelerometer locations were arranged to give a good spacial representation of the structure by spreading them out over the surface without regard to symmetry. Locations of both force and acceleration transducers are shown in Figure 11.

4. Frequency Range

The frequency range on which to focus our analysis was also determined by the finite element model. The desired characteristics were well defined modes that
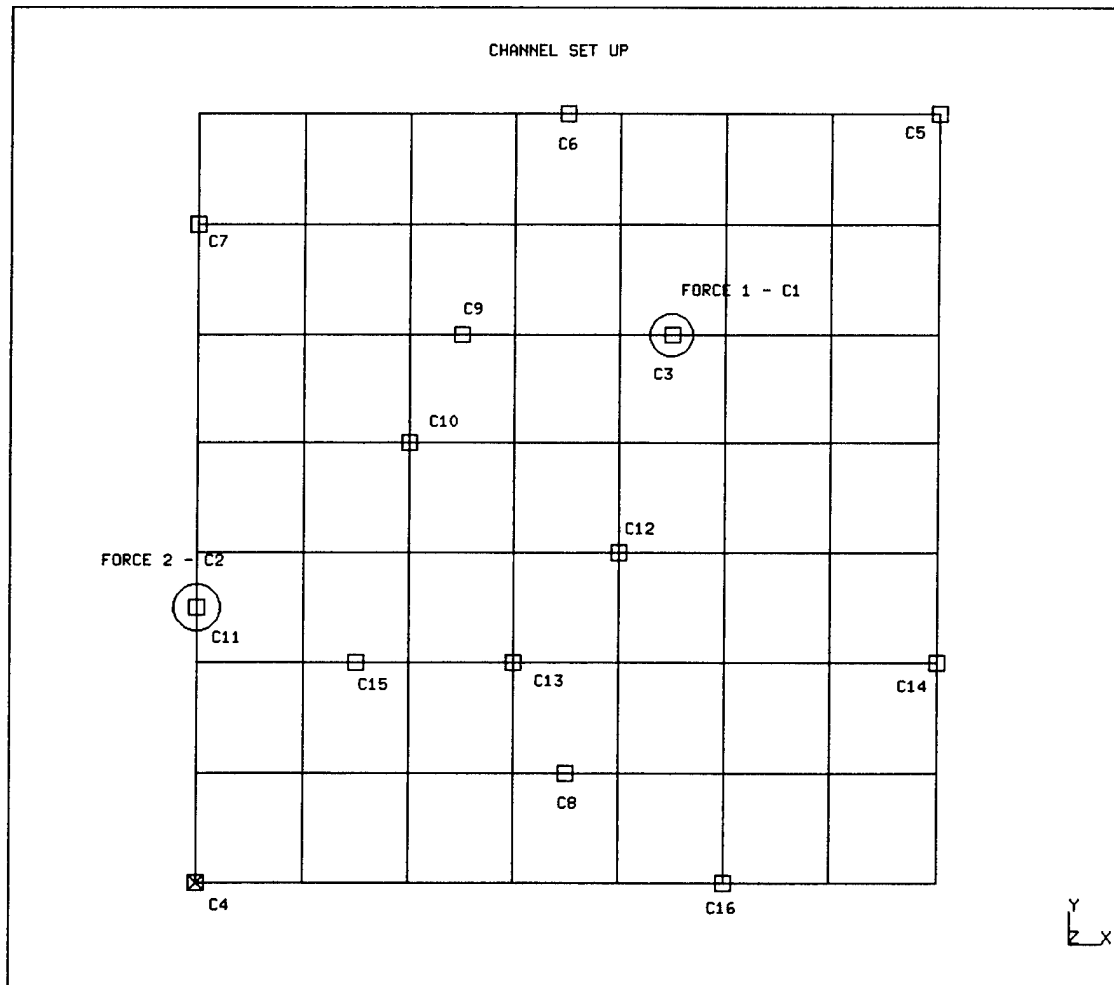
Figure 11. Transducer Locations and Channel Assignment

29

were not unduly influenced by residual stiffness or inertia. Rigid body modes were not of interest so that a low frequency cut-off was established at 20 Hz. By examining the FRF's generated from the theoretical analysis, it was decided that the first 16 modes met the above criteria and the upper frequency cut-off was therefore set at 1000 Hz.

C. TEST PROCEDURES

1. Calibration

Prior to conducting the experiment the system was run through a calibration sequence on two levels. First, the Zonic System 7000 was calibrated internally using a standard routine from the IDEAS Test interface that uses an internal calibration signal to set gain control and phase offset. Second, the individual transducers were calibrated by setting scale factors in a mass calibration technique described in Appendix J.

2. Data Collection

After calibration, the transducers were connected to the test article as described in Section A above. The experiment was controlled from the IDEAS Test interface, which allowed for various options on how the data was collected and stored. Of the 16 available input channels, two were designated as reference (force input) channels and the remaining 14 were designated as response (acceleration) channels. The IDEAS input channel configuration scheme allowed the individual transducer sensitivities to be set for each channel. Data acquisition parameters were set as discussed in Section B above and are listed in Appendix I. The source signals were started and data was acquired, with the actual data collection lasting approximately 16 seconds. Real time signals were displayed for all 16 channels during the test. Time histories of the data were not stored; rather, the FRF's for each reference-response pair (28 total) were automatically computed and available for display and storage.

3. Initial Reproducibility Assessment

Multiple runs for each test specimen were conducted, stored and compared to ensure reproducibility (11 tests were stored for the HLU, 9 for the MLU). Figure 12 shows an overlay of two FRF's for the HLU from different tests and shows the degree of reproducibility obtained. Figure 13 is a similar overlay from two different MLU tests. In this case, all transducers had been removed and the plate had been disconnected from the test fixture between tests. (Both Figures 12 and 13 are point inertances for node 52, where "node" refers to the FE model node. (See Figure 11 for location.) The frequencies at all modes appear to correlate very well; however, differences in amplitude were noted for some modes as shown in both Figures 12 and 13. These differences in amplitude represent the baseline error for the experiment. A more quantitative error assessment is made in the following section.

Tests were run using two different methods for computing the FRF's (H_1 and H_v, as discussed in Appendix H) and compared, with little discernable difference noted in amplitude and sharpness of peaks, as shown in Figure 14. In general, the H_1 FRF's appeared to be of better quality (less noise) and were used for extraction of modal parameters.

D. RESULTS AND ANALYSIS

1. General Comparison Between Specimens

With sets of 28 FRF's for each test collected and stored, an analysis of the data commenced. Figure 15 shows an overlay of the point inertance FRF's for node 176 for each plate. Figure 16 is a similar plot for node 52. Because of the density of modes and the fact that the higher frequency modes were less well defined, the analysis was confined to the 20-600 Hz range, in which approximately 16 well defined modes can be discerned.   The overlays in Figures 15 and 16 indicate an appreciable difference between the two FRF's in amplitude, phase, and frequency.   In order to quantify and substantiate these differences over all reference locations, the analysis proceeded to extract the modal parameters of each plate.
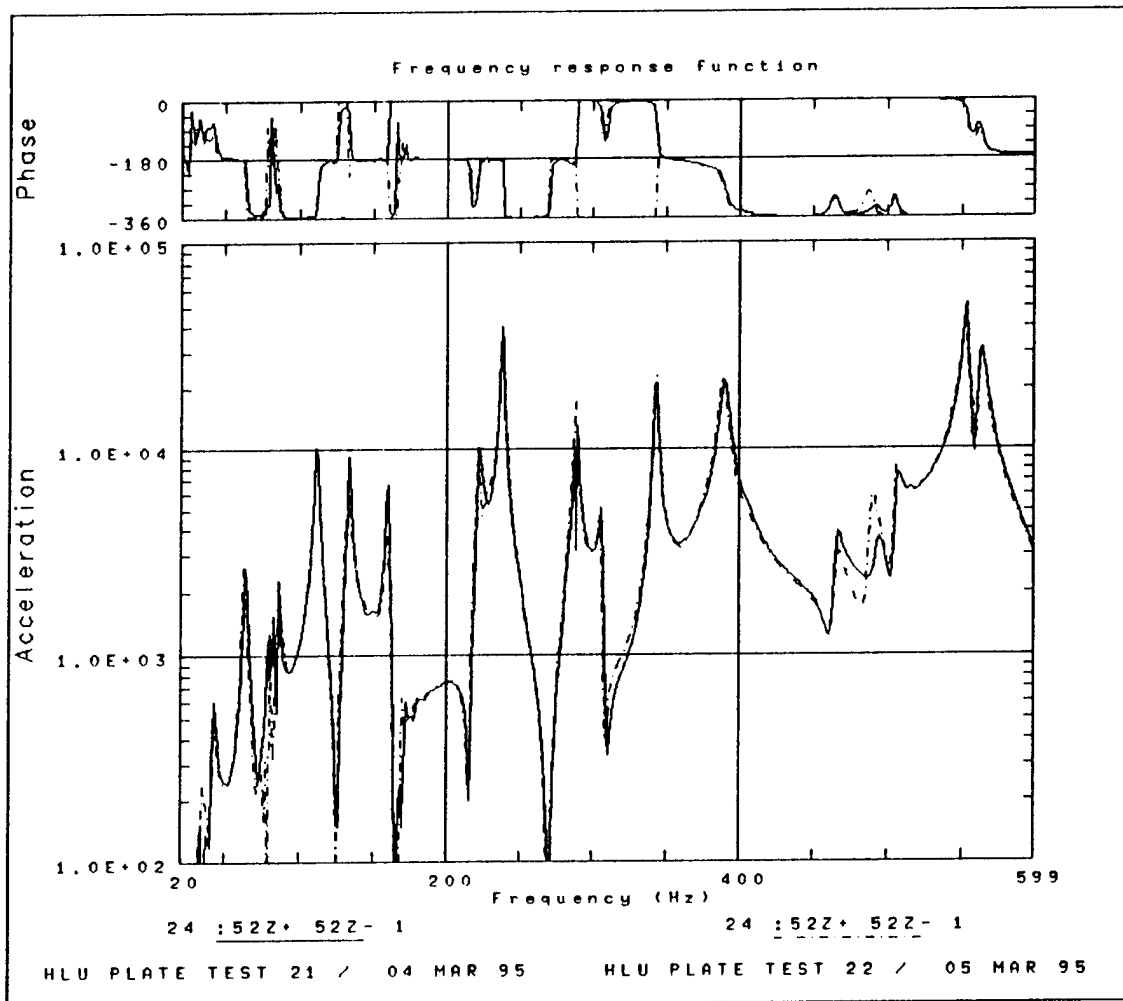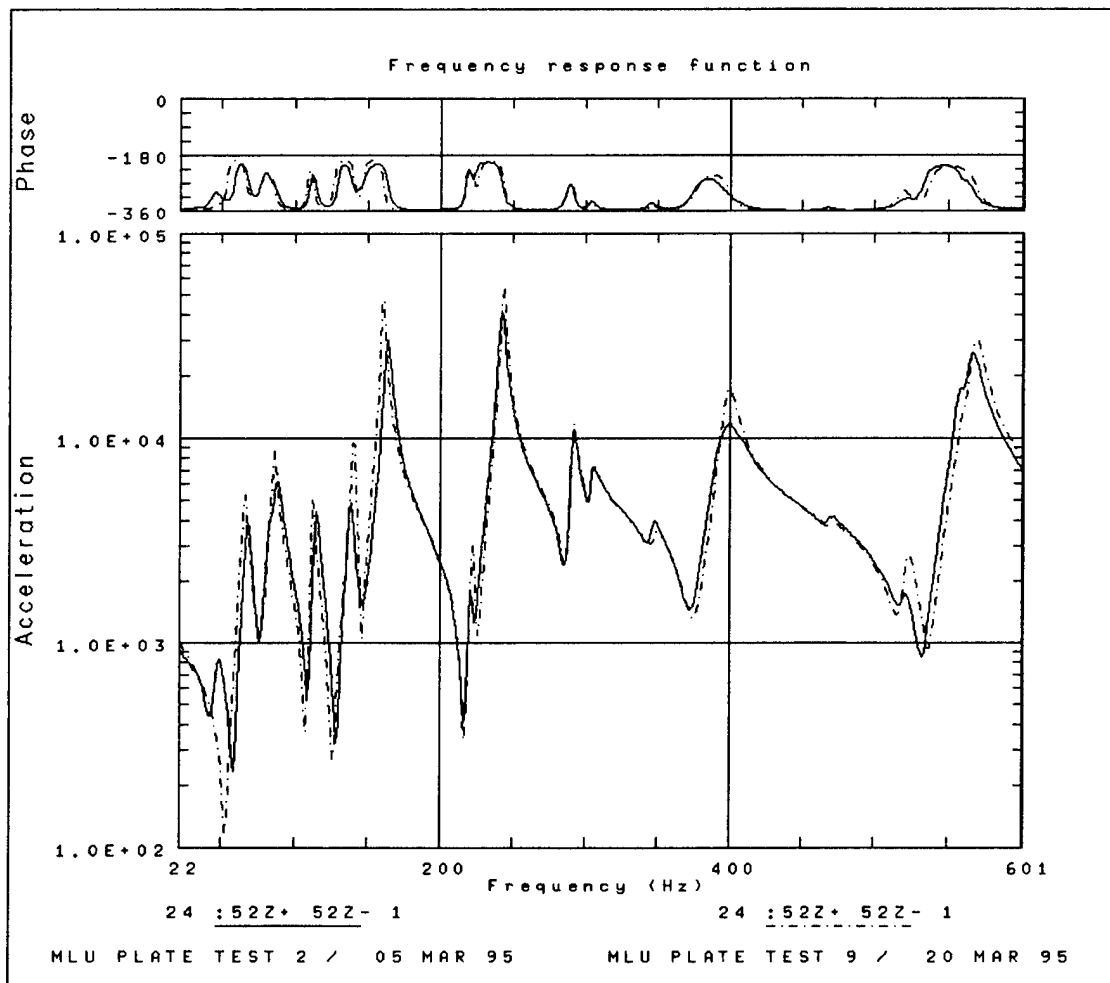
31

Figure 12. HLU FRF Reproducibility, Node 52

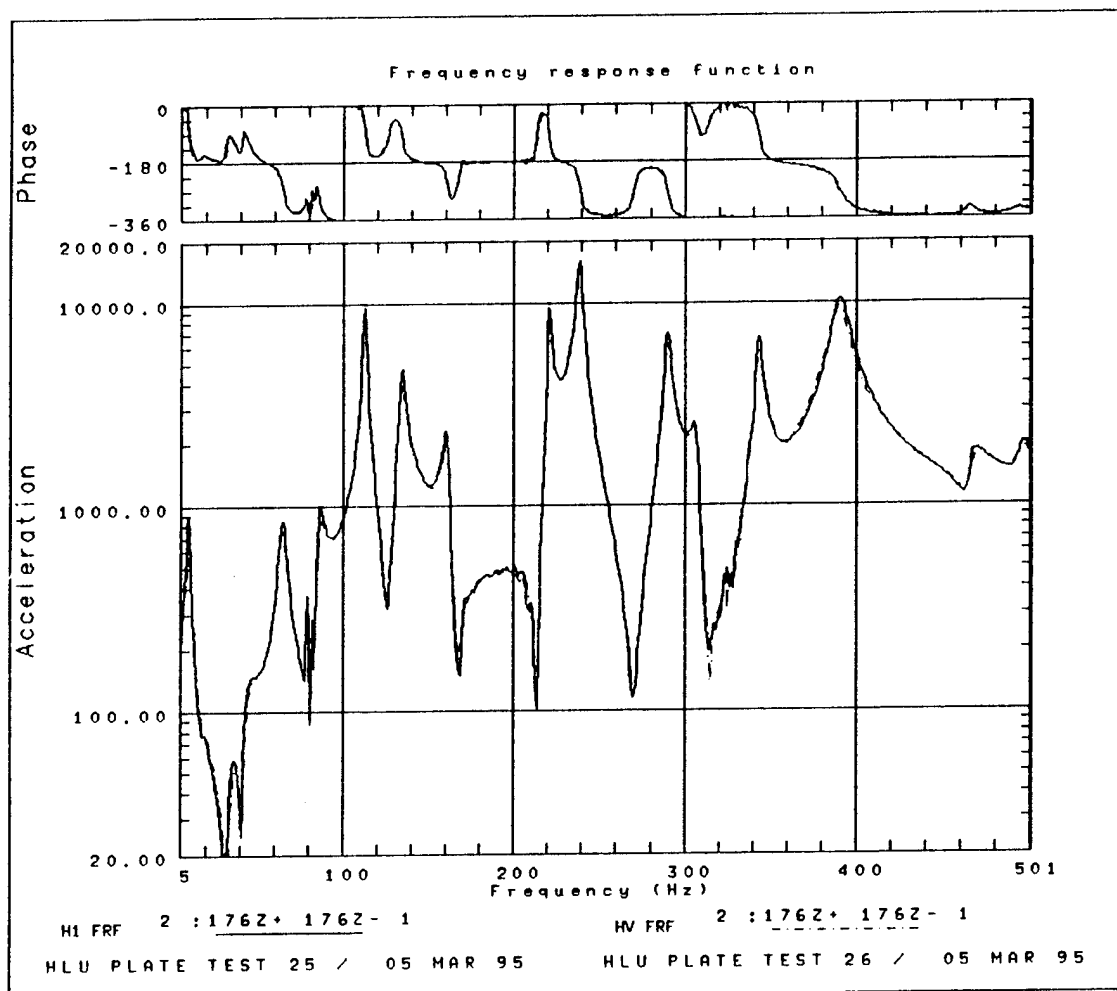Figure 13. MLU FRF Reproducibility, Node 52

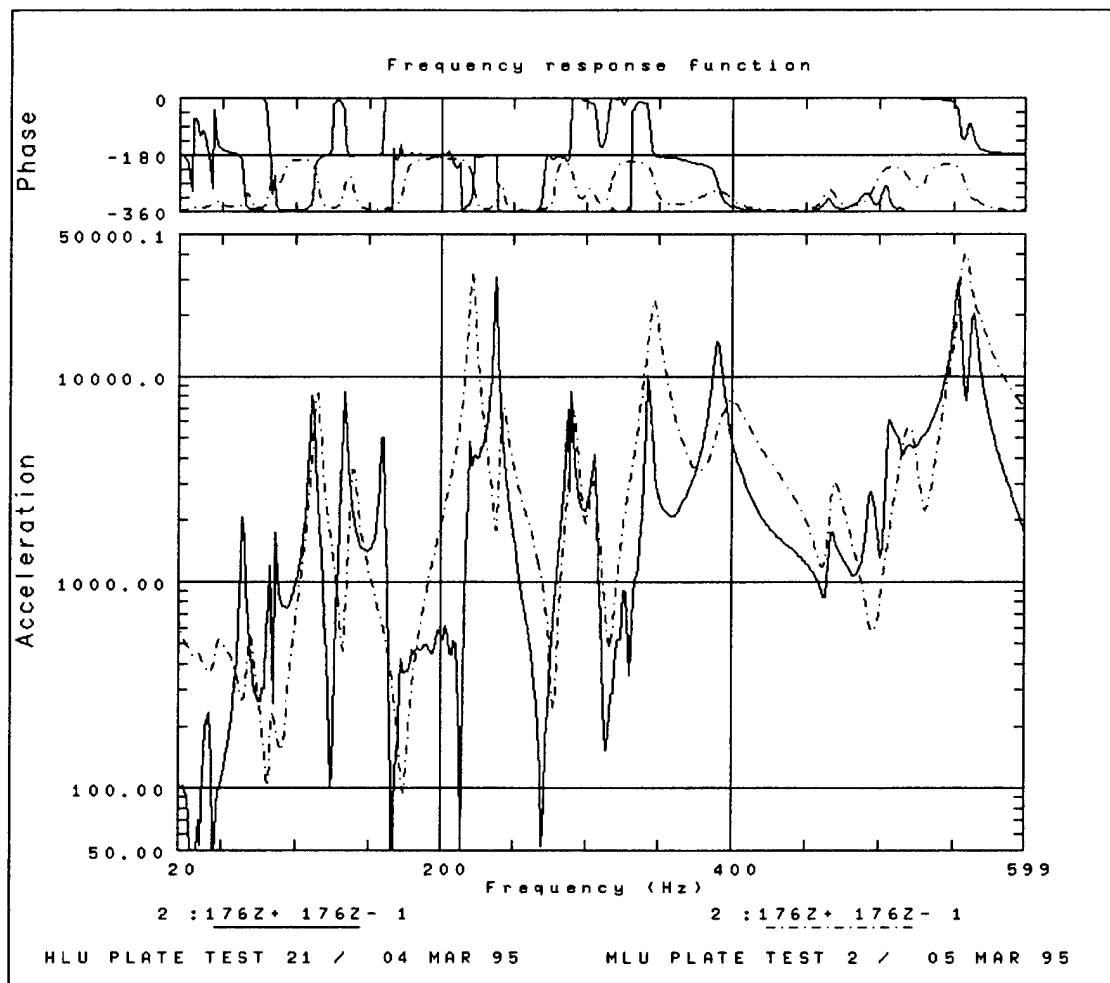Figure 14. H_1 and H_v FRF Comparison, Node 176
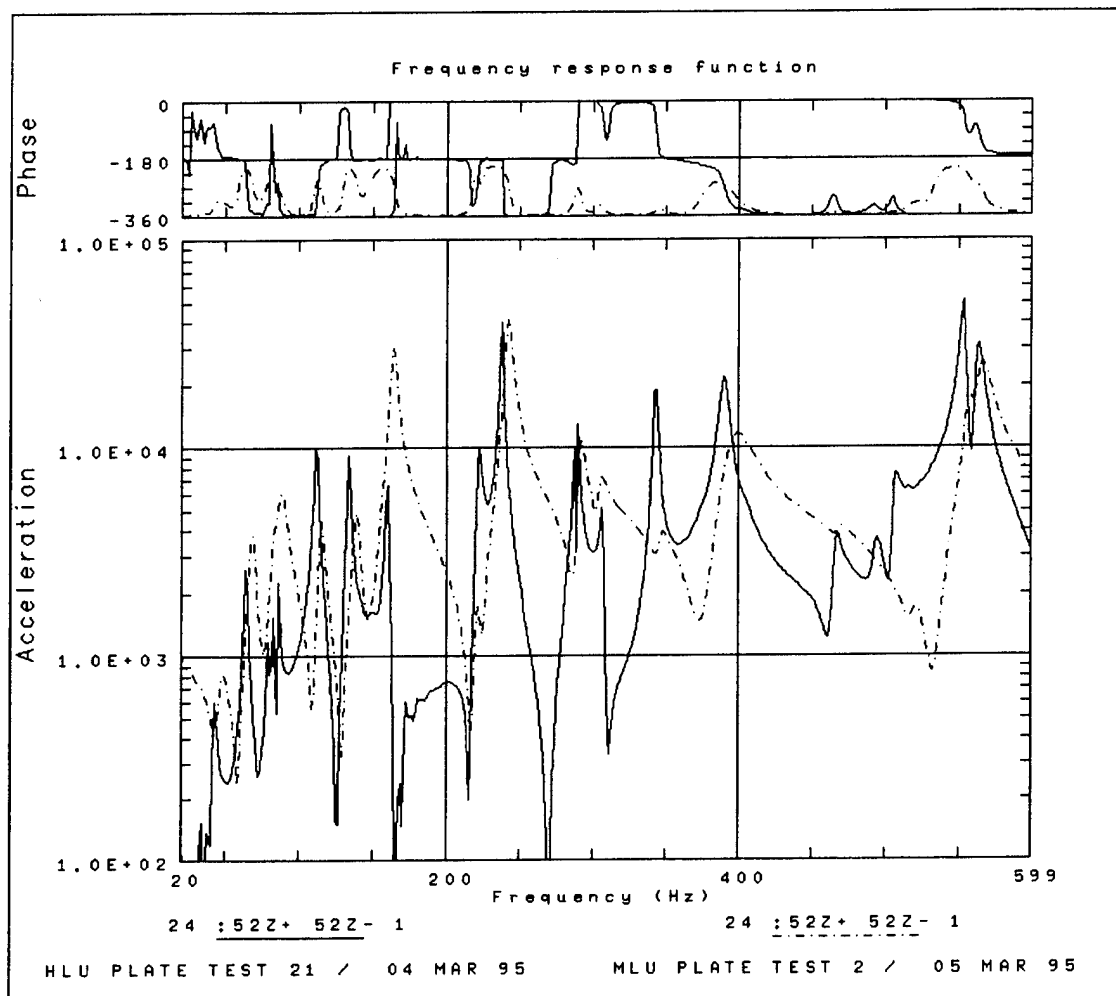
34

Figure 15. HLU/MLU FRF Comparison , Node 176

35

Figure 16. HLU/MLU FRF Comparison , Node 52

2. Extraction of Modal Parameters

The extraction of the modal parameters was accomplished entirely within IDEAS Modal Analysis and involved a number of steps including using a Multivariate Mode Indicator Function (MMIF); building the FRF matrix; estimating the natural frequencies, damping ratios, and modal constants (residues); generating the analytic functions that model the FRF's; and, finally, calculating a set of mode shapes. The Polyreference curve fitting technique was utilized to estimate the natural frequencies and damping ratios and the Frequency Polyreference Residue technique was used to calculate the residues and mode shapes. The Polyreference techniques obtain global least squares estimates of the modal parameters by processing all the FRF's simultaneously. The Frequency Polyreference Residue technique has the advantage of operating in the frequency domain so that residual inertial and compliance terms can be added to account for the effect of modes outside the frequency range of interest. A more detailed explanation of the procedure is presented in Appendix B.

The end result of the extraction procedure is a parameter table listing the natural frequencies, damping ratios, and residue amplitudes and phases for each identified mode. An analytic expression for the FRF is generated from these parameters to check the fit with the measured FRF. Figures 17 and 18 show the analytically derived functions and the measured counterparts at node 52 for the HLU and MLU, respectively.

Included in the parameter table is a Modal Confidence Factor (MCF), which is a numerical value from 0 to 1 that can be used to discriminate between computational (false) modes and physical (true) modes. Computational modes are generated by the curve fitting algorithm to account for unwanted effects of noise, leakage, and nonlinearities and do not represent physical modes. An MCF close to 1 indicates a physical mode, while an MCF less than one indicates a computational mode. This feature allows easy filtering of computational modes by setting a MCF threshold value for the parameter table. Setting an MCF threshold of 0.95 resulted in 16 modes in the 0-600 Hz region for both HLU and MLU tests. The resulting parameter tables for the
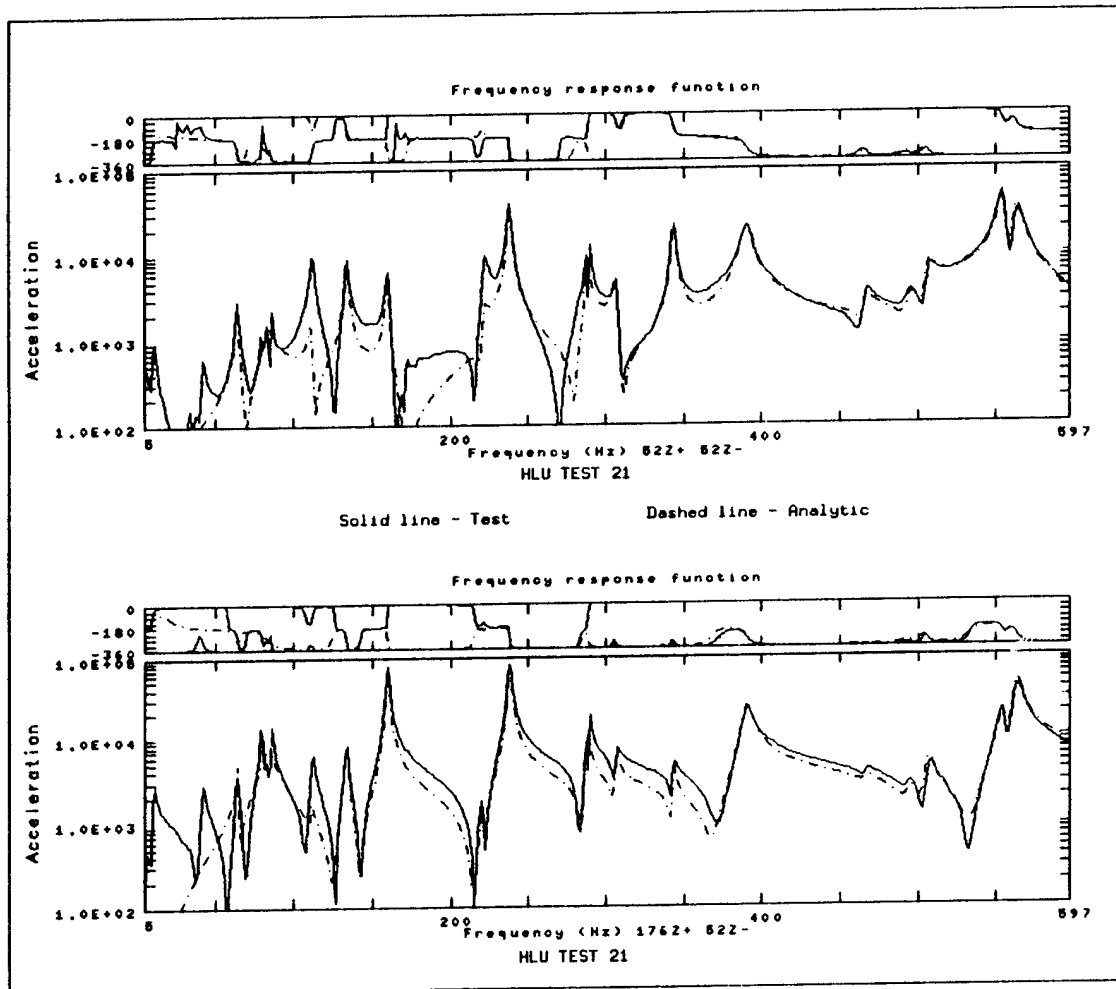
37

Figure 17. HLU Analytic FRF (Dashed) and Measured FRF (Solid), Node 52
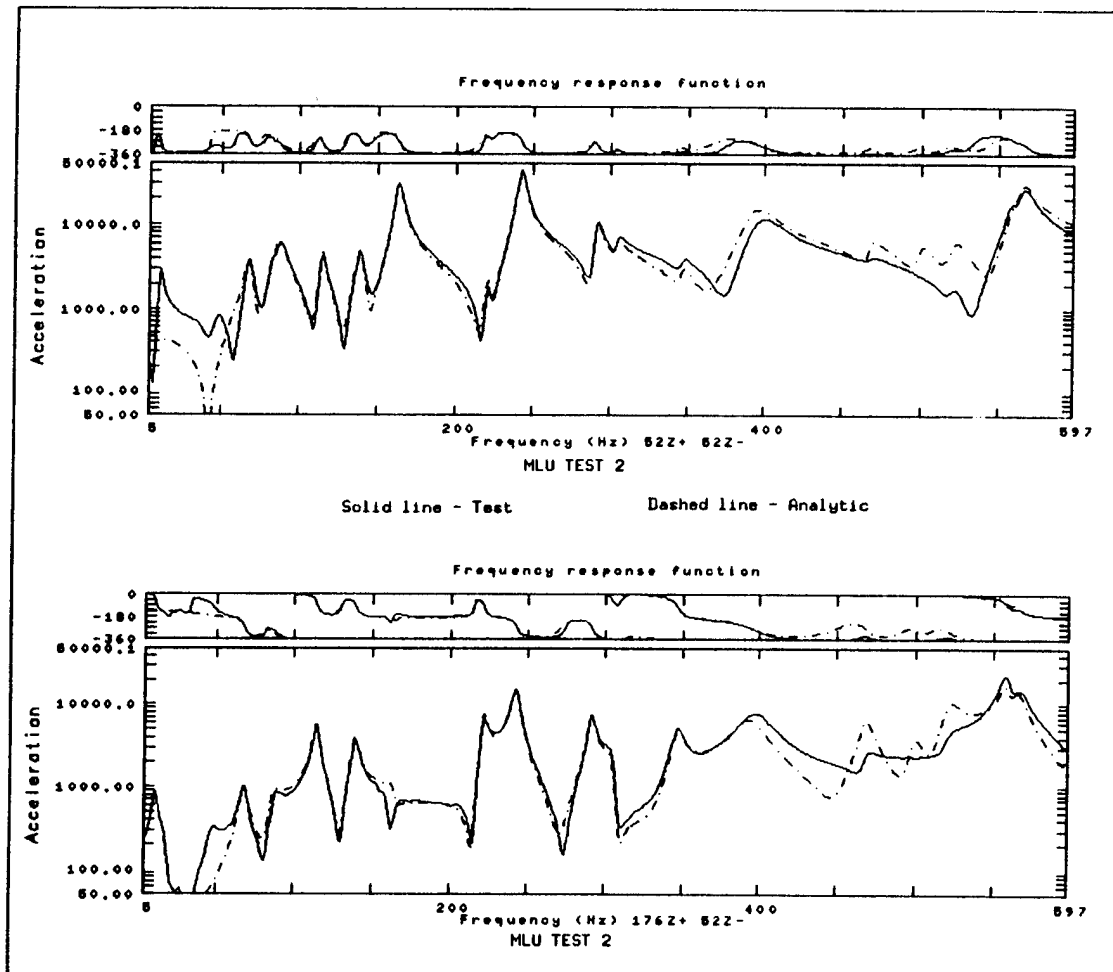
Figure 18. MLU Analytic FRF (Dashed) and Measured FRF (Solid), Node 52

HLU and MLU tests are listed in Appendix J. Table 2 shows a comparison of the HLU/MLU frequencies where it is evident that 14 out of 16 MLU frequencies are higher. (The number listed after "HLU" and "MLU" in the table indicates the number of the test run.) This frequency shift is portrayed graphically in Figure 19. The FE model frequencies are also listed in Table 2 for comparison.

A similar comparison for the damping ratios (in percent of critical damping) is shown in Table 3 and Figure 20, where all of the MLU damping ratios are higher. Note also that many of the damping ratios are quite high (greater than one percent), particularly for the second mode. This could be due to insufficient spectral resolution (true maxima not identified), non-proportional damping, or damping introduced by the support conditions.

3. Mode Shape Correlation

A Modal Assurance Criteria (MAC) matrix was calculated in order to correlate the mode shapes. The MAC method uses a least squares technique to correlate two sets of mode shapes, either from two different reference coordinates of the same structure, two different tests, or from a test and a finite element model solution. A MAC value of one indicates a perfect correlation, whereas a MAC value near zero indicates linear independence between mode shapes. When assembled into a matrix, the rows are the modes (or DOF's) for one set of mode shapes and the columns are the modes for the other set of mode shapes. The MAC matrix is typically presented graphically with the rows and columns of the matrix making up the horizontal floor and the MAC value making up the vertical bars. Appendix C has more detailed information on calculating the MAC.

The first correlations were performed between mode shapes calculated from different reference locations on the same plate to check the adequacy of the data and curve fit. Figures 21 and 22 show the MAC matrices for the HLU and MLU plates, respectively, where a high correlation between mode shapes is evident from the MAC values close to 1 along the diagonal. The non-zero values for off-diagonal MAC terms are probably due to some noise in the data. The MAC matrix for the HLU /

MODE	HLU21 FREQ	MLU2 FREQ	DIFFERENCE	% DIFF	FE FREQ
1	64.084	67.955	3.871	6.04	63.12
2	82.878	86.887	4.009	4.84	88.5
3	110.628	114.458	3.83	3.46	112.27
4	133.179	138.645	5.466	4.10	148.74
5	159.559	163.659	4.1	2.57	157.16
6	221.542	221.525	-0.017	0.01	247.84
7	238.048	242.358	4.31	1.81	251.21
8	288.421	291.394	2.973	1.03	300.4
9	306.315	304.421	-1.894	0.62	321.46
10	343.383	346.639	3.256	0.95	347.88
11	390.374	392.949	2.575	0.66	403.1
12	465.919	468.634	2.715	0.58	---
13	494.100	500.195	6.095	1.23	493.75
14	505.978	521.241	15.263	3.02	526.34
15	553.979	558.03	4.051	0.73	551.64
16	562.869	565.273	2.404	0.43	563.87

Table 2. HLU/MLU Frequency Comparison
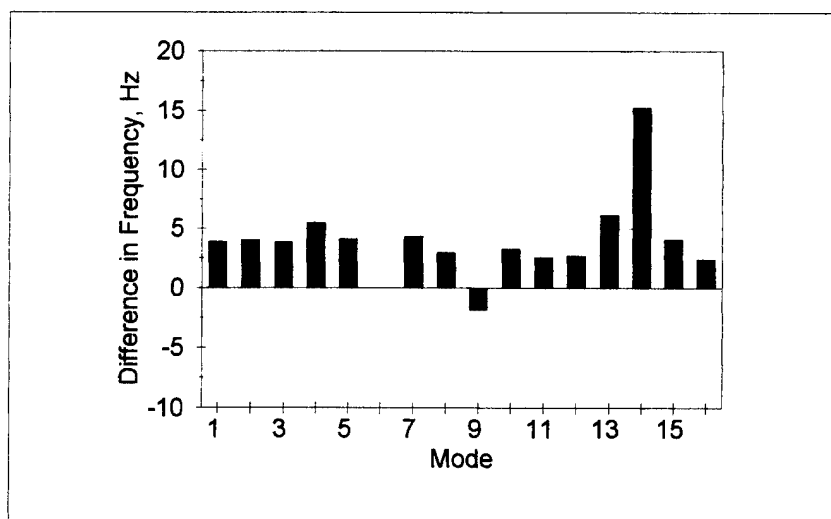
Figure 19. HLU/MLU Frequency Difference Chart

41

MODE	HLU21 DAMPING	MLU2 DAMPING	DIFFERENCE	% DIFF
1	0.908	3.081	2.173	239.317
2	4.054	4.407	0.353	8.707
3	0.852	1.621	0.769	90.258
4	0.514	1.591	1.077	209.533
5	0.215	1.318	1.103	513.023
6	0.587	0.746	0.159	27.087
7	0.189	0.902	0.713	377.249
8	0.412	0.810	0.398	96.602
9	0.399	0.925	0.526	131.830
10	0.227	0.975	0.748	329.515
11	0.781	2.480	1.699	217.542
12	0.579	0.905	0.326	56.304
13	0.776	0.906	0.130	16.753
14	0.510	1.098	0.588	115.294
15	0.299	0.621	0.322	107.692
16	0.436	0.920	0.484	111.009

Table 3. HLU/MLU Damping Ratio Comparison
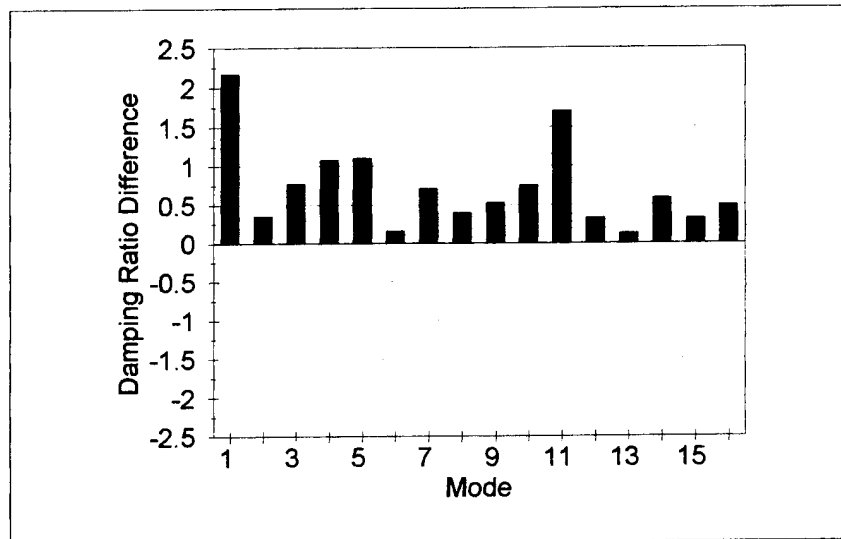
Figure 20. HLU/MLU Damping Ratio Difference Chart
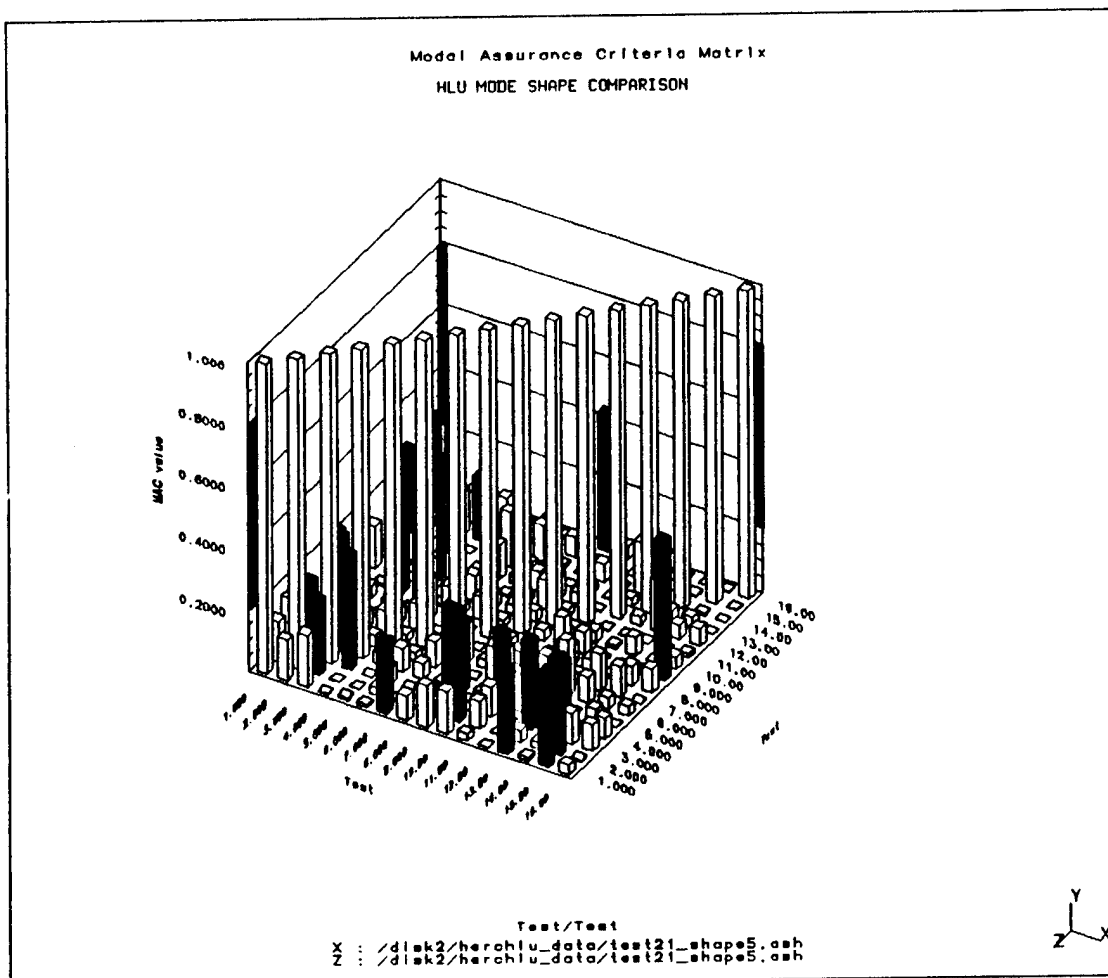
Figure 21. HLU Modal Assurance Criteria Matrix
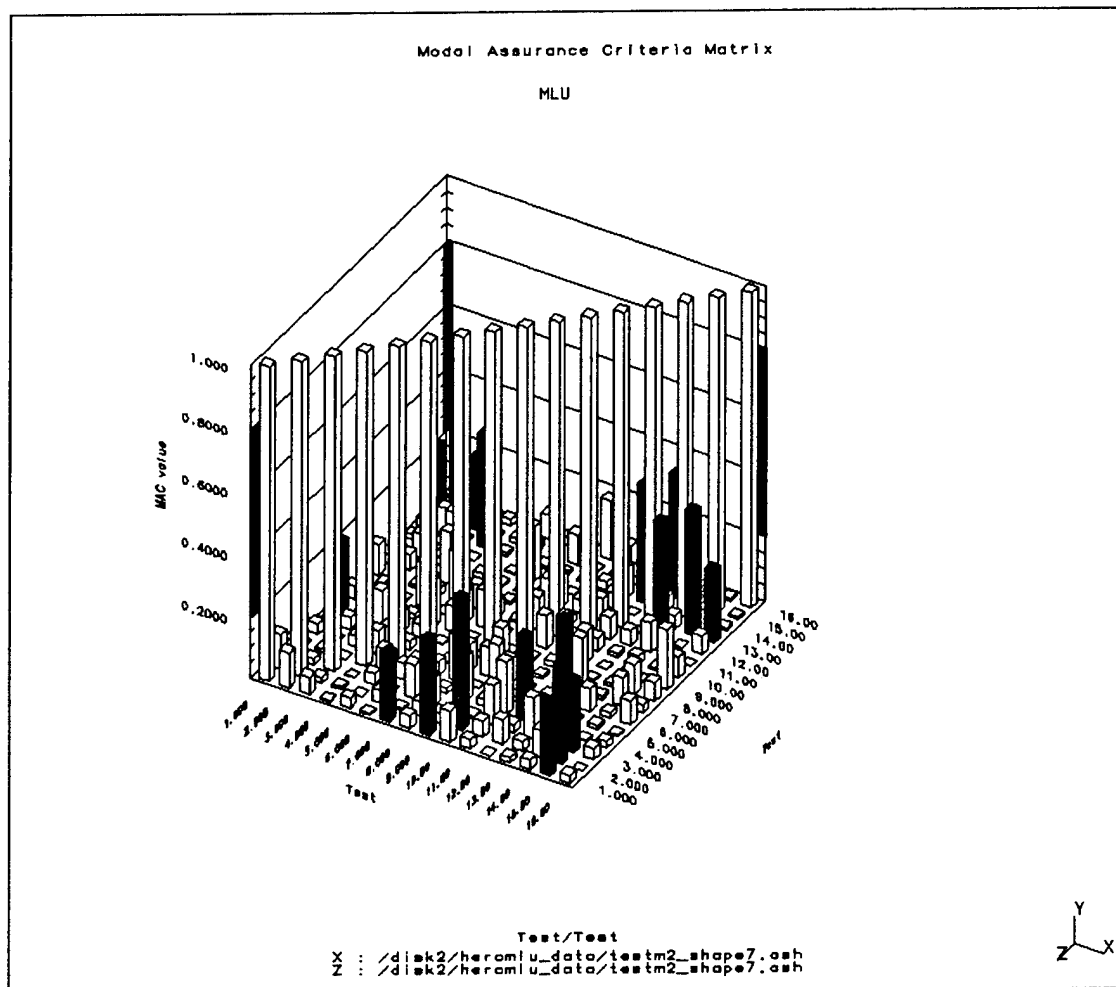
Figure 22. MLU Modal Assurance Criteria Matrix

MLU correlation is shown in Figures 23 and 24 for the real and complex mode shapes, respectively. It is evident from these figures that poor correlation exists for a number of modes, as seen by the low MAC values along the diagonal. Appendix J lists the diagonal MAC values for the complex shapes.

As an additional comparison between the mode shapes of the plates, the IDEAS Post Processing feature was utilized to graphically portray the physical deflections of the two plates. Figures 25 through 30 show a comparison between the two plates and the FE model at modes 1, 13 and 16, where a qualitative 3-D view is shown first and a side view for a more quantitative assessment is shown second. (Note that only the nodes coincident with an accelerometer position are shown as deflected for the experimental data.) At the first mode (Figures 25 and 26), a good correlation exists (MAC = .98) and the deflections closely agree. For mode 13 (Figures 27 and 28, MAC=.723), a significant difference can be seen in the deflections at the upper left and lower right portions of the plates (MAC=.056). Finally, Figures 29 and 30 show similar results for mode 16, where differences are seen in the upper right and left corners of the plates.

Before drawing any conclusions about the meaning of the apparent difference in mode shapes, it should be noted that there are several possible explanations for the poor correlation [Ref 7, p. 677]:

1. The tested system is nonstationary due to changes in mass, stiffness, or damping properties during the test.
2. The system is non-linear.
3. The reference mode shape contains noise.
4. The method used for parameter extraction is invalid for the measured data.
5. The mode shapes are linearly independent.

If the first four of these reasons can be eliminated, the differences in mode shapes can be considered to represent a real difference in the dynamic behavior of the two plates. The first possibility can be discarded by observing that the test environment (temperature, pressure suspension method, etc.) did not change appreciably between

45
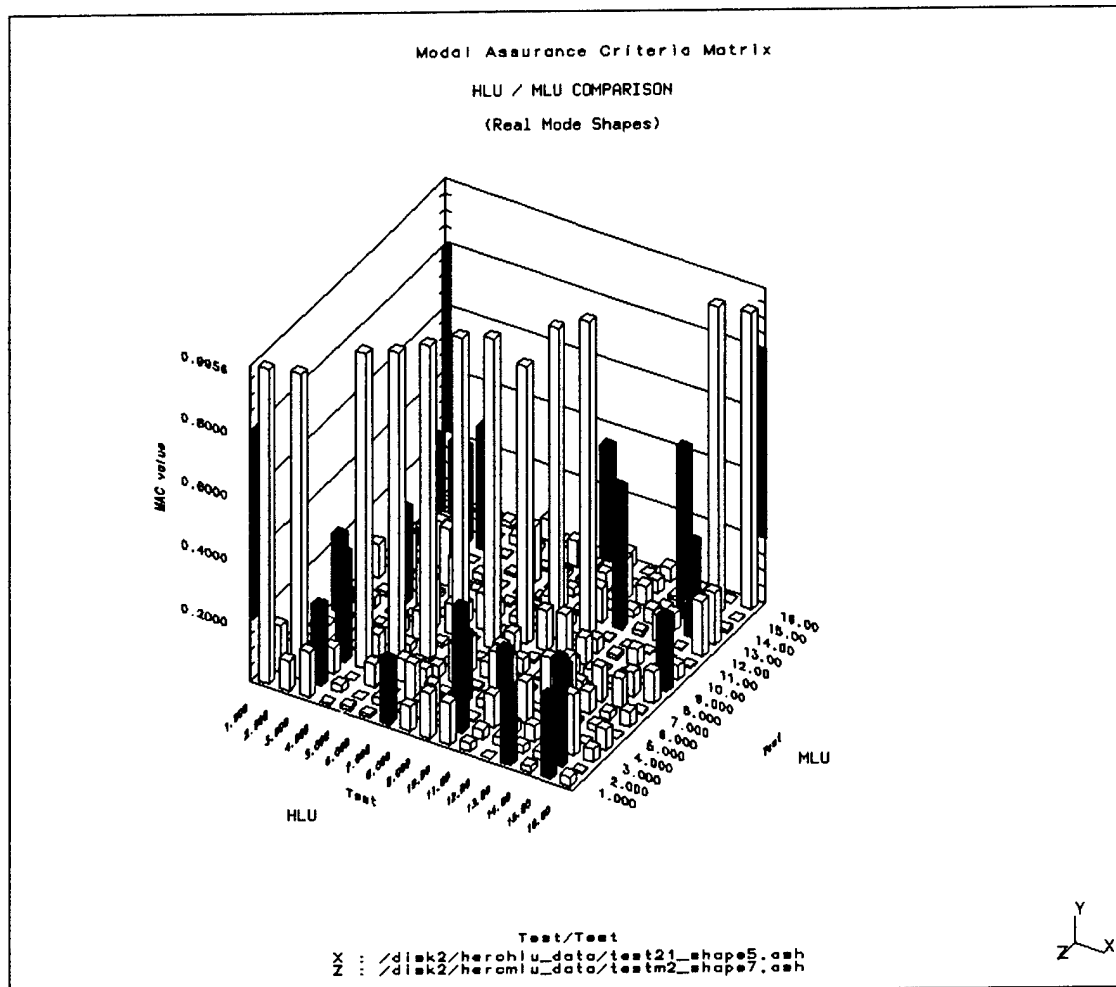
Figure 23. HLU/MLU Modal Assurance Criteria Matrix, Real Modes
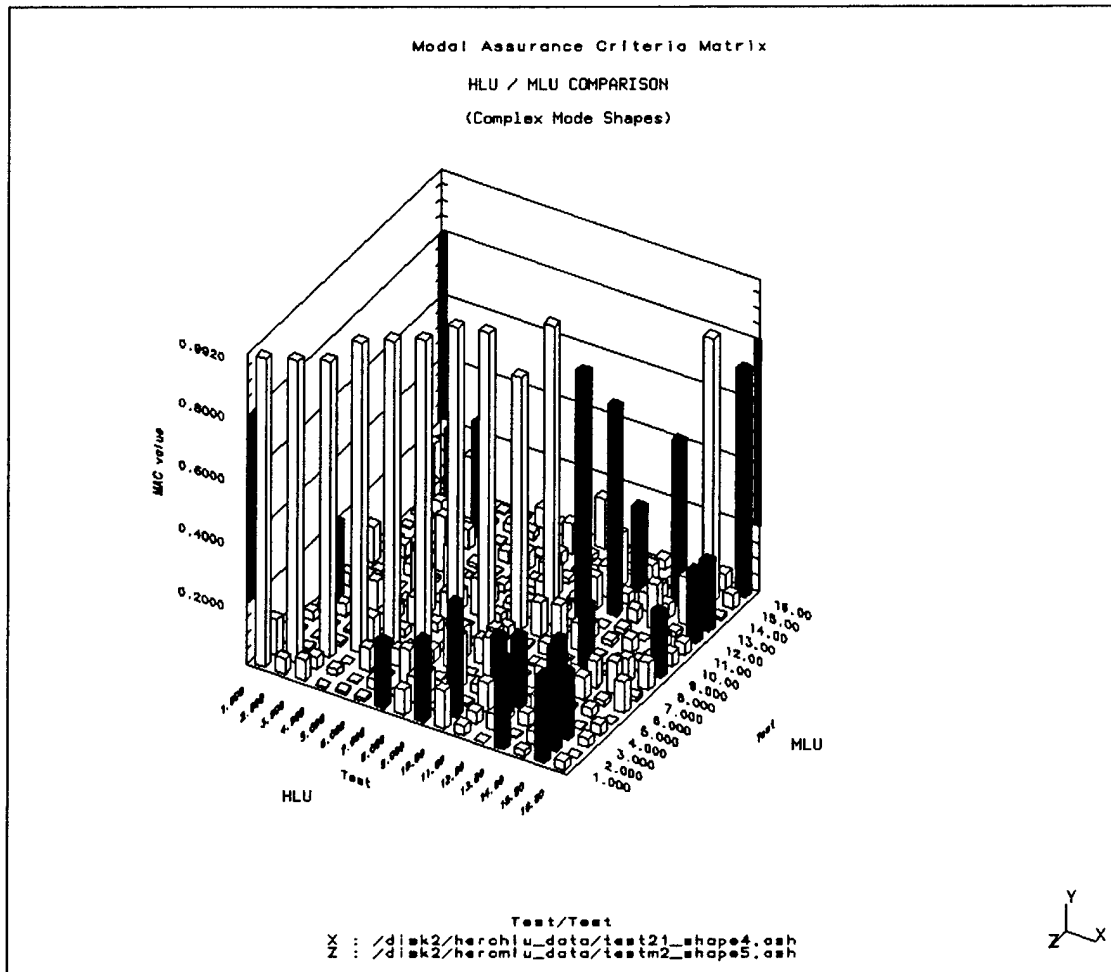
Figure 24. HLU/MLU Modal Assurance Criteria Matrix, Complex Modes
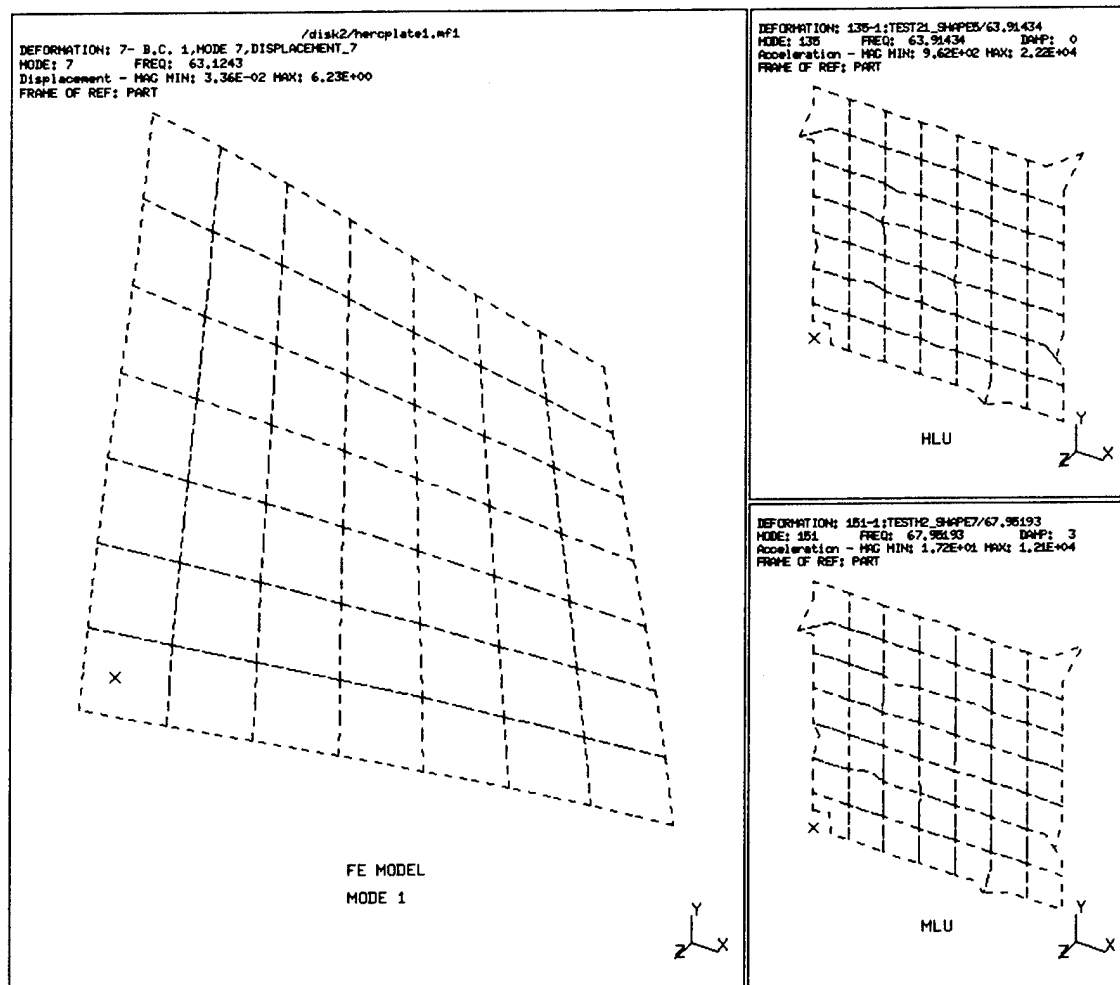
Figure 25. Mode Shape Comparison, Qualitative View, Mode 1

Figure 26. Mode Shape Comparison, Side View, Mode 1

49

/disk2/heroplate1.mf1
DEFORMATION: 18- B.C. 1,MODE 18,DISPLACEMENT_18
MODE: 18   FREQ: 493.362
Displacement - MAG MIN: 1.39E-02 MAX: 2.52E+00
FRAME OF REF: PART

FE MODEL
MODE 13

DEFORMATION: 147-13:TEST21_SHAPE5/494.0847
MODE: 147   FREQ: 494.0847   DAMP: 0
Acceleration - MAG MIN: 5.81E+02 MAX: 1.25E+04
FRAME OF REF: PART

HLU

DEFORMATION: 131-13:TESTM2_SHAPE7/500.1141
MODE: 131   FREQ: 500.1141   DAMP: 0
Acceleration - MAG MIN: 7.72E+02 MAX: 4.63E+03
FRAME OF REF: PART

MLU

Figure 27. Mode Shape Comparison, Qualitative View, Mode 13

50
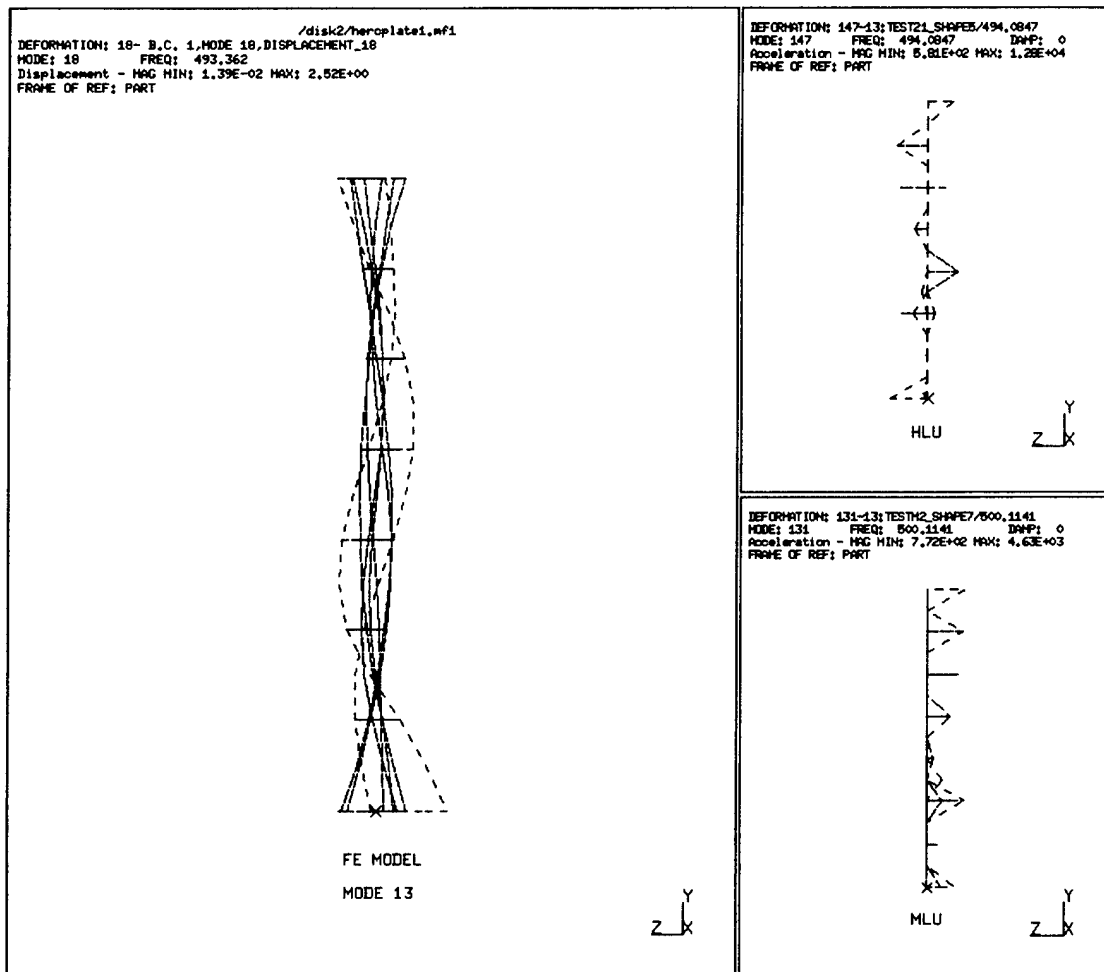
Figure 28. Mode Shape Comparison, Side View, Mode 13
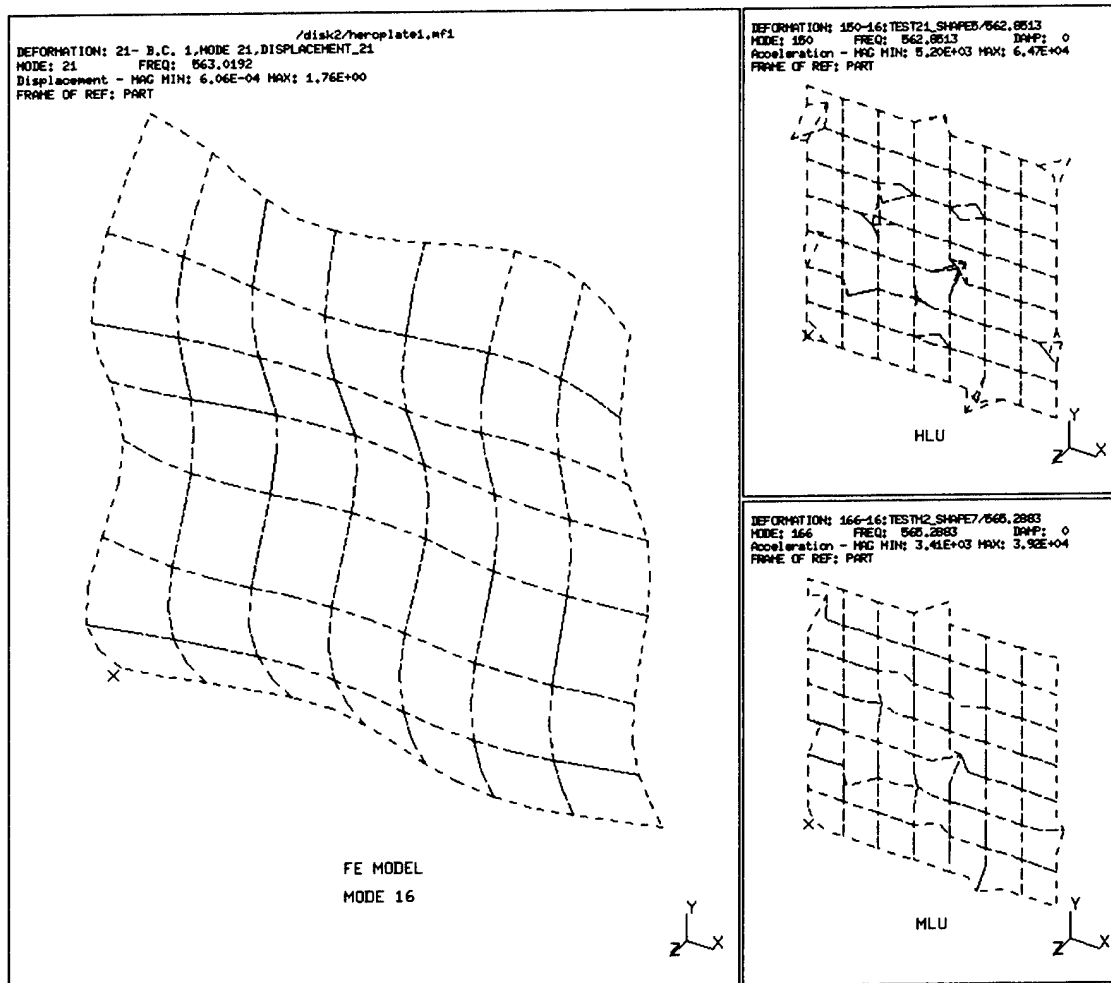
Figure 29. Mode Shape Comparison, Qualitative View, Mode 16
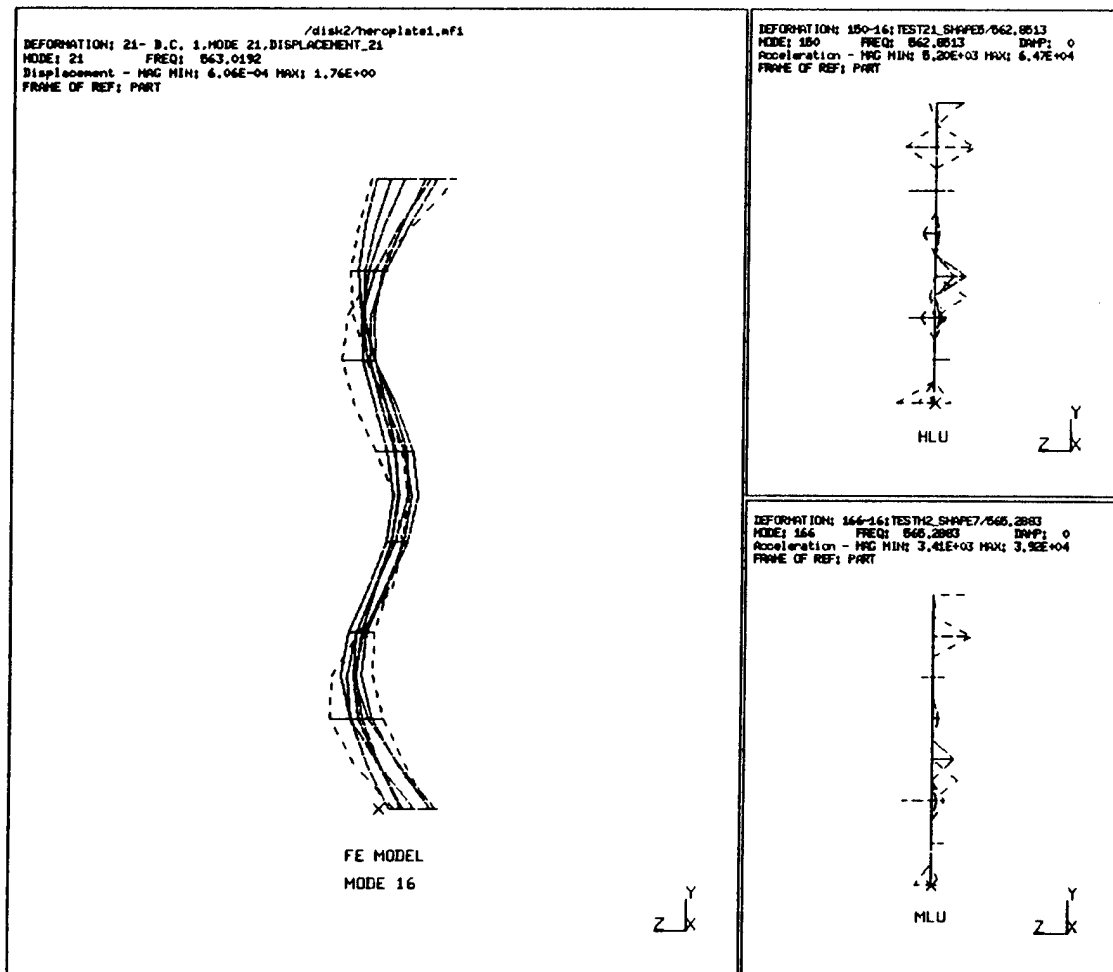
Figure 30. Mode Shape Comparison, Side View, Mode 16

tests so that no changes in material properties would have occured. Secondly, the forces applied to the structure were not high enough to cause non-linear behavior in the test specimens. Examination of the FRF's does not indicate an inordinate amount of noise and the fact that the tests were reproducible supports this observation. Concerning the fourth reason above, the natural frequencies derived by the polyreference technique correlate fairly well with the Finite Element solution, as shown earlier in Table 2, substantiating the extraction results.

4. Error Estimation

The minimum frequency error is defined by the spectral resolution, which in the case of these measurements was 1.25 Hz. To better assess the true error and the degree of reproducibility, modal parameters were extracted from several different MLU test runs and compared against the HLU parameters obtained previously. Tables 4 and 5 and Figures 30 and 31 show the frequency comparisons which indicate a similar shift to that observed in Figure 19, though it is somewhat less pronounced. Tables 6 and 7 and Figures 32 and 33 show a comparison between frequencies derived from different MLU test runs. Figure 32 is a comparison of two consecutive runs conducted one day apart where the transducers remained in place. Figure 33 is a comparison of two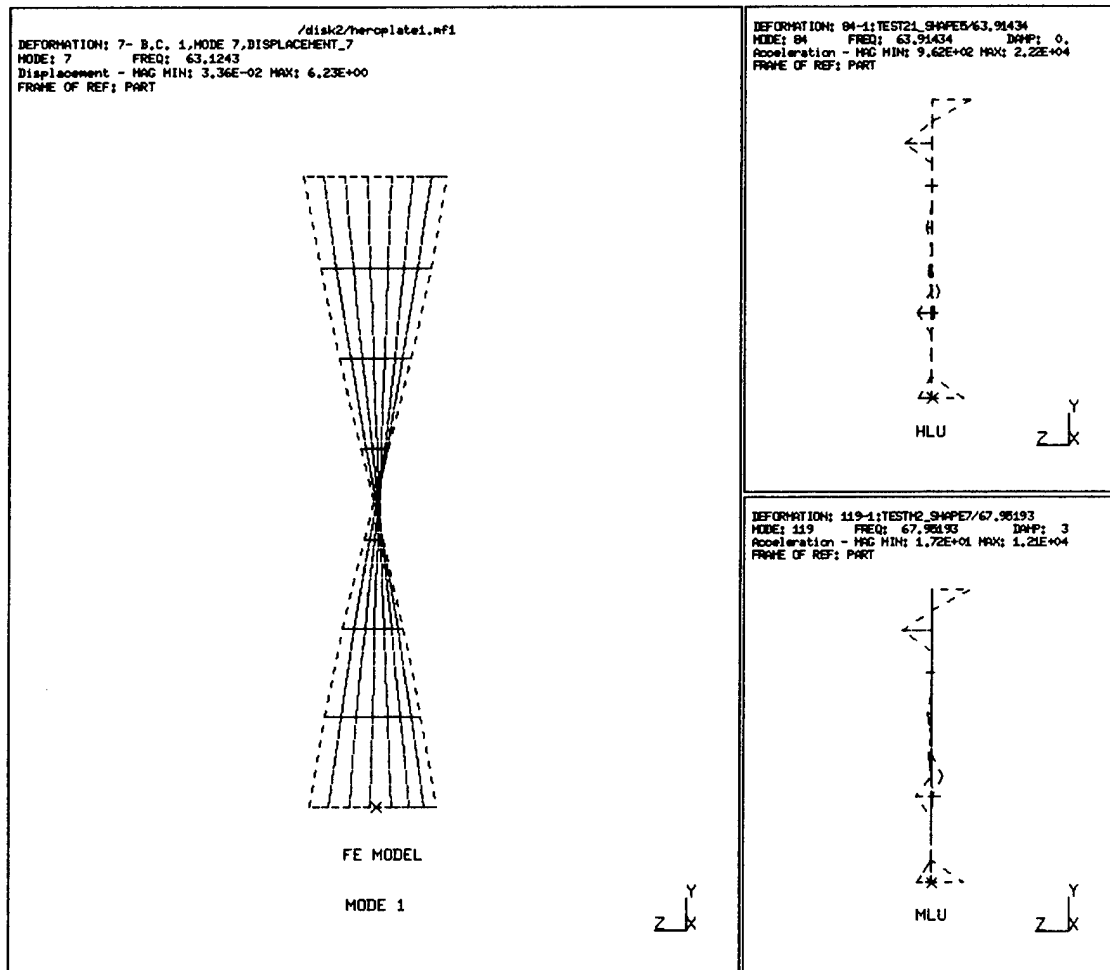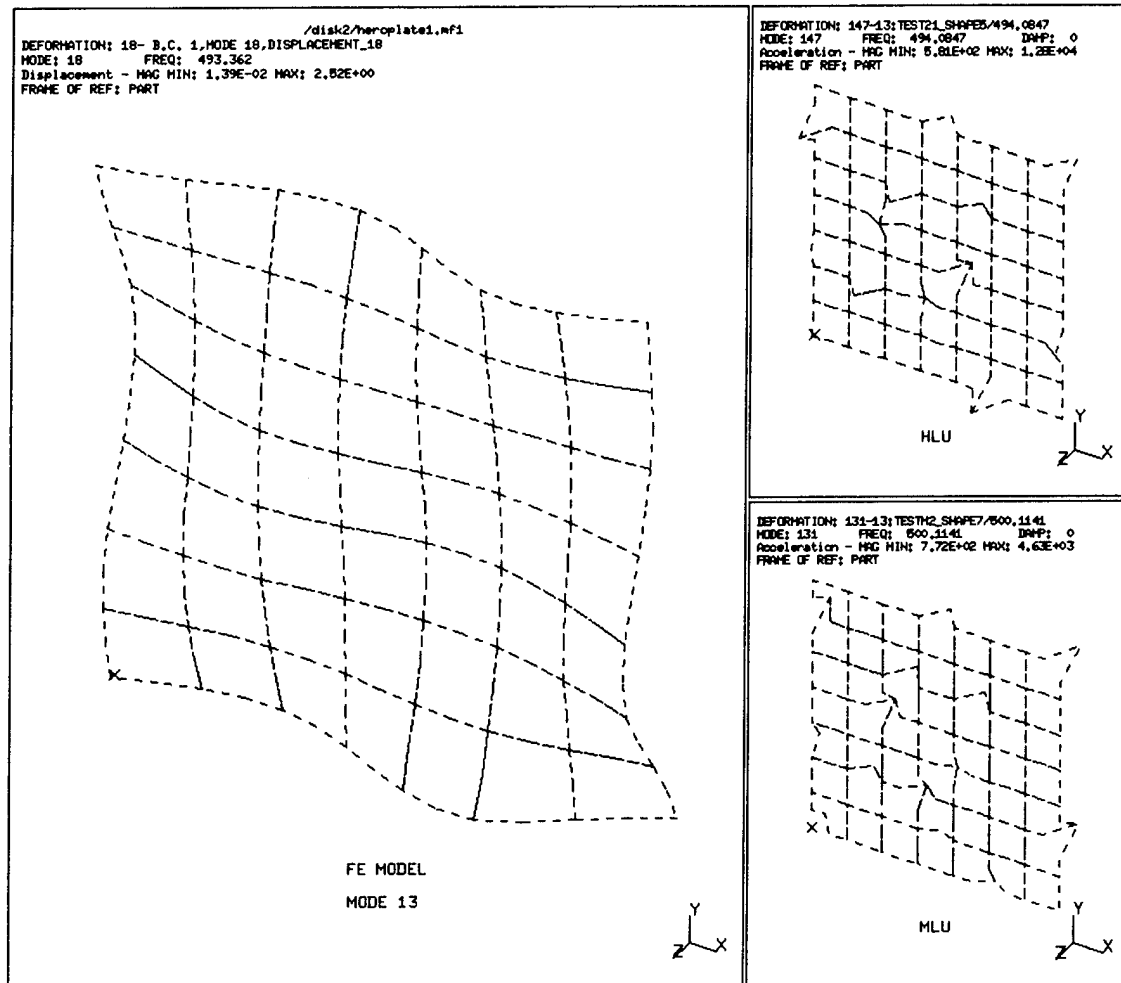 MLU tests (runs 2 and 9) where all of the transducers had been removed and the plate unhooked from the support frame between runs. The reduction in reproducibility when the transducers are removed and replaced is obvious from these figures.

A similar comparison of the extracted damping ratios was carried out and is illustrated in Tables 8 through 11 and Figures 35 through 38. The bias towards higher damping ratios for the MLU seen in Figure 20 is evident in Figures 35 and 36; however, the comparison between MLU tests in Figures 37 and 38 shows that significant variation in damping ratios exists between test runs on the same plate. The fact that a noticeable bias exists between MLU test runs 2 and 9 (Figure 38), where transducers were removed and replaced, and not for test runs 8 and 9 (Figure 37), where transducers remained in place, indicates that the damping bias may have

54

MODE	HLU21 FREQ	MLU8 FREQ	DIFFERENCE	% DIFF
1	64.084	66.080	1.996	3.11
2	82.878	82.250	-0.628	0.76
3	110.628	112.008	1.38	1.25
4	133.179	138.099	4.92	3.69
5	159.559	161.354	1.795	1.12
6	221.542	222.916	1.374	0.62
7	238.048	243.240	5.192	2.18
8	288.421	291.783	3.362	1.17
9	306.315	304.379	-1.936	0.63
10	343.383	349.264	5.881	1.71
11	390.374	396.721	6.347	1.63
12	465.919	469.701	3.782	0.81
13	494.100	502.884	8.784	1.78
14	505.978	520.150	14.172	2.80
15	553.979	561.094	7.115	1.28
16	562.869	567.520	4.651	0.83

Table 4. HLU Run 21/MLU Run 8 Frequency Comparison
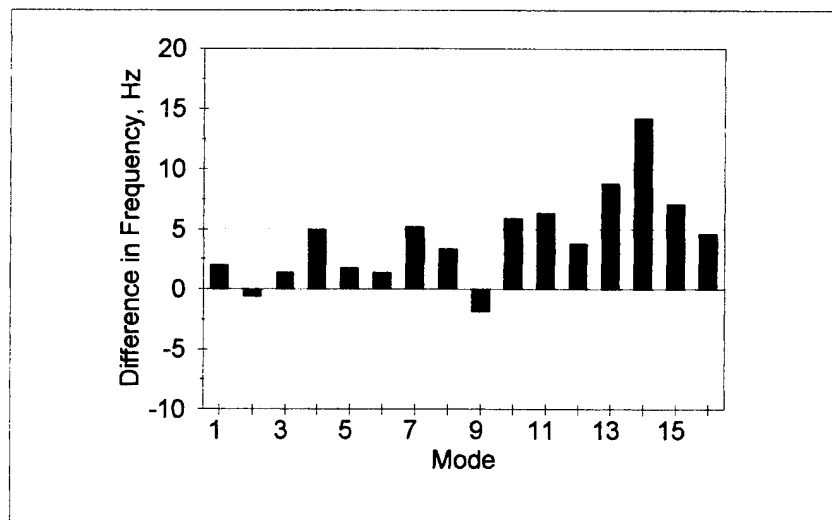
Figure 31. HLU Run 21/MLU Run 8 Frequency Difference Chart

MODE	HLU21 FREQ	MLU9 FREQ	DIFFERENCE	% DIFF
1	64.084	66.127	2.043	3.19
2	82.878	85.742	2.864	3.46
3	110.628	112.608	1.98	1.79
4	133.179	140.719	7.54	5.66
5	159.559	160.617	1.058	0.66
6	221.542	223.014	1.472	0.66
7	238.048	243.535	5.487	2.30
8	288.421	291.771	3.35	1.16
9	306.315	304.634	-1.681	0.55
10	343.383	349.821	6.438	1.87
11	390.374	398.932	8.558	2.19
12	465.919	468.320	2.401	0.52
13	494.100	503.548	9.448	1.91
14	505.978	522.286	16.308	3.22
15	553.979	560.423	6.444	1.16
16	562.869	567.995	5.126	0.91

Table 5. HLU Run 21/MLU Run 9 Frequency Comparison
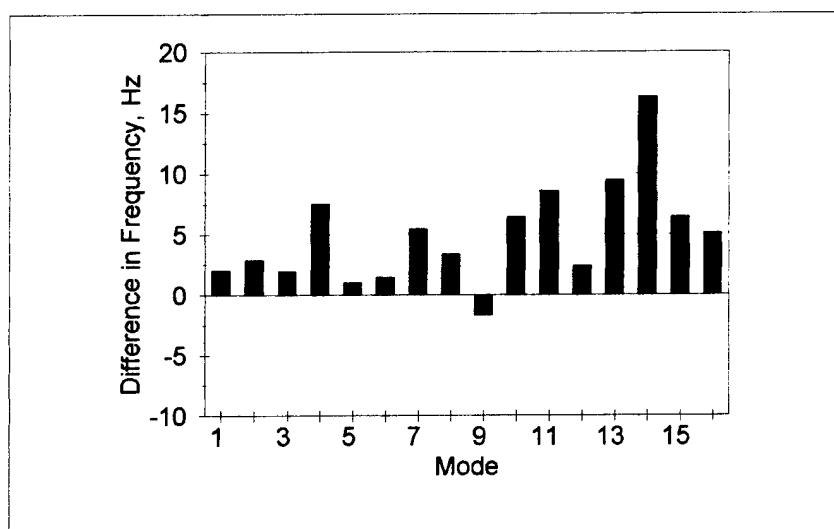
Figure 32. HLU Run 21/MLU Run 9 Frequency Difference Chart

MODE	MLU9 FREQ	MLU8 FREQ	DIFFERENCE	% DIFF
1	66.127	66.080	-0.047	0.07
2	85.742	82.250	-3.492	4.07
3	112.608	112.008	-0.6	0.53
4	140.719	138.099	-2.62	1.86
5	160.617	161.354	0.737	0.46
6	223.014	222.916	-0.098	0.04
7	243.535	243.240	-0.295	0.12
8	291.771	291.783	0.012	0.00
9	304.634	304.379	-0.255	0.08
10	349.821	349.264	-0.557	0.16
11	398.932	396.721	-2.211	0.55
12	468.320	469.701	1.381	0.29
13	503.548	502.884	-0.664	0.13
14	522.286	520.150	-2.136	0.41
15	560.423	561.094	0.671	0.12
16	567.995	567.520	-0.475	0.08

Table 6. MLU Runs 8 and 9 Frequency Comparison (Reproducibility)
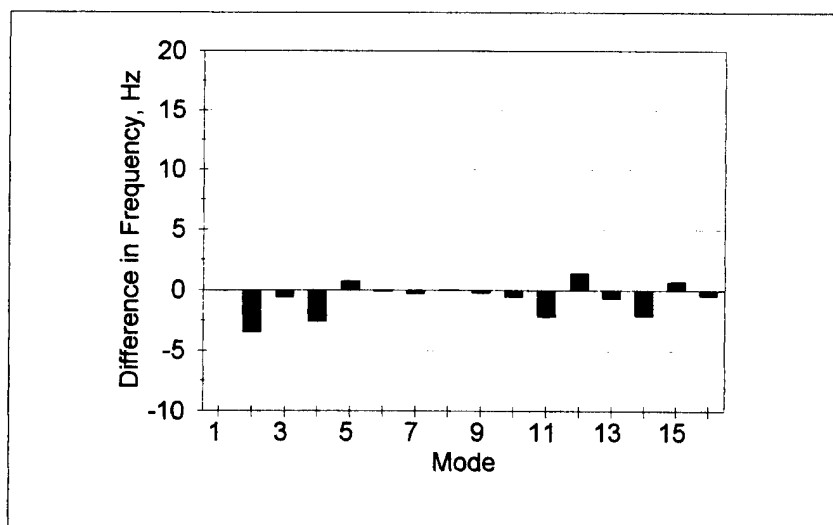
Figure 33. MLU Runs 8 and 9 Frequency Difference Chart (Reproducibility)

57

MODE	MLU9 FREQ	MLU2 FREQ	DIFFERENCE	% DIFF
1	66.127	67.955	1.828	2.76
2	85.742	86.887	1.145	1.34
3	112.608	114.458	1.85	1.64
4	140.719	138.645	-2.074	1.47
5	160.617	163.659	3.042	1.89
6	223.014	221.525	-1.489	0.67
7	243.535	242.358	-1.177	0.48
8	291.771	291.394	-0.377	0.13
9	304.634	304.421	-0.213	0.07
10	349.821	346.639	-3.182	0.91
11	398.932	392.949	-5.983	1.50
12	468.320	468.634	0.314	0.07
13	503.548	500.195	-3.353	0.67
14	522.286	521.241	-1.045	0.20
15	560.423	558.03	-2.393	0.43
16	567.995	565.273	-2.722	0.48

Table 7. MLU Runs 2 and 9 Frequency Comparison (Reproducibility)
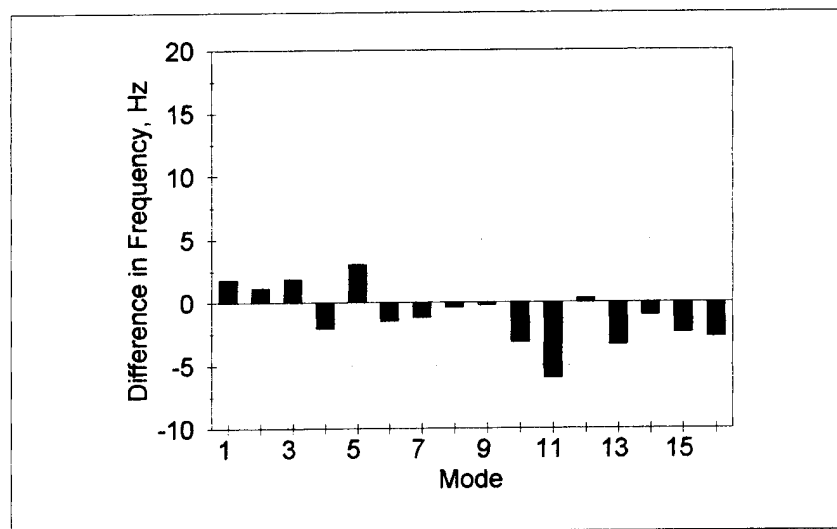
Figure 34. MLU Runs 2 and 9 Frequency Difference Chart (Reproducibility)

MODE	HLU21 DAMPING	MLU8 DAMPING	DIFFERENCE	% DIFF
1	0.908	3.737	2.829	311.564
2	4.054	3.400	-0.654	16.132
3	0.852	1.064	0.212	24.883
4	0.514	1.138	0.624	121.401
5	0.215	0.949	0.734	341.395
6	0.587	0.414	-0.173	29.472
7	0.189	0.629	0.440	232.804
8	0.412	0.469	0.057	13.835
9	0.399	0.597	0.198	49.624
10	0.227	0.635	0.408	179.736
11	0.781	2.234	1.453	186.044
12	0.579	0.519	-0.060	10.363
13	0.776	0.682	-0.094	12.113
14	0.510	0.901	0.391	76.667
15	0.299	0.576	0.277	92.642
16	0.436	0.762	0.326	74.771

Table 8. HLU Run 21/MLU Run 8 Damping Ratio Comparison
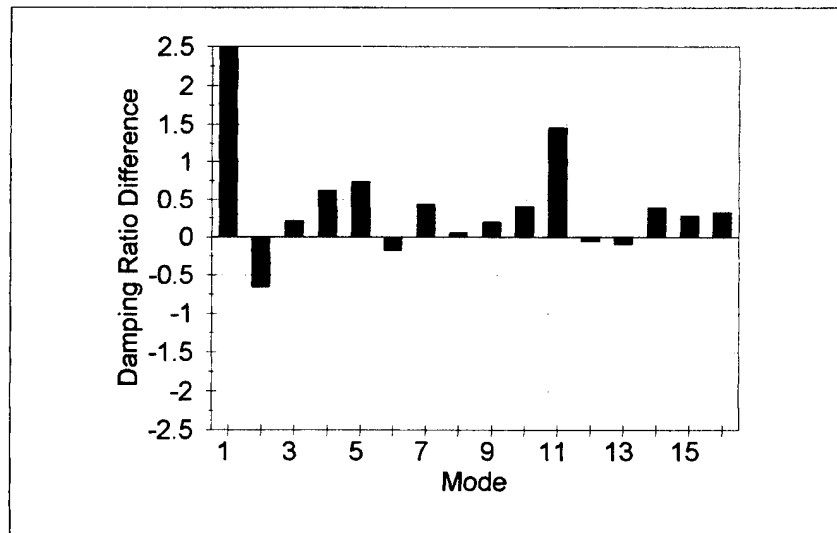
Figure 35. HLU Run 21/MLU Run 8 Damping Ratio Difference Chart

MODE	HLU21 DAMPING	MLU9 DAMPING	DIFFERENCE	% DIFF
1	0.908	2.495	1.587	174.780
2	4.054	2.489	-1.565	38.604
3	0.852	1.074	0.222	26.056
4	0.514	0.972	0.458	89.105
5	0.215	0.835	0.620	288.372
6	0.587	0.618	0.031	5.281
7	0.189	0.674	0.485	256.614
8	0.412	0.697	0.285	69.175
9	0.399	0.770	0.371	92.982
10	0.227	1.129	0.902	397.357
11	0.781	1.354	0.573	73.367
12	0.579	0.623	0.044	7.599
13	0.776	0.694	-0.082	10.567
14	0.510	0.959	0.449	88.039
15	0.299	0.669	0.370	123.746
16	0.436	0.767	0.331	75.917

Table 9. HLU Run 21/MLU Run 9 Damping Ratio Comparison
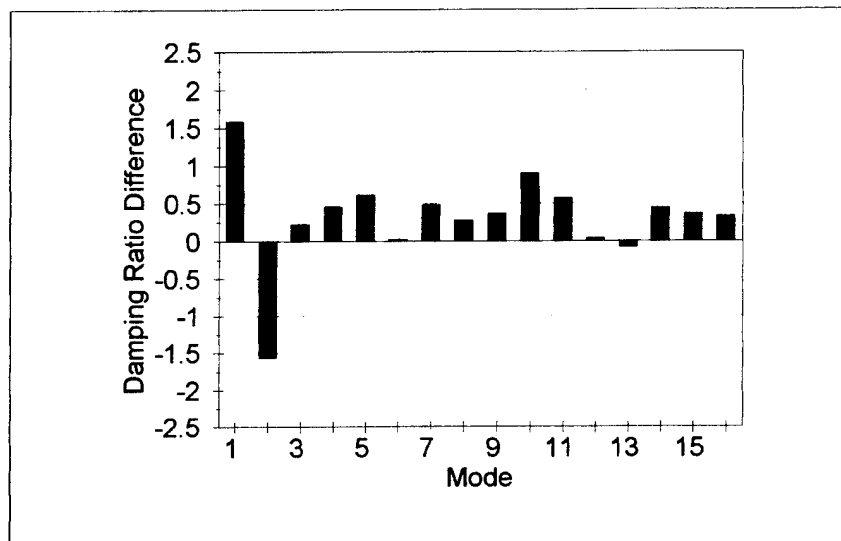
Figure 36. HLU Run 21/MLU Run 9 Damping Ratio Difference Chart

MODE	MLU8 DAMPING	MLU9 DAMPING	DIFFERENCE	% DIFF
1	3.737	2.495	-1.242	33.235
2	3.400	2.489	-0.911	26.794
3	1.064	1.074	0.010	0.940
4	1.138	0.972	-0.166	14.587
5	0.949	0.835	-0.114	12.013
6	0.414	0.618	0.204	49.275
7	0.629	0.674	0.045	7.154
8	0.469	0.697	0.228	48.614
9	0.597	0.770	0.173	28.978
10	0.635	1.129	0.494	77.795
11	2.234	1.354	-0.880	39.391
12	0.519	0.623	0.104	20.039
13	0.682	0.694	0.012	1.760
14	0.901	0.959	0.058	6.437
15	0.576	0.669	0.093	16.146
16	0.762	0.767	0.005	0.656

Table 10. MLU Runs 8 & 9 Damping Ratio Comparison (Reproducibility)
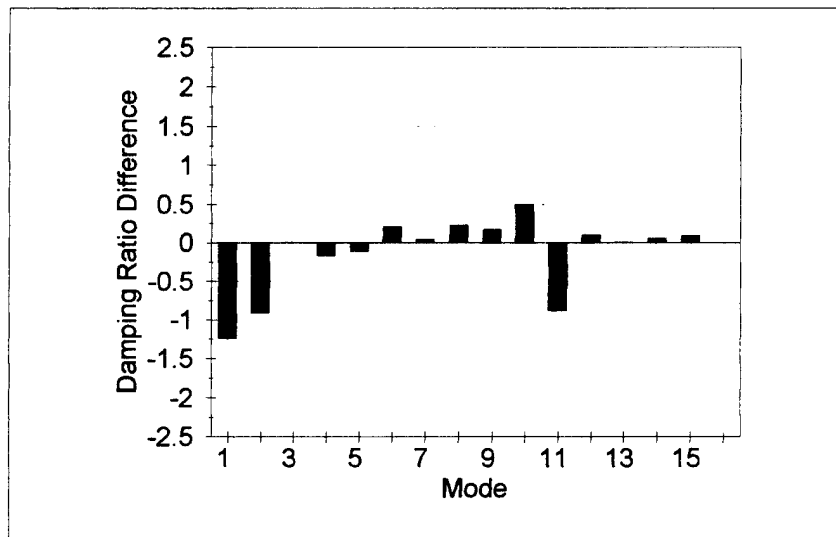
Figure 37. MLU Runs 8 & 9 Damping Ratio Difference Chart (Reproducibility)

61

MODE	MLU9 DAMPING	MLU2 DAMPING	DIFFERENCE	% DIFF
1	2.495	3.081	0.586	23.487
2	2.489	4.407	1.918	77.059
3	1.074	1.621	0.547	50.931
4	0.972	1.591	0.619	63.683
5	0.835	1.318	0.483	57.844
6	0.618	0.746	0.128	20.712
7	0.674	0.902	0.228	33.828
8	0.697	0.810	0.113	16.212
9	0.770	0.925	0.155	20.130
10	1.129	0.975	-0.154	13.640
11	1.354	2.480	1.126	83.161
12	0.623	0.905	0.282	45.265
13	0.694	0.906	0.212	30.548
14	0.959	1.098	0.139	14.494
15	0.669	0.621	-0.048	7.175
16	0.767	0.920	0.153	19.948

Table 11. MLU Runs 2 & 9 Damping Ratio Comparison (Reproducibility)
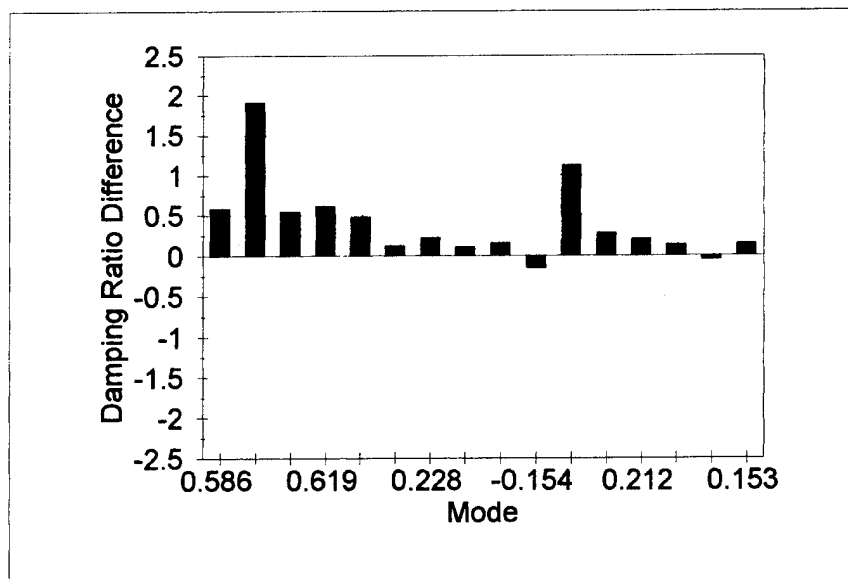
Figure 38. MLU Runs 2 & 9 Damping Ratio Difference Chart (Reproducibility)

more to do with transducer locations and support conditions than with any inherent difference between plates.

5. Summary of Results

Even after accounting for the reproducibility errors, a measurable difference in frequencies and mode shapes is evident between the two plates. Because of the variability in damping ratio measurements, the damping ratio comparison is not conclusive. If the frequency and mode shape results are assumed to be a valid representation of the dynamic behavior of the two plates, it is clear that differences in that behavior not only exist but are quantifiable by reference to either the MAC value or the frequency shift. These differences in dynamic behavior can only be attributed to underlying differences in the stiffness, inertial, and damping properties of the plates. In this regard it would appear that the MLU is either "stiffer", less dense, more heavily damped, or some combination of the three. (Since the two plates differ in mass by less than one gram, the inertial differences would have to be due to mass distribution.) The cause of these differences could be anything from less variation in fiber volume or fewer voids in the MLU plate to differences in cure rate between the two plates. In any event, the significance for this investigation is the fact that the differences are identifiable.

V. CONCLUSIONS AND RECOMMENDATIONS

A. CONCLUSIONS

The experimental modal measurement and finite element dynamic analysis techniques employed in this investigation have been verified against known analytical results for homogeneous isotropic plates. The results of this investigation are relevant to the following Non-Destructive Inspection applications.

1. Quality Assurance and Acceptance Testing

The application of multi-input multi-output modal measurement and discrimination as a Non-Destructive Inspection technique for composite materials quality assurance applications has been demonstrated on two identically configured composite plates manufactured by different processes, one with the traditional hand layup method and one with machine controlled fiber placement. The measurement technique has been shown to have both the reproducibility and resolution to quantitatively discern the differences in dynamic responses of the two samples. This quantitative measured difference is consistent with the qualitative observations that the F-18E/F inlet ducts manufactured by machine aided fiber placement are acoustically quieter and thus presumably more heavily damped.

2. Cost-Effective Composites

Additional investigation into associating micro-mechanical variations with stiffness and damping properties will lead to refined quantification of the link between internal structural differences and global dynamics characteristics. Such methodology may enable utilization of modal measurement for defining the required level of control for materials and processing in composite manufacturing. For instance, dynamic response characteristics derived through modal testing could be used as a quantitative assessment of the effects of increasing the fiber volume variability on stiffness properties. The level of quality control could then be set such that the desired stiffness properties were achieved. Such an approach would be useful in the

manufacture of cost-effective composites for such non-man-safe applications as missiles and torpedoes.

3. Reliability Assurance and Damage Assessment

The demonstrated reproducibility with removal and remounting of transducers opens the possibility of using periodic modal measurements (in comparison to a benchmark measurement taken when new) to monitor in-service structural degradation. This "before and after" evaluation could be applied in both fatigue life monitoring and damage assessment situations provided adequate standardization of apparatus and procedure could be achieved. Effective damage assessment would require localization of structural deficiencies either through a frequency domain technique such as that attempted by Campbell [Ref. 4], or by a comparison of mode shapes for each response coordinate. Mode shapes derived for each measured spacial location could be compared to those from the established benchmark to determine the coordinates causing the discrepancies in modal parameters.

4. Field Applications

The feasibility of adapting modal analysis techniques for fleet use is an open question that can only be resolved with further refinement of both apparatus and procedure. Fleet-wide use of this technique for NDI would require standardization of transducer and shaker mounting locations, component mounting conditions, and the development of benchmark signatures for each individual component to be evaluated. With the compact data storage capabilities now available, compiling a data bank of benchmark modal parameters for critical structural components would not appear problematic. Given that these requirements can be achieved, NDI through modal analysis is a potentially viable technique worthy of future investigation.

B. RECOMMENDATIONS

The following areas of investigation are recommended for future studies of NDI using modal analysis.

1. Conduct damage localization tests using before and after measurements of test specimens with inflicted damage. Utilize a coordinate mode shape comparison in an attempt to localize the damage.

2. Test composite specimens of various geometries to verify applicability to different component configurations.

3. Use alternate specimen support conditions to reduce the variability between measurements. (A clamped configuration may be easier to apply in the field.)

4. Mount the transducers in a more permanent manner to further reduce the variability between measurements.

5. Refine the error estimation through an analysis of the distribution of modal frequencies and damping ratios over a larger number of tests. Build a probability distribution to define the mean and variance of the frequencies and damping ratios for each specimen. The means could then be used as more accurate baselines for comparison.

APPENDIX A. MULTIPLE DOF VIBRATIONS

Consider the forced 2 DOF system modeled by the dual mass-spring-damper arrangement depicted in Figure A.1. The equations of motion may be written as follows:

$$m_1 x_1'' + c_1 x_1' + c_2 (x_1' - x_2') + k_1 x_1 + k_2 (x_1 - x_2) = f_1 (t) \quad \text{A.1}$$

$$m_2 x_2'' - c_2 (x_1' - x_2') - k_2 (x_1 - x_2) = f_2 (t) \quad \text{A.2}$$

Rearranging,

$$m_1 x_1'' + (c_1 + c_2) x_1' - c_2 x_2' + (k_1 + k_2) x_1 - k_2 x_2 = f_1 (t) \quad \text{A.3}$$

$$m_2 x_2'' - c_2 x_1' + c_2 x_2' - k_2 x_1 + k_2 x_2 = f_2 (t) \quad \text{A.4}$$

Or, in matrix form,

$$\begin{bmatrix} m_1 & 0 \\ 0 & m_2 \end{bmatrix} \begin{Bmatrix} x_1'' \\ x_2'' \end{Bmatrix} + \begin{bmatrix} c_1 + c_2 & -c_2 \\ -c_2 & c_2 \end{bmatrix} \begin{Bmatrix} x_1' \\ x_2' \end{Bmatrix} + \begin{bmatrix} k_1 + k_2 & -k_2 \\ -k_2 & k_2 \end{bmatrix} \begin{Bmatrix} x_1 \\ x_2 \end{Bmatrix} = \begin{Bmatrix} f_1 \\ f_2 \end{Bmatrix} \quad \text{A.5}$$

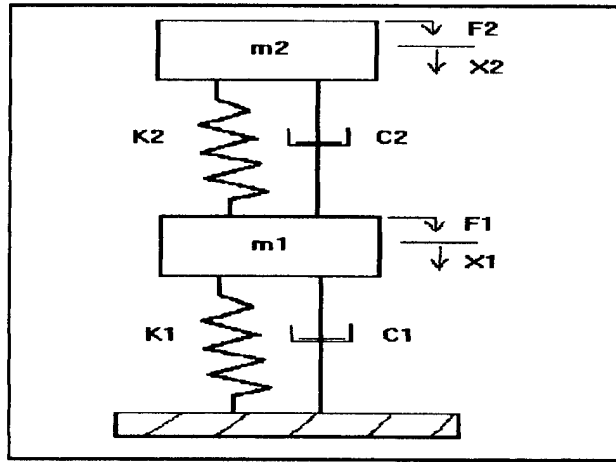$$[m] \{x''\} + [c] \{x'\} + [k] \{x\} = \{f\} \quad \text{A.6}$$

Figure A.1. 2 DOF System

Now consider the case of zero damping and no driving force. We have

$$[m] \{x''\} + [k] \{x\} = [0].$$ A.7

Assuming a solution $x(t) = A\{\psi\} e^{i\omega t}$, where A is a scalar constant and $\{\psi\}$ is a time independent amplitude vector. Substituting into equation A.7 gives

$$([k] - \omega^2 [m]) A\{\psi\} e^{i\omega t} = [0].$$ A.8

A non-trivial solution dictates that

$$\det |[k] - \omega^2 [m]| = 0,$$ A.9

from which the eigenvalues $[\omega_r^2]$ may be obtained. The eigenvectors $\{\psi\}_i$ may then be found by substitution of the eigenvalues back into equation A.8. The $[\omega_r^2]$ and $[\psi]$ matrices represent the natural frequencies and mode shapes of the system, respectively. For the DEF system modeled here, we would have two natural frequencies and two mode shapes corresponding to the two modes of vibration (one for each DOF).

The natural mode shapes thus described have the orthogonality property that

$$\{\psi\}_i^T [m] \{\psi\}_j = 0 \quad i \neq j, \text{ and}$$ A.10

$$\{\psi\}_i^T [k] \{\psi\}_j = 0 \quad i \neq j.$$ A.11

This leads to the condition

$$[\psi]^T [m] [\psi] = [m_r] \text{ and}$$ A.12

$$[\psi]^T [k] [\psi] = [k_r],$$ A.13

so that the natural frequency for each mode r can be expressed in terms of the generalized mass and stiffnesses for that mode, m_r and k_r, as $\omega_r^2 = k_r / m_r$.

The orthogonality property allows us to decouple the differential equations of motion with a coordinate transformation using the mass-normalized mode shapes defined as:

$$[\phi]^T [m] [\phi] = [I],$$ A.14

from which it follows that

$$[\phi]^T [k] [\phi] = [\omega_n^2],$$ A.15

where $[\phi]$ is the mass-normalized mode shape matrix. The normalized mode shape matrix $[\phi]$ is then used as the transformation matrix:

$$\{x\} = [\phi] \{q\},$$ A.16

70

where {q } is the generalized set of coordinates. Substitution into equation A.7 results in the following differential equation of motion:

$$[m] [\phi] \{q''\} + [k] [\phi] \{q\} = [0].$$ A.17

Premultiply by $[\phi]^T$ to obtain

$$[\phi]^T [m][\phi] \{q''\} + [\phi]^T [k][\phi] \{q\} = [0],$$ A.18

or, by equations A.14 and A.15,

$$[I] \{q''\} + [\omega_r^2] \{q\} = [0].$$ A.19

Equation A.19 represents a set of uncoupled differential equations that can be solved for {q} and subsequently transformed back to the { x } domain using equation A.16.

Now adding a forcing function $\{f(t)\} = [F] e^{i\omega t}$ to the right side of equation A.17 and we have

$$[I] \{q°\} + [\omega_r^2] \{q\} = [\phi]^T [F] e^{i\omega t}$$ A.20

Assuming a solution $\{q(t)\} = [Q] e^{i\omega t}$ results in

$$(\omega_r^2 - \omega^2) [Q] e^{i\omega t} = [\phi]^T [F] e^{i\omega t}$$ A.21

$$Q = \frac{[\phi]^T [F]}{(\omega_r^2 - \omega^2)}.$$ A.22

To find the response in the frequency domain, we define the frequency response function, or FRF, as the transfer function between the output (displacement, velocity, or acceleration) to the input (force), as

$$H_{ij}(\omega) = X_i / F_j$$ A.23

where X_i is the response at coordinate i from the excitation F_j at coordinate j. For an N DOF system, H (ω) will be an N x N matrix of FRF elements that constitute the response model. Recalling that $[Q] = [\phi]^{-1} [X]$, equation A.22 gives

$$H_{ij}(\omega) = \frac{X_i}{F_j} = \sum_{r=1}^{N} \frac{\phi_i^r \phi_j^r}{(\omega_r^2 - \omega^2)}$$ A.24

where the summation is made over all DOF's (modes).

71

For proportional damping of the form

$$[c] = \beta [k] + \gamma [m] , \qquad\qquad A.25$$

where β and γ are arbitrary constants, the normal modes of the system will still yield the orthogonality conditions for the damping matrix, that is,

$$\{\psi\}_i^T [c] \{\psi\}_j = 0 \quad i \neq j, \text{ and} \qquad\qquad A.26$$

$$[\psi]^T [c] [\psi] = [c_r]. \qquad\qquad A.27$$

Since $[c_r]$ is also a diagonal matrix, the system of differential equations of motion remains uncoupled and can be solved as an independent set of equations. In this case, the damped mode shapes will be the same as the undamped mode shapes and the damped natural frequencies are

$$\omega_{dr}^2 = \omega_r^2 (1 - \zeta_r^2) \quad \text{where} \quad \zeta_r = \beta \omega_r / 2 + \gamma / 2 \omega_r . \qquad A.28$$

The FRF may be derived in a similar manner to that of the undamped case and is found to be:

$$H_{ij}(\omega) = \sum_{r=1}^{N} \frac{A^r_{ij}}{\omega_r^2 - \omega^2 + i 2 \zeta_r \omega_r \omega} \qquad\qquad A.29$$

where $A^r_{ij} = \phi^r_i \phi^r_j$, the modal constant. An FRF for a typical 2 DOF system is shown in figure A-2, where the two peaks occur at the natural frequencies of the system and correspond to the two modes, one for each DOF. FRF's for most real structures, where the DOF's are infinite, will exhibit a series of successive peaks, some of which are more dominant than others, but each of which correspond to a particular vibrational mode of the structure. The damping at a particular mode is seen as a blunting of the peaks in the FRF. [Ref. 5, 7, 14]

72

FRF
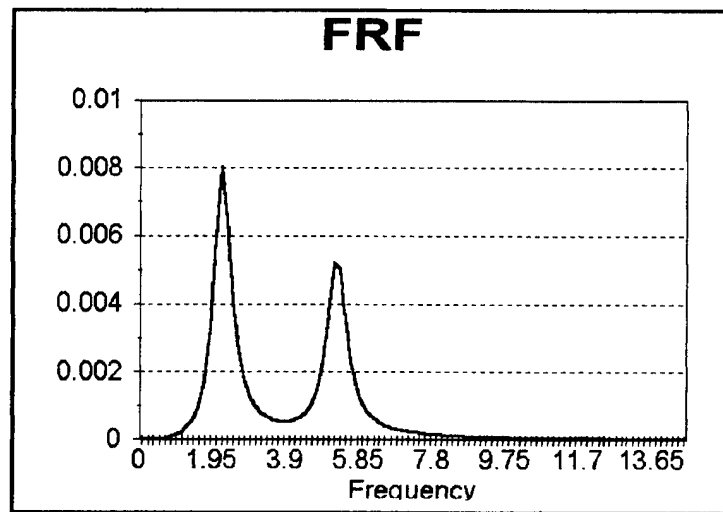
Figure A.2. Frequency Response Function

APPENDIX B. MODAL PARAMETER EXTRACTION

The following describes the process used to extract the modal parameters from the set of measured FRF's.

The first step of the extraction procedure was to initiate a modal parameter table within IDEAS Modal Analysis by determining the resonant modes and an estimate of the frequencies. A Multivariate Mode Indicator Function (MMIF) routine was used to identify the modes and their frequencies. The MMIF minimizes the ratio of the kinetic energies of the in-phase response (real part) to the total response for the entire set of FRF's to identify the normal modes. This idea is based on the fact that at the normal modes, the imaginary of the response reaches a maximum and the real part tends to zero. The Mode Indicator Function (MIF) for a single FRF is characterized by the function:

$$\frac{\sum |H_{re}||H|}{\sum |H|^2} \qquad \text{B.1}$$

where H is the FRF. The MMIF is an extension of this concept, but it finds the force vector that produces the smallest ratio of real response to total response,

$$\frac{F^T A F}{F^T (A+B) F} = a \qquad \text{B.2}$$

where

$F^T A F = F^T (H^T_{re} M H_{re}) F$

$F^T B F = F^T (H^T_{im} M H_{im}) F$

a = a diagonal matrix of the minima.

The minima are found by solving the eigenvalue problem

$$AF = (A + B) F a, \qquad \text{B.3}$$

and the eigenvalues can then be plotted as a function of frequency to reveal the real

75

normal modes. Localized or lower amplitude modes are revealed by the MMIF since the maximum amplitude is normalized to one.

The MMIF has a maximum value of one with downward spikes at the frequencies corresponding to the normal modes. Figure B.1 shows the MMIF for the MLU test FRF's. A "search valleys" function picks the modal frequencies from the MMIF with a user defined threshold for maximum values of the spikes. The end product of this step was a parameter table listing the frequencies of the identified modes for the set of measured FRF's.

The Polyreference complex exponential curve fitting method was then used to estimate the damping ratios and refine the resonant frequency estimates. The Polyreference technique is a time domain algorithm that simultaneously processes multiple FRF's to obtain a global least squares estimate of the modal parameters. The method was developed by Vold et. al. [Ref. 7]. Essentially, it fits decaying exponentials to impulse response functions through an inverse Fourier transform of the FRF's. A summary of the theory behind the technique follows.

The response to a unit impulse at an exciter location can be obtained from the inverse Fourier transform of the appropriate FRF. In matrix form, it is:

$$\{X_i(t_k)\} = [W][U^k]\{A_{ij}\} \qquad \text{B.4}$$

where

$X_i(t_k) = $ an 1 dimensional vector representing the response at i due to a force at j,
   where 1 is the total number of excitation locations

$W = $ an 1 x 2N matrix representing the ratios of the eigenvectors of the different
   exciter locations

$U^k = $ a 2N x 2N diagonal matrix of diagonal elements $e^{s_r kT}$

$A_{ij} = $ a 2N dimensional vector of the residues for response i and exciter j

$N = $ number of modes

$T = $ time subinterval

$k = 1,2,3,4,...2N$

A matrix G may be defined as
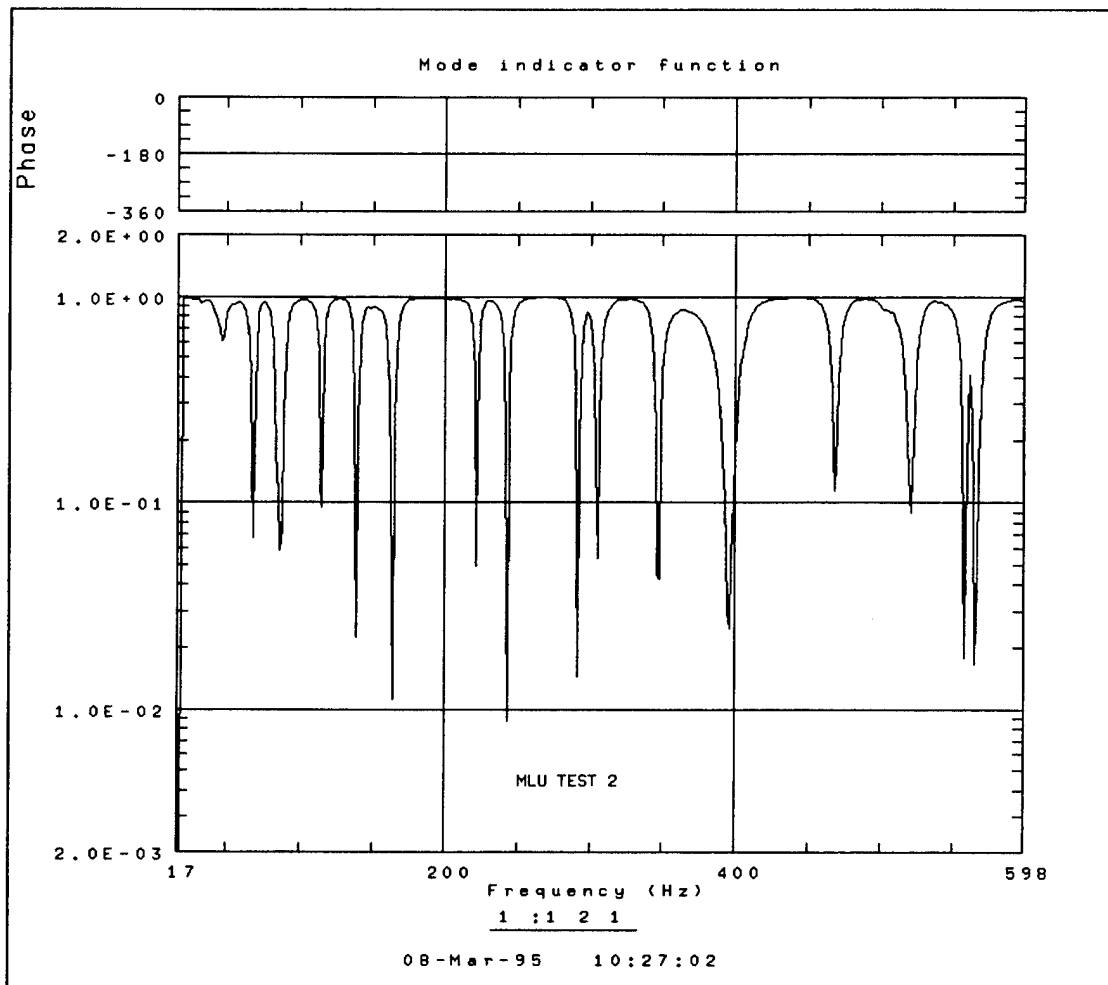
Figure B.1. Multivariate Mode Indicator Function for MLU Test Run 2

$$G = \begin{bmatrix} W \\ WU \\ WU^2 \\ . \\ . \\ WU^p \end{bmatrix} \qquad \qquad B.5$$

where p is the smallest integer such that p 1 ≥ 2N.

Then there exists a full rank matrix Q such that

$$[Q]\,[G] = 0. \qquad \qquad B.6$$

Q can be partitioned into square submatrices

$$[Q] = [\ [B(p)]\ [B(p\text{-}1)]\ .....[B(1)]\ [B(0)]\ ] \qquad \qquad B.7$$

Equation B.6 can then be rewritten as

$$\sum_{s=0}^{p} B(s)\, W\, U^{p-s} = 0 \qquad \qquad B.8$$

The coefficients B are found by multiplying each coefficient by the response given by equation B.4 for the specific time t_k resulting in

$$\sum_{s=0}^{p} B(s)\, X_i\, (t_{p-s+n}) = -X_i\, (t_{p+n}) \qquad \qquad B.9$$

This equation is solved using a least squares method to obtain the coefficients B. A byproduct of this procedure is the lower triangular correlation matrix containing the residual error terms used to determine the number of poles required for the analysis. An error chart and pole stability diagram are displayed when the Polyreference technique is implemented in IDEAS, allowing the selection of the appropriate number of poles when building the parameter table.

To determine the resonance frequencies and damping values, the method finds the zeroes of the matrix polynomial enclosed in parenthesis in the following expression

Equation B.10 was derived by multiplying equation B.8 above by e_r , the vector of

$$(\sum_{s=0}^{p} B(s) U^{p-s}_r) W_r = 0 \qquad\qquad B.10$$

zeroes except for a one in position r. Once [U] is known, the frequencies and damping values follow from

$$U_r = e^{(-\zeta_r \omega_r + j\omega dr)T} \qquad\qquad B.11$$

and $\qquad \ln |U_r| / T = -\zeta_r \omega_r$, $\qquad \angle U_r / T = \omega_{dr} = \omega_r (1 - \zeta_r)^{1/2}$. $\qquad$ B.12

The eigenvectors W_r may then be found in the null space associated with the zeroes of the matrix polynomial.

The Frequency Polyreference technique was used to generate the residues and mode shapes after the natural frequencies and damping ratios had been determined. The Frequency Polyreference method has the advantage of operating in the frequency domain, permitting the use of the residual stiffness and inertia terms from modes outside the frequency range of interest in calculating the mode shapes. The relation between the FRF's and the residues may be written in matrix form as follows:

$$
\begin{bmatrix} H_i(i\omega_L) \\ \cdot \\ \cdot \\ H_i(i\omega_n) \\ \cdot \\ \cdot \\ H_i(i\omega_H) \end{bmatrix}
=
\begin{bmatrix} W U_L \\ \cdot \\ \cdot \\ W U_N \\ \cdot \\ \cdot \\ W U_H \end{bmatrix}
\begin{Bmatrix} A^1_{ij} \\ \cdot \\ \cdot \\ A^2_{ij} \\ \cdot \\ \cdot \\ A^{2N}_{ij} \end{Bmatrix}
\qquad\qquad B.13
$$

where

$H_i(i\omega_L)$ = an 1 dimensional vector consisting of the value of the FRF at the
$\qquad$ frequency ω_L for a response at i and an exciter at j

W = the same matrix as above except that it has been scaled so that the row
$\qquad$ corresponding to the exciter has is set to one

U_n = a 2N x 2N diagonal matrix with the rth diagonal element equal to 1 / (s - s_n)

L, H = frequency range of interest.

Equation B.14 can be written as

79

$$[H] = [P] [A],\qquad\qquad\text{B.14}$$

and the least squares solution is found by the normal equations method, as follows:

$$[P]^T [H] = [[P]^T [P]] [A]\qquad\qquad\text{B.15}$$

$$[[P]^T [P]]^{-1} [[P]^T [H]] = [A].\qquad\qquad\text{B.16}$$

The residual compliance and inertance terms can be added into the [W] and [U] matrices prior to solving the equation for the residues.

With the natural frequencies, damping ratios, and residues calculated, the parameter table was complete. The residues are displayed as an amplitude value and a phase angle. The analytic function representing these parameters can be generated and compared to the measured FRF's to qualitatively check the fit; two representative samples were shown in Figures 17 and 18. If the fit is not satisfactory, the process can be repeated using a different number of poles or with the lower valued MCF modes filtered out.

The final step in the process is that of generating the mode shapes. This is accomplished by the Polyreference algorithm from the residues, damping ratios, and resonant frequencies, since

$$A^r = A^r_{re} + A^r_{im}\qquad\qquad\text{B.17}$$

and,

$$\psi^r_{re} = \frac{A^r_{re}}{\zeta_r \omega_r}\qquad\qquad\text{B.18}$$

$$\psi^r_{im} = \frac{-A^r_{re}\,\zeta_r\,\omega_r + A^r_{im}\,\omega_r\sqrt{1-\zeta_r^2}}{\zeta_r\,\omega_r^2}\qquad\qquad\text{B.19}$$

In the case of real normal modes, $A^r_{re} = 0$ so that $\psi^r_{re} = 0$ and

$$\psi^r_{im} = \frac{A^r_{im}\,\omega_r\sqrt{1-\zeta_r^2}}{\zeta_r\,\omega_r^2}\qquad\qquad\text{B.20}$$

The mode shapes are stored as a table of coefficients representing the deformation at

each node. Real or complex mode shapes can be generated using either 3 or 6 DOF's. The mode shapes from two different tests or from a finite element model solution and a test can then be compared using Modal Assurance Criteria or by graphical portrayal of the deformations. [Ref. 5, 7, 15]

APPENDIX C. MODAL ASSURANCE CRITERIA

The following presents the background behind the Modal Assurance Criteria (MAC) correlation technique.

The MAC provides a means to compare two mode shapes, whether they were derived from two separate tests, from a test and a Finite Element solution, or from the same test using different extraction techniques. MAC is a scalar value between zero and one that represents the degree of correlation between the two mode shapes. A value of one indicates good correlation where the mode shapes differ only by a scale factor; a value of zero indicates poor correlation.

The MAC is a least squares estimation technique defined by the following expression:

$$MAC = \frac{\left| \sum_{r=1}^{m} \varphi_1^*(r) \, \varphi_2(r) \right|^2}{\sum_{r=1}^{m} \varphi_1^*(r) \, \varphi_1(r) \sum_{r=1}^{m} \varphi_2^*(r) \, \varphi_2(r)} \qquad \text{C.1}$$

where $\psi_i(r)$ = mode shape for rth degree of freedom

$\psi_i^*(r)$ = mode shape complex conjugate

m = number of degrees of freedom

The MAC must be used with some caution, since there are other factors which can influence its value. For instance, the MAC may assume a value near zero for the following reasons:

1. The tested system is nonstationary due to changes in mass, stiffness, or damping properties during the test.
2. The system is non-linear.
3. The reference mode shape contains noise.
4. The method used for parameter extraction is invalid for the measured data.
5. The mode shapes are linearly independent.

83

Likewise, the MAC can take on a value near unity for the following reasons:

1. The number of responses is not sufficient to distinguish between mode shapes.

2. Unmeasured forces were responsible for the mode shapes.

3. The mode shapes are mainly coherent noise.

4. The mode shapes represent the same motion differing only by a scale factor.

Obviously, it is the last reason in each of these lists that is desired; if the others can be eliminated the MAC can be interpreted as an approximate orthogonality calculation. [Ref. 5,7]

APPENDIX D. TEST SPECIMEN MATERIAL PROPERTIES

The laminates used in the experiment were constructed from Hercules IM7 carbon fiber and 8552 epoxy matrix. IM-7 is a continuous, intermediate-modulus, polyacrylonitrile (PAN) based fiber that combines high tensile strength and modulus with good shear strength. The laminate had 16 plys, each approximately .0055 inches thick, in a symmetrical +45 / 0 / -45 / +90 layup sequence. Listed below are the specific mechanical properties of the ply and the laminate [Ref. 16].

Property	Ply	Laminate
Axial Tensile Modulus, Ex , Msi	25	9.4*
Transverse Tensile Modulus, Ey , Msi	1.39	9.4*
Axial Tensile Strength, X , ksi	400	---
Axial Compression Strength, X', ksi	240	---
Shear Strength, S, ksi	14.5	---
Density,ρ , lb/in^3	.06	.056†
Shear Modulus, Gxy , Msi	.71	3.6*
Shear Modulus, Gyz , Msi	.07*	.13*
Poisson Ratio, υxy	.31	.32*
Poisson Ratio, υyz	.34*	.32*
Fiber Volume, Vf	.62	.62

†-Measured *-Estimated from micromechanics relations.
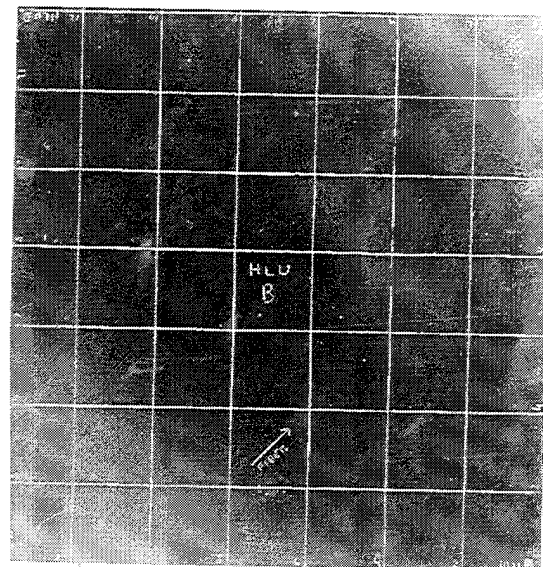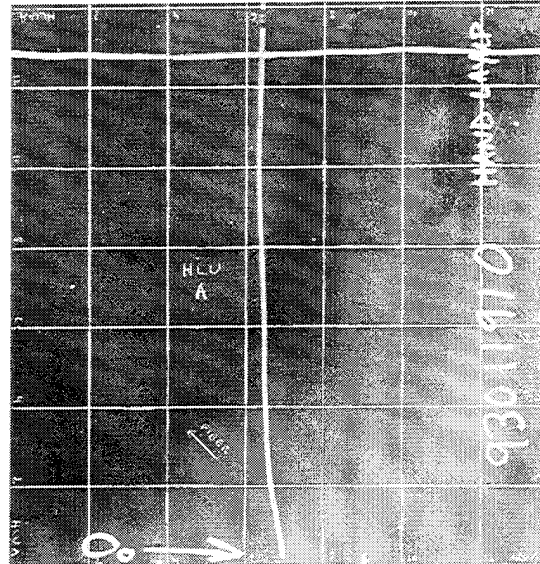
Table D.1 Material Properties of Test Specimens
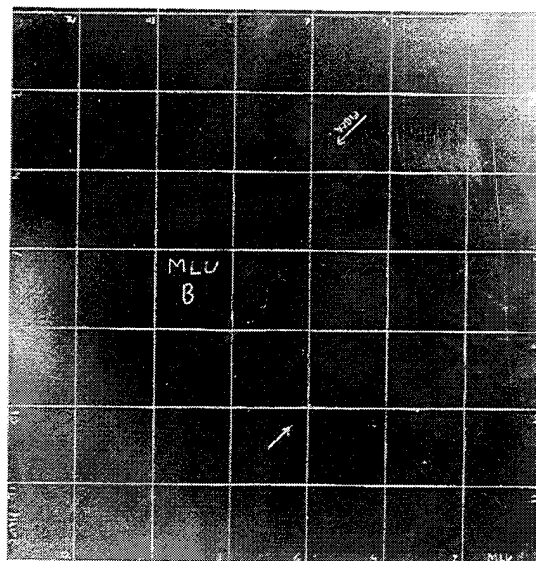
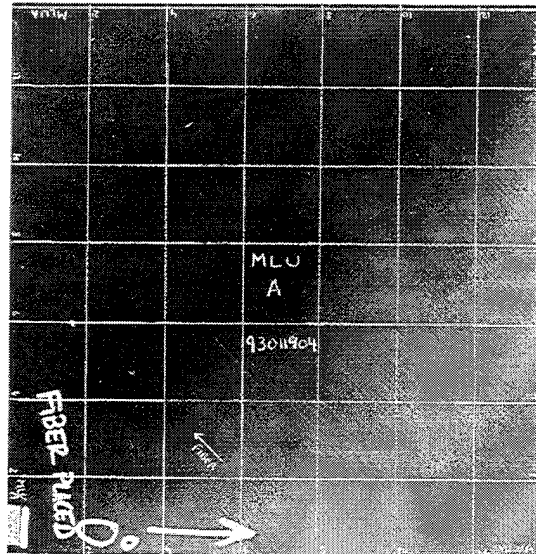Figure D.1 Hand Layup Plate (Front and Back)

Figure D.2 Machine Layup Plate (Front and Back)

APPENDIX E. MECHANICAL BEHAVIOR OF LAMINATES

The mechanical behavior of a laminate is governed by the constitutive matrix C_{ij}, which relates the applied stress to strains and curvatures. The constitutive matrix is made up of a number of submatrices, as seen in the following expressions that relate the forces and moments to the displacements [Ref. 10, p. 154].

$$\begin{Bmatrix} N_x \\ N_y \\ N_{xy} \end{Bmatrix} = \begin{bmatrix} A_{11} & A_{12} & A_{16} \\ A_{12} & A_{22} & A_{26} \\ A_{16} & A_{26} & A_{66} \end{bmatrix} \begin{Bmatrix} \epsilon^0_x \\ \epsilon^0_y \\ \gamma^0_{xy} \end{Bmatrix} + \begin{bmatrix} B_{11} & B_{12} & B_{16} \\ B_{12} & B_{22} & B_{26} \\ B_{16} & B_{26} & B_{66} \end{bmatrix} \begin{Bmatrix} \kappa_x \\ \kappa_y \\ \kappa_{xy} \end{Bmatrix} \qquad \text{E.1}$$

$$\begin{Bmatrix} M_x \\ M_y \\ M_{xy} \end{Bmatrix} = \begin{bmatrix} B_{11} & B_{12} & B_{16} \\ B_{12} & B_{22} & B_{26} \\ B_{16} & B_{26} & B_{66} \end{bmatrix} \begin{Bmatrix} \epsilon^0_x \\ \epsilon^0_y \\ \gamma^0_{xy} \end{Bmatrix} + \begin{bmatrix} D_{11} & D_{12} & D_{16} \\ D_{12} & D_{22} & D_{26} \\ D_{16} & D_{26} & D_{66} \end{bmatrix} \begin{Bmatrix} \kappa_x \\ \kappa_y \\ \kappa_{xy} \end{Bmatrix} \qquad \text{E.2}$$

where

N, M = resultant forces and moments

ϵ = strain

γ = shear strain

κ = curvature

A = extensional stiffness matrix

B = coupling stiffness matrix

D = bending stiffness matrix.

For regular symmetric angle-ply laminates, the plies are of equal thickness and are arranged such that the orientation angles of adjacent plies are opposite in sign and symmetrically layered about the middle of the laminate. The test specimens used in this investigation were a special form of this type of laminate, since the opposing angle plies of +/- 45 degrees were separated by layers oriented at 0 or 90 degrees.

For symmetric laminates the terms of the coupling matrix, B, are zero, eliminating any coupling between bending and extension. However, the presence of

the terms D_{16} and D_{26} introduces twist-curvature coupling for these types of laminates. This type of coupling has been shown to reduce the effective stiffness of the laminate with a resulting increase in deflections and a decrease in vibration frequencies. The effect of this coupling on deflections and vibration frequencies dies out as the number of ply layers is increased.

APPENDIX F. SIMULTANEOUS VECTOR ITERATION

The following describes the method of Simultaneous Vector Iteration (SVI) as applied to structural dynamics problems [Ref. 6 and 13].

SVI is two step inverse power iteration method that solves the eigenvalue problem

$$[k]\{\phi\} = \lambda[m]\{\phi\} \qquad \qquad F.1$$

where λ is the square of the natural frequencies and $\{\phi\}$ is the mode shape vector. Each iteration in the algorithm consists of two steps:

1. Inverse power:

$$[\psi] = [k]^{-1} [m] [\phi]_p \qquad \qquad F.2$$

2. Subspace orthogonalization:

$$[\phi]_{p+1} = [\psi] [Q] \qquad \qquad F.3$$

where

$$[\psi]^T [k] [\psi] [Q] = [\psi]^T [m] [\psi] [Q] [\lambda] \qquad \qquad F.4$$

and

[ϕ] = mode shape matrix

[m], [k] = mass and stiffness matrices

[Q], [λ] = eigenvectors and eigenvalues of equation F.4

p = iteration counter

As the iteration proceeds, [ϕ] and [λ] converge to the mode shapes and the square of the natural frequencies of the system.

APPENDIX G. FRF'S THROUGH RANDOM EXCITATION

For a stationary ergodic random process f (t), the autocorrelation function is defined as:

$$R_{ff}(t) = E\{f(t)\ f(t+\tau)\} = \lim_{T\to\infty} \frac{1}{T} \int_{-T/2}^{T/2} f(t)\ f(t+\tau)\ d\tau \qquad \text{G.1}$$

where T is the total time of the sample and E{ } denotes the expected value of the product of f at time t and t + τ. The autocorrelation function, unlike the random process it was derived from, meets the Dirichlet criteria for discontinuities and therefore the Fourier transform may by obtained as follows:

$$S_{ff}(\omega) = (\frac{1}{2\pi}) \int_{-\infty}^{\infty} R_{ff}(\tau)\ e^{-i\omega\tau}\ d\tau \qquad \text{G.2}$$

where S_{ff} is the auto-spectral density function. The auto-spectral density function provides frequency domain characterization of the random process.

Similarly, for a pair of functions f(t) and x(t), the cross correlation and cross spectral density are defined as:

$$R_{xf}(\tau) = E\{x(t)\ f(t+\tau)\} = \lim_{T\to\infty} \frac{1}{T} \int_{-T/2}^{T/2} x(t)\ f(t+\tau)\ d\tau \qquad \text{G.3}$$

and

$$S_{xf}(\omega) = (\frac{1}{2\pi}) \int_{-\infty}^{\infty} R_{xf}(\tau)\ e^{-i\omega\tau}\ d\tau \qquad \text{G.4}$$

Now consider an input process f(t) and a response x(t). In order to find a relation between the input and response spectral densities we introduce the impulse response function g(t) and the dummy variables λ_1 and λ_2 into the convolution

93

integrals as follows:

$$x(t) = \int_{-\infty}^{\infty} g(\lambda_1) \, f(t-\lambda_1) \, d\lambda_1 \qquad\qquad G.5$$

$$x(t+\tau) = \int_{-\infty}^{\infty} g(\lambda_2) \, f(t+\tau-\lambda_2) \, d\lambda_2 \qquad\qquad G.6$$

Using equation G.1 above and the fact that $E\{g(x)\} = g(x)$, we can write

$$R_{xx}(\tau) = E\left\{ \int_{-\infty}^{\infty} g(\lambda_1) \, f(t-\lambda_1) \, d\lambda_1 \int_{-\infty}^{\infty} g(\lambda_2) \, f(t+\tau-\lambda_2) \, d\lambda_2 \right\} \qquad G.7$$

$$= \int\int_{-\infty-\infty}^{\infty\ \infty} g(\lambda_1) \, g(\lambda_2) \, E\{f(t-\lambda_1) \, f(t+\tau-\lambda_2)\} \, d\lambda_1 d\lambda_2 \qquad G.8$$

An ergodic process is stationary; hence,

$$E\{f(t-\lambda_1) \, f(t+\tau-\lambda_2)\} = E\{f(t) \, f(t+\tau+\lambda_1-\lambda_2)\} \qquad G.9$$

$$= R_{ff}(\tau+\lambda_1-\lambda_2) \qquad\qquad G.10$$

which is the autocorrelation of the excitation process. Substituting into equation G.8 gives

$$R_{xx}(\tau) = \int\int_{-\infty-\infty}^{\infty\ \infty} g(\lambda_1) \, g(\lambda_2) \, R_{ff}(t+\tau-\lambda_2)\} \, d\lambda_1 d\lambda_2 \qquad G.11$$

Substituting this equation into the expression for the autospectra of the response yields

$$S_{xx}(\omega) = \int_{-\infty}^{\infty} R_{xx}(\tau) \, e^{-i\omega\tau} d\tau = \int_{-\infty}^{\infty} e^{-i\omega\tau} \, [\int\int_{-\infty-\infty}^{\infty\ \infty} g(\lambda_1) \, g(\lambda_2) \, R_{ff}(t+\tau-\lambda_2) \, d\lambda_1 d\lambda_2$$

$$G.12$$

94

Since

$$R_{ff}(\tau + \lambda_1 - \lambda_2) = \frac{1}{2\pi} \int_{-\infty}^{\infty} S_{ff}(\omega) e^{i\omega(\tau + \lambda_1 - \lambda_2)} d\omega \qquad \text{G.13}$$

upon substitution into equation G.12 we obtain

$$S_{xx}(\omega) = \int_{-\infty}^{\infty} e^{-i\omega\tau} \{ \int_{-\infty}^{\infty}\int_{-\infty}^{\infty} g(\lambda_1)\, g(\lambda_2)\; [\,\frac{1}{2\pi} \int_{-\infty}^{\infty} S_{ff}(\omega) e^{i\omega(\tau + \lambda_1 - \lambda_2)} d\omega\,]\; d\lambda_1 d\lambda_2 \}$$

$$\text{G.14}$$

$$= \int_{-\infty}^{\infty} e^{-i\omega\tau} \{ \frac{1}{2\pi} \int_{-\infty}^{\infty} S_{ff}(\omega)\; [\int_{-\infty}^{\infty} g(\lambda_1)\, e^{i\omega\tau}\, d\lambda_1 \int_{-\infty}^{\infty} g(\lambda_2)\, e^{-i\omega\lambda_2} d\lambda_2] e^{i\omega\tau} d\omega \}\; d\tau$$

$$\text{G.15}$$

$$= \int_{-\infty}^{\infty} e^{-i\omega\tau} \{ \frac{1}{2\pi} \int_{-\infty}^{\infty} S_{ff}(\omega)\, H(-\omega)\, H(\omega)\, e^{i\omega\tau} d\omega \}\; d\tau \qquad \text{G.16}$$

$$= \int_{-\infty}^{\infty} e^{-i\omega\tau} \{ \frac{1}{2\pi} \int_{-\infty}^{\infty} S_{ff}(\omega)\, |H(\omega)|^2\, e^{i\omega\tau} d\omega \}\; d\tau \qquad \text{G.17}$$

where H(-ω) is the complex conjugate of the frequency response H(ω). Taking the inverse Fourier transform of equation G.17 we have

$$\frac{1}{2\pi} \int_{-\infty}^{\infty} [S_{xx}]\, e^{i\omega\tau} d\omega = \frac{1}{2\pi} \int_{-\infty}^{\infty} S_{ff}(\omega)\, |H(\omega)|^2\, e^{i\omega\tau} d\omega \qquad \text{G.18}$$

Or,

$$S_{xx}(\omega) = |H(\omega)|^2\, S_{ff}(\omega) \qquad \text{G.19}$$

This expression relates the spectral densities of the input and response through the transfer function H(ω). In a similar fashion the expressions for the cross spectra are

95

$$S_{xx}(\omega) = H(\omega) \, S_{xf}(\omega) \qquad\qquad \text{G.20}$$

$$S_{fx}(\omega) = H(\omega) \, S_{ff}(\omega) \qquad\qquad \text{G.21}$$

Equations G.19, G.20 and G.21 make it possible to obtain the FRF from a random excitation in at least three different manners. This provides a convenient check on the data, since each method should give the same FRF. The ratio of the various transfer functions is known as the coherence, which ideally should be equal to 1.0 if only one excitation force is used.

In the IDEAS software and elsewhere the standard nomenclature for the transfer functions is H_1 and H_2 for the functions H in equations G.20 and G.21, respectively. IDEAS has the capability to produce the FRF through both of these methods. In addition, IDEAS can also calculate the FRF using the H_v optimal scaling method, which formulates a noise spectral matrix to account for truncation errors. [Ref. 5, 7, 14]

APPENDIX H. DATA ACQUISITION SETTINGS

Sampling Conditions

Spectral Lines	: 801	Delta f	: 1.25 Hz
Maximum Freq	: 1000.0 Hz		
Minimum Freq	: 0.0 Hz		
Frame Size	: 2048	Frame Length	: 0.8 sec
Delta t	: 3.91E-04 sec	Sampling Freq	: 2560.0 Hz
Replay Ratio	: 1.0		

Trigger Conditions

Trigger Method	: Free Run	Delay Type	: Pre Trigger
Trigger Source	: Channel	Delay Samples	: 204
Input Channel	: 1	Delay Time	: 0.07969
Level Percent	: 5.0	Delay Percent	: 10.0
Slope	: Positive		
Trigger Bell	: On		

Autorange Conditions

Autorange Before Preview	: On	Percent Frame	: 100.0
Autorange Before Acquire	: On	Percent Overhead	: 30.0

Window Conditions

Ref/Res Window : Hanning Broad

Averaging Conditions

Average Method	: Stable
Exponential Average Constant	: 5
Frames per Average	: 20
Overlap Percent	: 0.0
Frame Acceptance	: Automatic

Measurement Conditions

Acquisition Results	: FRF		
Auto Switch	: Off	Clear Lower	: 0.0
		Clear Upper	: 1000.0
Coherence Switch	: Off	Normalization	: Units^2/Hz
Ref Coherence Switch	: On	Amplitude Units	: RMS
FRF Switch	: On	FRF Method	: H1-Gyx/Gxx
Test Log Switch	: On	Log Prefix	: TEST9
Function Logging Switch	: Off		
Description	: MLU PLATE TEST 9 / 20 MAR 95		

97

Real Time Display Conditions

```
Number of Display Channels : 8
Display Units              : Engineering Units (EU)
Background Grid            : None
Range Indicators           : On
Upper Limit                : 90.0     Lower Limit : 20.0
Preview Sampling Factor     : 1.0
Acquisition Monitor        : Time and Windowed
```

Waterfall Options

```
Function Height Percent : 100.0
Number of Functions     : 30
Start Amplitude Percent : 100.0
Hidden Line switch      : On
```

Overall Shutdown Conditions

```
Overall Shutdown Switch : Off
```

Signal Sources

```
Signal Sources    : Off
Signal Type       : Burst Random
Duration (%)      : 30.0
Off Time (%)      : 70.0
Lower Freq Bound  : 0.0 Hz
Upper Freq Bound  : 1000.0 Hz
```

Source	Level
1-S1	0.09899
2-S2	0.09899

APPENDIX I. CALIBRATION PROCEDURES

A. SIGNAL ANALYZER CALIBRATION

The Zonic System 7000 signal analyser was calibrated automatically upon initialization from IDEAS Test and whenever signal processing settings were changed. The System 7000 calibrates itself through an internally generated signal that checks gain settings, filtering and phase.

B. TRANSDUCER CALIBRATION

Each transducer was individually calibrated using a mass calibration procedure whereby a block of aluminum of known mass was connected to one of the shakers through a force transducer. Each accelerometer was then placed opposite the force transducer one at a time and a random excitation was applied. The result was a flat response at a level corresponding to the inverse of the mass, since

$$F = ma \qquad\qquad\qquad I.1$$

$$a / F = 1 / m \qquad\qquad\qquad I.2$$

and the FRF we measured is simply a / F. A scale factor was applied to each transducer channel to adjust the input voltage level to meet the below criteria:

$$\frac{1}{m} = K_{cal}\,\frac{V_a}{V_f} \qquad\qquad\qquad I.3$$

For example, a sample calibration FRF before application of the scale factor is shown in Figure I.1. The flat portion of the curve is at a level corresponding to approximately 1791 in / lb_f-sec^2. The mass of the calibration block and both transducers was .0006115 lb_f-sec^2 / in. , so that

$$K_{cal} = \frac{1}{m}\,\frac{V_f}{V_a} = \frac{1}{.0006115} * \frac{1}{1791} = 0.9131 \qquad\qquad I.4$$

The scale factor so obtained was then applied to the channel in question through the channel set up feature in IDEAS Test. Figure I.2 shows the calibration FRF after
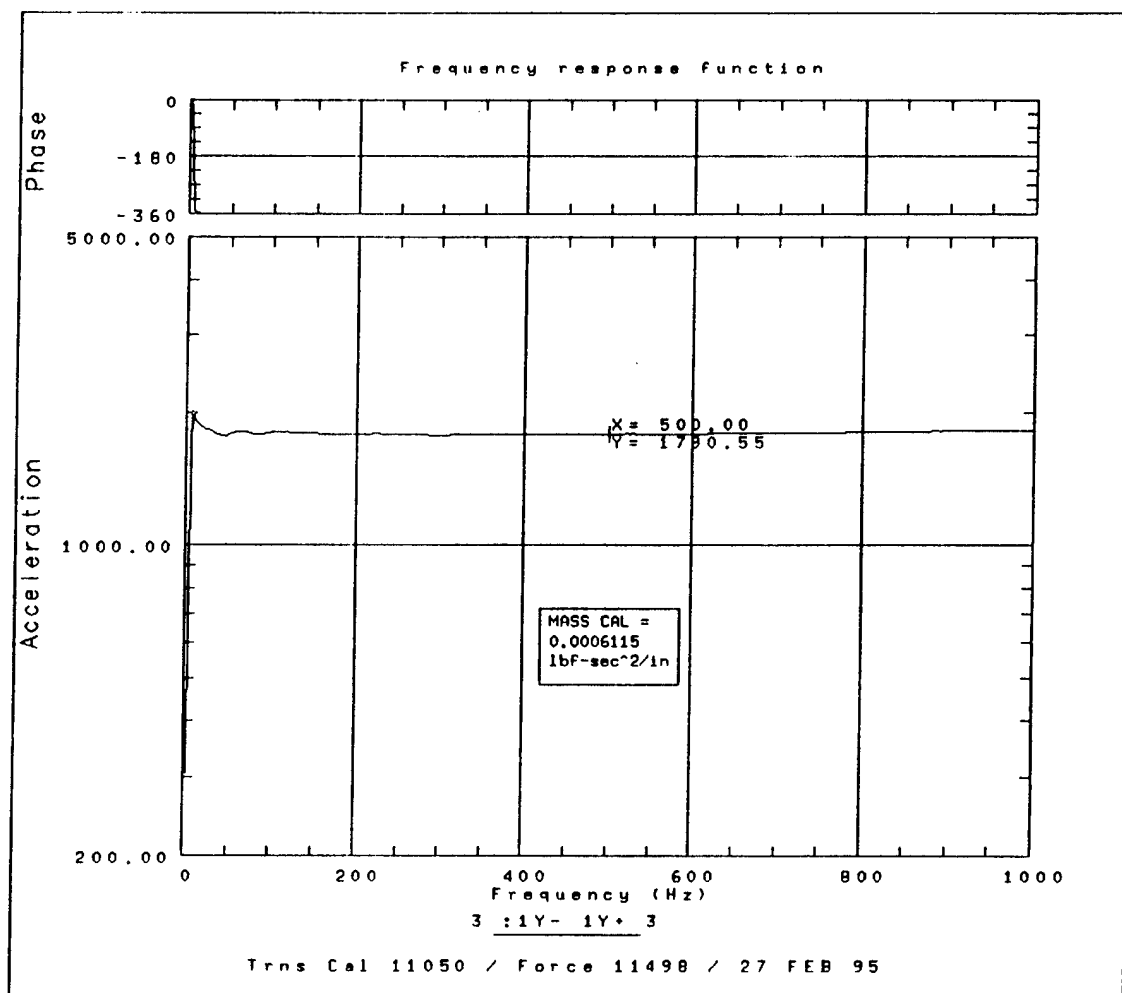
Figure I.1. Transducer Calibration FRF (Prior to Applying Scale Factor)

100
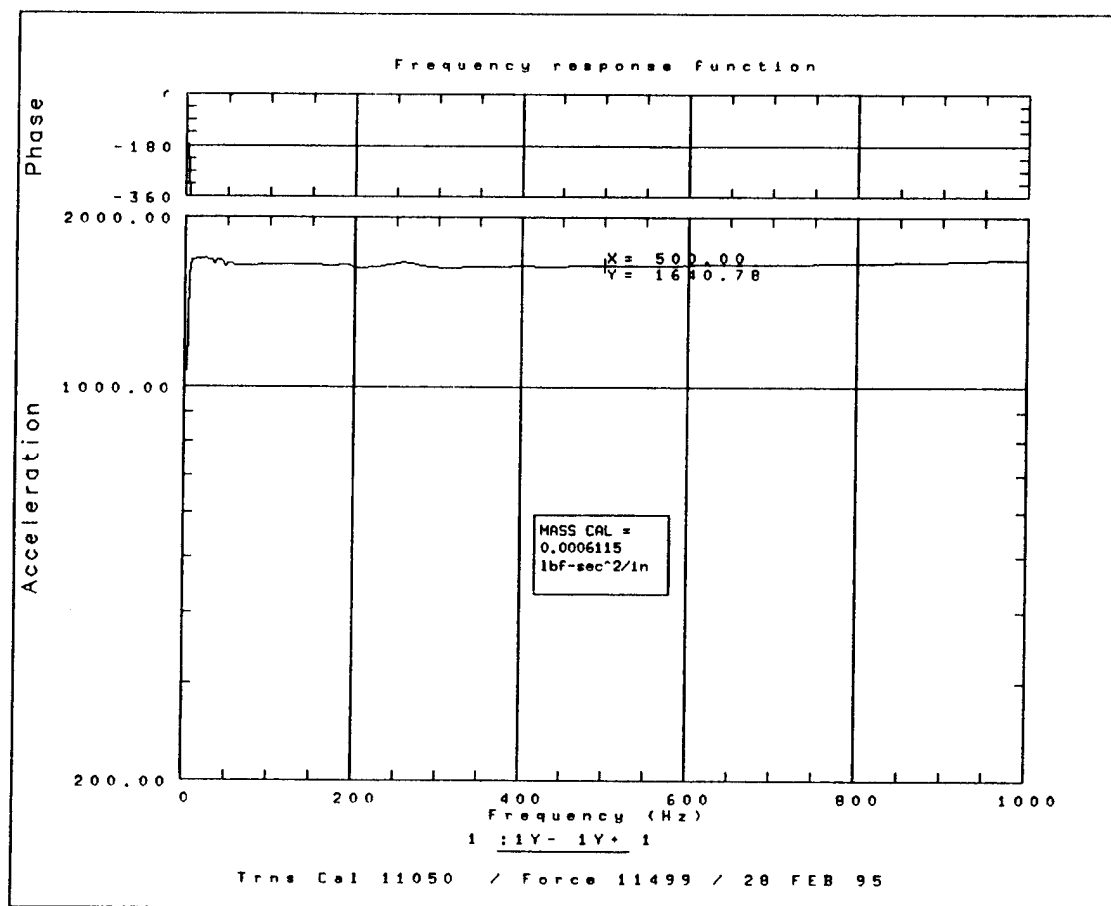
Figure I.2. Transducer Calibration FRF (After Applying Scale Factor)

application of the scale factor, where the level is within one percent of the 1/m value of 1635.3 in/lb$_f$-sec^2. This procedure was repeated for each transducer.

C. SHAKER CHECK OUT

Prior to the initial test, each shaker was checked using the procedure detailed in the Ling Electronics Model 207 Operation Manual. The procedure involves connecting an oscilloscope to the output of an accelerometer attached to the shaker's mounting surface and running a swept sine signal through the shaker. The accelerometer output is then monitored for any signal anomalies. The procedure was conducted from 0 to 2000 Hz with no discrepancies noted for either shaker.

D. TRANSDUCER SUITABILITY CHECK

To ensure the available transducers were suitable for the selected frequency range, the low frequency response was calculated from the Discharge Time Constant (DC) according to the PCB accelerometer manual. Specifically, the 3 DB down frequency is approximately

$$f_c = .16 / DC \hspace{3cm} 1.5$$

for the Model 336C34 transducers. The DC of our transducers was 50 sec, or the low frequency cut off was .0032 Hz, well below the first bending mode of our structure.

The upper frequency limitation was governed by the resonance frequency of the transducers, which was listed as 70 KHz. The PCB manual states that the transducers should only be used for applications within the lower 20 percent of the resonance frequency, or below 14 KHz. This frequency was well above our range of interest.

APPENDIX J. SAMPLE DATA OUTPUT

MODE	FREQUENCY (HERTZ)	DAMPING (%)	AMPLITUDE	PHASE (RAD)	MCF
1	64.084	0.908	8.2953E+04	1.571	0.994
2	82.878	4.054	1.6422E+05	1.571	0.982
3	110.628	0.852	3.4760E+04	-1.571	0.995
4	133.179	0.514	2.1945E+05	-1.571	0.999
5	159.599	0.215	2.5971E+05	1.571	0.998
6	221.542	0.587	1.3544E+05	1.571	0.990
7	238.048	0.189	5.2726E+05	-1.571	0.999
8	288.421	0.412	7.3539E+04	1.571	0.994
9	306.315	0.399	1.2519E+05	-1.571	0.994
10	343.383	0.227	4.7727E+05	1.571	0.997
11	390.374	0.781	7.7894E+05	1.571	0.984
12	465.919	0.579	1.7857E+05	-1.571	0.994
13	494.100	0.776	1.3248E+05	1.571	0.997
14	505.978	0.510	1.8766E+05	-1.571	0.999
15	553.979	0.299	1.6830E+06	1.571	1.000
16	562.869	0.436	5.9721E+05	1.571	0.999

Table J.1.   Modal Parameters Derived by Polyreference Technique, HLU Test

MODE	FREQUENCY (HERTZ)	DAMPING (%)	AMPLITUDE	PHASE (RAD)	MCF
1	67.955	3.081	5.8694E+04	-1.571	0.998
2	86.887	4.407	2.1013E+05	-1.571	0.987
3	114.458	1.621	1.0674E+05	1.571	1.000
4	138.654	1.591	1.1914E+05	1.571	0.997
5	163.659	1.318	3.7298E+05	1.571	0.999
6	221.525	0.746	6.1483E+05	1.571	0.999
7	242.358	0.902	5.5301E+05	1.571	1.000
8	291.394	0.810	1.6802E+05	1.571	0.999
9	304.421	0.925	1.3300E+05	1.571	0.998
10	346.639	0.975	6.5222E+05	-1.571	0.997
11	392.949	2.480	7.0102E+05	1.571	0.958
12	468.634	0.905	3.8168E+05	1.571	0.998
13	500.195	0.906	3.0744E+05	1.571	0.977
14	521.241	1.098	5.6214E+05	1.571	1.000
15	558.030	0.621	8.0497E+05	1.571	0.999
16	565.273	0.920	1.4245E+06	1.571	0.999

Table J.2.   Modal Parameters Derived by Polyreference Technique, MLU Test

Mode	HLU Freq	MLU Freq	% Change	MAC	FE Freq
1	63.914	67.955	6.323	0.981	63.12
2	83.274	86.887	4.339	0.960	88.50
3	110.916	114.458	3.193	0.942	112.27
4	133.177	138.654	4.113	0.987	148.74
5	159.609	163.659	2.538	0.978	157.16
6	221.529	221.525	-0.002	0.966	247.84
7	238.054	242.358	1.808	0.992	251.21
8	288.421	291.394	1.031	0.960	300.40
9	306.314	304.421	-0.618	0.804	321.46
10	343.377	346.639	0.950	0.954	347.88
11	390.334	392.949	0.670	0.789	403.10
12	465.959	468.634	0.574	0.664	------
13	494.085	500.195	1.237	0.056	493.75
14	505.957	521.241	3.021	0.520	526.34
15	553.995	558.030	0.728	0.840	551.64
16	562.851	565.273	0.430	0.723	563.87

Table J.3. Modal Assurance Criteria

LIST OF REFERENCES

1. Sciabica, Joe, "Overview of Non-Destructive Evaluation (NDE) Technologies for Space," *Nondestructive Evaluations for Aerospace Requirements*, Gordon and Breach Science Publishers, New York, 1989.

2. Mordfin, L. "Toward the Nondestructive Characterization of Fatigue Damage in Composite Materials," *Damage in Composite Materials*, American Society for Testing and Materials, Philadelphia, PA, 1980.

3. Gardner, Gerald C., "Introduction," *Nondestructive Testing: A Survey*, National Aeronautics and Space Administration Publication SP-5113, Washington, D. C., 1973.

4. Campbell, Marvin G., "Structural Damage Detection Using Frequency Domain Error Localization," Thesis for Master of Science in Mechanical Engineering, Naval Postgraduate School, Monterey, CA, 1994.

5. Ewins, D. J., *Modal Testing Theory and Practice*, Research Studies Press, Ltd., Letchworth, England, 1984.

6. *IDEAS Model Solution & Optimization User's Guide*, Structural Dynamics Research Corporation Publication P-10024 Rev. 1, Milford, OH, 1994.

7. *IDEAS Test User's Guide*, Structural Dynamics Research Corporation Publication P-10050B, Milford OH, 1994.

8. Rost, Robert W. "Overview of Multi-Input Frequency Domain Modal Testing Methods with an Emphasis on Sine Testing," *58th Shock and Vibration Symposium, Vol. II*, National Aeronautics and Space Administration, Huntsville, AL, 1988.

9. Brillhart, Ralph, Hunt, David L., Jensen, Brent M. and Mason, Donald R., "Modal Survey of the Space Shuttle Solid Rocket Motor Using Multiple Input Methods," *58th Shock and Vibration Symposium, Vol. I,* National Aeronautics and Space Administration, Huntsville, AL, 1988.

10. Jones, Robert M., *Mechanics of Composite Materials*, Hemisphere Publishing Corporation, USA, 1975.

11. *IDEAS Finite Element User's Guide Vol. II*, Structural Dynamics Research Corporation Publication P-10020B, Milford, OH, 1994.

12. Good, Michael and Rost, Robert, "Summary of Excitation Signals for Structural Testing," University of Cincinnati.

13. Bathe, Klaus-Jurgen, *Finite Element Procedures in Engineering Analysis*, Prentice-Hall, Inc., Englewood Cliffs, N.J., 1982.

14. Meirovitch, Leonard, *Elements of Vibration Analysis*, McGraw-Hill, New York, 1986.

15. Allemang, R. J. and Brown, D.L., "Multiple-Input Experimental Modal Analysis- A Survey," *1985 SEM Spring Conference on Experimental Mechanics*, Las Vegas, NV, 1985.

16. Product Data for IM7 Carbon Fiber, Hercules Corporation Publication Number 868-2, Magna, UT.

INITIAL DISTRIBUTION LIST

		No. Copies
1.	Defense Technical Information Center Cameron Station Alexandria, Virginia 22304-6145	2
2.	Library, Code 52 Naval Postgraduate School Monterey, California 93943-5101	2
3.	Dr. Edward M. Wu Professor of Aeronautics, Code AA/Wu Naval Postgraduate School Monterey, California 93943-5101	3
4.	Dr. Jon Raggett, Code ME/RA Professor of Mechanical Engineering Naval Postgraduate School Monterey, California 93943-5101	1
5.	Aeronautical Engineering Curricular Office, Code 31 Naval Postgraduate School Monterey, California 93943-5101	1
6.	Aeronautical Engineering Office, Code AA Naval Postgraduate School Monterey, California 93943-5101	1
7.	Timothy S. Matthews, LCDR, USN 8888 Pipestone Way San Diego, California 92129	2